UNIVERSIDADE DE COIMBRA
Faculdade de Ciências e Tecnologia
Departamento de Química

Double Many-Body Expansion Potential Energy Surfaces For Nitrogen-Hydrogen Molecular Systems

Luis Argel Poveda Calviño

COIMBRA
2007

UNIVERSIDADE DE COIMBRA
Faculdade de Ciências e Tecnologia
Departamento de Química

Double Many-Body Expansion Potential Energy Surfaces For Nitrogen-Hydrogen Molecular Systems

Dissertation presented for fulfillment of the requirements for the degree of "Doutor em Ciências, especialidade em Química Teórica"

Luis Argel Poveda Calviño

COIMBRA
2007

A mi familia

Agradecimentos

Em primeiro lugar agradeço ao meu supervisor Professor António Joaquin de Campos Varandas pela sua decisiva orientação na realização dos trabalhos aqui apresentados.

A todos os elementos do grupo de Química Teórica & Computacional pela ajuda e a simpatia dispensados durante estes anos. Em especial aos Professores Alexander Alijah e Sergio P. J. Rodrigues pelas suas valiosas sugestões e comentários, e ao Dr. Pedro J. S. B. Caridade por me auxiliar na confecção e revisão crítica da tese. Um agradecimento também especial a Vinícius C. Mota e Maikel B. Furones, pelas enriquecedoras discussões e recomendações sobre o manuscrito. Ainda agradeço aos Professores José R. Mohallem, da Universidade Federal de Minas Gerais, e Juana Z. J. Horta, da Universidade de Matanzas, Cuba, pelas suas recomendações.

Aos meus familiares e em especial a minha mãe, minhas duas irmãs e o meu pai (sempre presente), uma divida de gratidão pelo exemplo, o apoio e o amor.

Agradeço a Fundação para a Ciência e Tecnologia o financiamento através da bolsa de doutoramento que me foi concedida (SFRH/BD/8005/2002).

A minha gratidão extende-se ao departamento de Química da Universidade de Coimbra por me ter aceite como estudante de doutoramento e pelas facilidades concedidas para a realização deste trabalho.

Contents

Foreword

Molecular systems involving nitrogen and hydrogen atoms play a significant role in many chemical processes as combustion of nitrogen containing fuel [1], atmospheric cycles of pollutants [2] and nitrogen fixation [3]. In $\mathrm{De-NO}_x$ processes, environmental catalysts are used for abatement of hazardous nitrogen oxides, released when fuel is burned at high temperatures. Thus, in the selective catalytic reduction, a gaseous or liquid reductant, commonly ammonia or urea, reacts with NO_x, in the presence of a catalyst, to form water vapor and nitrogen gas. In turn, nitrogen fixation is a natural or artificial processes by which atmospheric nitrogen gas is converted into other useful nitrogen compounds (ammonia, nitrate). In the artificial ammonia synthesis [3], a nitrogen atom is hydrogenated on the surface of a catalyst, while in the biological mechanism [4] some bacterias reduce N_2 to ammonia involving a nitrogenase enzyme complex.

Eventhough, from both theoretical and experimental point of view, is very complicate to deal with such a processes, mainly due to the overwhelming physical complexity of the systems involved, a complementary description can be achieved by studying, using electronic structure calculation, of elementary gas-phase reaction analogous to those present in the real processes. Thus, the modeling of accurate global potential energy surfaces of N_xH_y systems, combined with nuclear dynamics studies, may enhance the understanding of the gas-phase nitrogen-hydrogen chemistry and support further investigations aiming at the improvement of the nitrogen fixation industrial mechanisms. For example, Haber-Bosch processes [3] can be mimic by means of radical multistep reactions: $\mathrm{N + H \rightarrow NH}$, $\mathrm{NH + H \rightarrow NH_2}$ and $\mathrm{NH_2 + H \rightarrow NH_3}$, while $\mathrm{N_2 + H_2 \rightarrow N_2H_2}$, $\mathrm{N_2H_2 + H_2 \rightarrow N_2H_4}$ and $\mathrm{N_2H_4 + H_2 \rightarrow 2NH_3}$ may be used to rigorously examine elementary steps in the biological catalytic mechanism [4].

The potential energy surface of a molecule is a function of the relative positions of the nuclei whose description is justified within the Born-Oppenheimer [5] separation. An analytical representation of the PES is achieved using different formalism, such as the double many-body expansion (DMBE) method [6]. The latter consist in to expand the potential energy function of a given molecular system in terms of the potential energies of its fragments. Information about a potential energy surface can be obtained both from the analysis of experimental data and from *ab initio* calculations. At present, robust theoretical frameworks and computational resources make possible to extensively explore the configuration space with the aim of construct accurate and global *ab initio*-based potential energy surfaces.

The main goal of the present doctoral thesis is the construction of double many-body expansion potential energy surfaces for systems involving nitrogen and hydrogen, which may used later in dynamics and kinetic studies of gas-phase reactions. Potential energy surfaces for the triatomics HN_2 and NH_2 were constructed, with the purpose of being employed as building-blocks of DMBE-PESs of larger N_xH_y systems.

Thesis is divided in two parts. The first concern with the theoretical framework supporting the case studies, presented in the second part. The following Chapter, presents the concept of potential energy surface. Chapter 2 gives a survey of the *ab initio* methods and the formalisms to obtain analytical representations. Chapter 3 deals with methods here employed to calculate spectroscopic and dynamics properties using the potential energy surfaces. Some conclusions and outlook are given in Chapter 7.

In Chapter 4, global accurate DMBE potential energy surfaces for ground state HN_2 is presented [7]. In the second paper of this chapter an improved version of the DMBE-PES for HN_2 is tested by computing spectroscopic properties and running dynamics calculations [8].

In Chapter 5, we report DMBE potential energy surfaces for doublet and quartet states of NH_2. The first paper [9] of this chapter concern with a novel switching function formalism to represent a single-sheeted DMBE potential energy surface for NH_2 ($^2A''$). An approximated single-valued representation of the lower quartet state of this triatomic is presented in second paper [10].

In Chapter 6, an *ab initio* study of the potential energy surface for N_2H_2 is given [11]. The geometries and energies of main stationary points of diimide were calculated at the multiconfiguration-reference configuration interaction (MRCI) level of theory using different basis sets. A reaction path following calculation at the complete active space self-consistent field (CASSCF) level, explore isomerization and dissociation processes of such a system. The present results provide an accurate ground for ongoing work on modeling a DMBE potential energy surface for N_2H_2.

Bibliography

[1] J. A. Miller and C. G. Bowman, Prog. Energy Combust. Sci. **15**, 287 (1989).

[2] R. P. Wayne, *Chemistry of Atmospheres* (Oxford University Press, Oxford, 2002).

[3] A. Hellman, E. J. Baerends, M. Biczysko, T. Bligaard, C. H. Christensen, D. C. Clary, S. Dahl, R. van Harrevelt, K. Honkala, O. H. Jonsson, G. J. Kroes, M. Luppi, U. Manthe, J. K. Nørskov, O. R. A. Olsen, J. Rossmeisl, E. Skulason, C. S. Tautermann, J. K. Vincent, and A. J. C. Varandas, J. Chem. Phys. B **110**, 17719 (2006).

[4] B. K. Burgess and D. J. Lowe, Chem. Rev. **96**, 2983 (1996).

[5] M. Born and J. R. Oppenheimer, Ann. Phys. **84**, 457 (1927).

[6] A. J. C. Varandas, Mol. Phys. **53**, 1303 (1984).

[7] L. A. Poveda and A. J. C. Varandas, J. Phys. Chem. A **107**, 7923 (2003).

[8] P. J. S. B. Caridade, L. A. Poveda, S. P. J. Rodrigues, and A. J. C. Varandas, J. Phys. Chem. A (in press).

[9] A. J. C. Varandas and L. A. Poveda, Theor. Chem. Acc. **116**, 404 (2006).

[10] L. A. Poveda and A. J. C. Varandas, Phys. Chem. Chem. Phys. **7**, 2867 (2005).

[11] M. Biczysko, L. A. Poveda, and A. J. C. Varandas, Chem. Phys. Lett. **424**, 46 (2006).

Part I

Theoretical framework

Chapter 1

The concept of potential energy surface

The concept of potential energy surface (PES) for a molecule comes from the possibility of describe the electronic and nuclear motions in a separate way. The validity of such a separation was established by Born and Oppenheimer [1] at the early days of quantum mechanics, who demonstrated that the simple picture of nuclei moving in a potential energy surface determined by electrons is justified due to the small mass ratio of the latter particles to the formers. In this way, the resolution of the molecular problem is attained within the so-called *adiabatic approximation*, in which an electronic Schrödinger equation is solved for a set of fixed nuclear arrangements, yielding the potential energy surface for the nuclei motion through a specific electronic state.

Although valid for the majority of chemistry, the adiabatic approximation breaks down for many important cases involving nonnegligible coupling between electronic and nuclear motions. A particularly tricking example appears when electronic states become degenerate at some points in the configuration space. In a point of degeneracy the potential energy surfaces cross each others and nonadiabatic effects appear as consequences of this "phenomenon".

1.1 Adiabatic approximation

Within the adiabatic approximation [2–4], the total molecular wave function is factorized as

$$|\Psi\left(\mathbf{r},\mathbf{R}\right)\rangle = \chi\left(\mathbf{R}\right)|\Phi\left(\mathbf{r};\mathbf{R}\right)\rangle \tag{1.1}$$

where $\mathbf{r}$ and $\mathbf{R}$ represent electronic and nuclear coordinates, relative to the center of mass of the molecule.

The term $|\Phi\left(\mathbf{r};\mathbf{R}\right)\rangle$ in (1.1) describes the electronic motion in the clamped nuclei approximation (indicated by the semicolon) and is a solution of the *eigen*-equation

$$\hat{H}\left(\mathbf{R}\right)|\Phi_j\left(\mathbf{r};\mathbf{R}\right)\rangle = V_j\left(\mathbf{R}\right)|\Phi_j\left(\mathbf{r};\mathbf{R}\right)\rangle\,, \qquad \langle\Phi_j\,|\Phi_k\,\rangle = \delta_{jk} \tag{1.2}$$

being $\hat{H}\left(\mathbf{R}\right)$ the electronic Hamiltonian, a self-adjoint operator on the Hilbert space for the electrons that depends parametrically on $\mathbf{R}$[1]. The term, $\chi\left(\mathbf{R}\right)$, describes the nuclear motion in *the potential energy surface* (PES) for a specific electronic state, determined as an eigenvalue of (1.2). The corresponding nuclear Schrödinger equation is written as

$$\left[\hat{T}_N\left(\mathbf{R}\right) + V_j\left(\mathbf{R}\right) - E_{vj}\right]\chi_{vj}\left(\mathbf{R}\right) = 0 \tag{1.3}$$

where $\hat{T}_N\left(\mathbf{R}\right)$ is the nuclear kinetic energy operator and the v index represent a quantum number for the nuclei movement[2].

The *ansatz* (1.1) is usually called the Born-Oppenheimer approximation [1], celebrating the pioneering work of these authors who demonstrated that such a factorizing of the total molecular wave function is justified due to the small mass ratio of electrons to nuclei. Indeed, Born and Oppenheimer established that up to a lower order of a perturbative expansion in the small parameter $\kappa = \left(1/M\right)^{1/4}$, where M is a representative nuclear mass in units of the electronic mass, the molecular wave function shows an adiabatic feature formally analogous to (1.1) [1].

---

[1] As usual the nuclei repulsion operator is included in the electronic Hamiltonian.

[2] In equations (1.2) and (1.3) is assumed that the center-of-mass motion of the molecule is eliminated and the so-called mass polarization term and any terms coupling electronic and nuclear coordinates are neglected.

The adiabatic approximation has a huge methodological importance by allowing a visualization of a chemical reaction as a path from reactants to products throughout a single potential energy surface. In practice a PES for a molecule can be explored by solving the equation (1.2), for an specific electronic state, for as many clamped nuclear configurations as it is thought necessary to represent the given surface.

On the other hand, it is well known that in a number of important molecular situations the simple form (1.1) does not suffice to describe all the chemical complexity of the problem. In fact, unexpected "phenomena" arise due to the coupling between the electronic and nuclear motions. Furthermore, in the Born-Oppenheimer treatment, beyond the second-order in the wave function, the simple adiabatic feature is lost, so that terms coupling the electronic and nuclear coordinates appears [1].

The usual procedure to tackle the molecular problem beyond the adiabatic description, consists in consider no only one term in (1.1), but several in the form

$$|\Psi\left(\mathbf{r},\mathbf{R}\right)\rangle=\sum_{j}^{n}\chi_j\left(\mathbf{R}\right)|\Phi_j\left(\mathbf{r};\mathbf{R}\right)\rangle \tag{1.4}$$

Eq. (1.4) represent the Born-Huang [2] approximation and its basic premise is that the preliminary solution of Eq.(1.2) allows for the drastic truncation of the summation [5]. If n were to be large, is more advisable to treat nuclei and electrons in a completely nonadiabatic way, a treatment only performed to day for small molecular systems [6, 7].

In order to derive coupled nuclear equations in the Born-Huang representation, is customary to invoke the substitution of (1.4) in the nonrelativistic full Schrödinger equation and to project from the left by one member, $\langle\Phi_k\left(\mathbf{r};\mathbf{R}\right)|$, of the *adiabatic basis*. However, this procedure is far from being trivial in the center-of-mass (COM) fixed frame, due to the presence of terms that mixes electronic with nuclear coordinates [8]. On the other hand, as traditional, the formalism could be made in the space fixed frame, but in this case (1.4) no longer will be a solution of the full Schrödinger equation, which require an additional plane-wave-type wave function to account for the COM motion [9].

Fortunately, as has been point out [9], 'In doing things that, strictly speaking, one should not do, one arrives at the correct adiabatic corrections, and so in a much simpler way than if one had first separated off the COM motion'. Then, for sake of simplicity, the following derivations will be made, as usual, in a pragmatic sense [2].

Lets assume a complete orthonormal basis of electronic eigenstates for each $\mathbf{R}$; by substituting (1.4) in the nonrelativistic full Schrödinger equation for the molecule and taking the inner product with $\langle \Phi_k (\mathbf{r}; \mathbf{R})|$, coupled equations for the $\chi_j (\mathbf{R})$ are obtained

$$\left[-\sum_{\alpha} \frac{\nabla_{\alpha}^2}{2M_{\alpha}} + V_j (\mathbf{R}) - E_{vj} \right] \chi_{vj} (\mathbf{R}) = \sum_k \Lambda_{jk} (\mathbf{R}) \chi_{vk} (\mathbf{R}) \tag{1.5}$$

where $\boldsymbol{\nabla}_{\alpha}$ is the nuclear gradient operator in coordinates of α-th nucleus, with mass M_{α} in units of the electronic mass, and the operator $\Lambda_{jk} (\mathbf{R})$ expressed as

$$\Lambda_{jk} (\mathbf{R}) = \sum_{\alpha} \frac{1}{2M_{\alpha}} \left[2\mathbf{F}_{jk} (\mathbf{R}) \cdot \boldsymbol{\nabla}_{\alpha} + G_{jk} (\mathbf{R}) \right] \tag{1.6}$$

being

$$\mathbf{F}_{jk} (\mathbf{R}) = \langle \Phi_j (\mathbf{r}; \mathbf{R}) | \boldsymbol{\nabla}_{\alpha} \Phi_k (\mathbf{r}; \mathbf{R}) \rangle \tag{1.7}$$

and

$$G_{jk} (\mathbf{R}) = \left\langle \Phi_j (\mathbf{r}; \mathbf{R}) \left| \nabla_{\alpha}^2 \Phi_k (\mathbf{r}; \mathbf{R}) \right. \right\rangle \tag{1.8}$$

the derivative vector coupling term and scalar coupling term respectively.

By comparing (1.3) with (1.5) it is verified that within the Born-Huang approach the adiabatic approximation is valid as a limit case, when the matrix elements, Λ_{jk}, are neglected. Commonly, the smallness of the derivative coupling vector, $\mathbf{F}_{jk}$, is assumed under supposition of negligible coupling between electronic states. However, such a condition may not be fulfilled, at least between consecutive electronic states, for an appreciable region of the configuration space. This becomes clear by writing the off diagonal coupling vectors in the form

$$\mathbf{F}_{jk} (\mathbf{R}) = \frac{\langle \Phi_j (\mathbf{r}; \mathbf{R}) | \boldsymbol{\nabla}_{\alpha} \hat{H} (\mathbf{R}) | \Phi_k (\mathbf{r}; \mathbf{R}) \rangle}{V_k (\mathbf{R}) - V_j (\mathbf{R})} \qquad (j \neq k) \tag{1.9}$$

obtained by taking $\boldsymbol{\nabla}_{\alpha}$ in (1.2) and combining with (1.7)[3].

---

[3] By differentiating the orthogonality condition in (1.2) and using (1.7) and (1.8) can be shown that $\mathbf{G} = \boldsymbol{\nabla} \cdot \mathbf{F} + \mathbf{F} \cdot \mathbf{F}$, thus the same conclusions apply to $\mathbf{G}$.

The expression (1.9) reveals that for low energy molecular collisions and when the system is far from degeneracy, $\mathbf{F}_{jk}$ will be small if the energy gap between the electronic states involved is large. This corresponds to an energetic difference of many atomic units, a situation only present when one of the states is very highly excited.

In fact, the smallness of the coupling terms, Λ_{jk}, is attributed to the presence of the multiplicative factor $1/M_\alpha$. Thus, an uncoupled single-surface treatment is justified, as shown by Born and Oppenheimer using a perturbative treatment, by the small mass ratio of electrons to nuclei [1].

However, in situations for which derivative couplings, Λ_{jk}, cannot be neglected, the adiabatic separation (1.1) is no longer valid. In particular near a degeneracy the vector coupling terms shows an hyperbolic behavior, as can be observed from equation (1.9). At the point of degeneracy it is said that the adiabatic potentials surfaces cross each other, a "phenomenon" that can provide a pathway for fast interstate crossing in the molecular dynamics [10].

1.2 Surface crossings

The most notable effect related to the crossing of potential energy surfaces was discovered by Herzberg and Longuet-Higgins [11] who showed that an adiabatic electronic wave function undergoes a sign change when the nuclear coordinates follow a closed path around a conical intersection[4]. Using a simple two-state model suggested by Teller [12], the sign change in the electronic wave function emerge as a property of the real electronic Hamiltonian matrix under continuation of its parameters (the nuclear coordinates). In fact, after a parameter circuit, their eigenvectors return to their original values with changed sign.

In a subsequent paper Longuet-Higgins [13] demonstrated, using topological arguments, that such sign reversal of the electronic wave function can be used to diagnose the presence of a conical intersection. The well known Longuet-Higgins's theorem states that 'if the wave function of a given electronic state changes sign when transported adiabatically around any loop in configuration space, then its

---

[4] For polyatomic molecules at least two independent variable nuclear coordinates are required to get a degeneracy of two potential surfaces. The manifold determined by the electronic energy, as a functions of such coordinates, is a cone with vertex at the intersection point.

potential energy surface must intersect that of another state at some point within the loop' [13].

The multivalueness of the electronic wave function, in the vicinity of a conical intersection, is linked to a general phenomenon discovered by M. V. Berry. In a remarkable paper [14] this author shows that any quantum state acquires a *geometric phase factor* (in addition to the familiar dynamical phase factor) when it is adiabatically transported by varying parameters in its Hamiltonian. Five years before to the Berry's discovery, the molecular version of this effect was established by Mead and Truhlar [15], when demonstrating that transporting a real electronic wave function along an infinitesimal loop in the configuration space, it acquires a phase of magnitude

$$\delta A_j = 2\mathrm{Im} \sum_{k(\neq j)} \frac{\langle \Phi_j | \, \partial \hat{H}/\partial x \, | \Phi_k \rangle \, \langle \Phi_k | \, \partial \hat{H}/\partial y \, | \Phi_j \rangle}{\left(V_j - V_k\right)^2} \delta x \delta y \tag{1.10}$$

where, for simplicity, the authors assume an infinitesimal rectangular closed path in a two-dimensional configuration space [15]. If the loop encircle a conical intersection the phase change will be equal to π, leading to the sign change of the electronic wave function obtained by Longuet-Higgins and co-workers [11, 15].

Following Mead and Truhlar [15] the *geometric phase effect* can be included by expanding the total wave function in a *gauge* [14, 16–21] transformed adiabatic basis, with components

$$\left| \tilde{\Phi}_j \left(\mathbf{r};\mathbf{R}\right) \right\rangle \equiv e^{iA_j(\mathbf{R})} \left| \Phi_j \left(\mathbf{r};\mathbf{R}\right) \right\rangle \tag{1.11}$$

That is,

$$\left| \Psi \left(\mathbf{r},\mathbf{R}\right) \right\rangle = \sum_{j}^{n} \chi_j \left(\mathbf{R}\right) \left| \tilde{\Phi}_j \left(\mathbf{r};\mathbf{R}\right) \right\rangle \tag{1.12}$$

where the $A_j\left(\mathbf{R}\right)$ are chosen to make $\left| \tilde{\Phi}_j \left(\mathbf{r};\mathbf{R}\right) \right\rangle$ single-valued and the $\left| \Phi_j \left(\mathbf{r};\mathbf{R}\right) \right\rangle$ are real-valued solutions of (1.2)[5].

By substituting (1.12) in the full Schrödinger equation and projecting from

---

[5] In turn, (1.12) can be reassociated such that $\tilde{\chi}_j\left(\mathbf{R}\right) \equiv \chi_j\left(\mathbf{R}\right) e^{iA_j(\mathbf{R})}$. In this case both, electronic and nuclear wave function will be double-valued. This procedure is less preferred, being computational cumbersome [22].

the left with $\left\langle \tilde{\Phi}_j\left(\mathbf{r};\mathbf{R}\right)\right|$, is obtained

$$\left[\sum_\alpha \frac{1}{2M_\alpha}\left(-i\boldsymbol{\nabla}_\alpha+\boldsymbol{\nabla}_\alpha A_j\right)^2+\bar{V}_j\left(\mathbf{R}\right)-E_{vj}\right]\chi_{vj}\left(\mathbf{R}\right)=\sum_{k(\neq j)}\Omega_{jk}\left(\mathbf{R}\right)\chi_{vk}\left(\mathbf{R}\right) \quad (1.13)$$

where

$$\begin{aligned}\Omega_{jk}\left(\mathbf{R}\right) &= e^{iA_{kj}(\mathbf{R})}\sum_\alpha \frac{1}{2M_\alpha}\left[-K_{jk}\left(\mathbf{R}\right)+i\left(-i\boldsymbol{\nabla}_\alpha+\boldsymbol{\nabla}_\alpha A_k\right)\cdot\mathbf{F}_{jk}\left(\mathbf{R}\right)\right.\\ &+ \left. i\mathbf{F}_{jk}\left(\mathbf{R}\right)\cdot\left(-i\boldsymbol{\nabla}_\alpha+\boldsymbol{\nabla}_\alpha A_k\right)\right], \qquad (k\neq j) \qquad (1.14)\end{aligned}$$

being $A_{kj}\left(\mathbf{R}\right)=A_k\left(\mathbf{R}\right)-A_j\left(\mathbf{R}\right)$, $K_{jk}\left(\mathbf{R}\right)$ a derivative coupling in the form

$$K_{jk}\left(\mathbf{R}\right)=\left\langle\boldsymbol{\nabla}_\alpha\Phi_j\left(\mathbf{r},\mathbf{R}\right)\left|\boldsymbol{\nabla}_\alpha\Phi_k\left(\mathbf{r},\mathbf{R}\right)\right.\right\rangle=\sum_l \mathbf{F}_{lj}\left(\mathbf{R}\right)\cdot\mathbf{F}_{lk}\left(\mathbf{R}\right) \quad (1.15)$$

and finally

$$\bar{V}_j\left(\mathbf{R}\right)=V_j\left(\mathbf{R}\right)+\sum_\alpha\frac{K_{jj}\left(\mathbf{R}\right)}{2M_\alpha} \quad (1.16)$$

The term $K_{jj}\left(\mathbf{R}\right)$ in (1.16) is called the *adiabatic correction*, a mass-dependent and $\mathbf{R}$-dependent term which cause, in general, an small shift of the adiabatic potential $V_j\left(\mathbf{R}\right)$. Near a conical intersection $K_{jj}\left(\mathbf{R}\right)$ becomes positive infinity [see Eqs. (1.15) and (1.9)], and its contribution must be considered [23–25].

In the adiabatic limit [only one term in the expansion (1.12)], the equation (1.13) becomes

$$\left[\sum_\alpha \frac{1}{2M_\alpha}\left(-i\boldsymbol{\nabla}_\alpha+\boldsymbol{\nabla}_\alpha A_j\right)^2+\bar{V}_j\left(\mathbf{R}\right)-E_{vj}\right]\chi_{vj}\left(\mathbf{R}\right)=0 \quad (1.17)$$

which look like a generalized version of (1.3). In fact, by enforcing the single-valueness of the real electronic wave function through the complex phase factor $e^{iA_j(\mathbf{R})}$, the nuclei dynamics is affected by an additional phase gradient term, $\boldsymbol{\nabla}_\alpha A_j(\mathbf{R})$, in the nuclear momentum operator.

The equation (1.17) express that even when a conical intersection is not energetically accessible, its presence is reflected on the nuclei dynamics. Besides the suspicious analogy between this effect and the well known Aharonov-Bohm effect[6], it has been noticed that the quantity $A_j\left(\mathbf{R}\right)$ behave mathematically exactly

---

[6] In the Aharonov-Bohm effect [26] the wave function of a charge particle acquires a phase change when the particle is carried around a loop enclosing a magnetic flux, even if the field itself is zero everywhere along the path.

as the vector potential of a δ-function magnetic field along the curve of intersection of two potential surfaces [15, 27, 28]. Consequently, the name "Molecular Aharonov-Bohm effect" was suggested [27].

A general procedure to treat the coupled problem (1.5), avoiding computational difficulties associated to geometric phase effects and derivative couplings, consists in looking for an unitary transformation of the electronic adiabatic basis, such that in the new eigenstates the vector coupling terms nullify [10, 29, 30]. This procedure is referred as the *diabatic* representation, a theme argued in the literature [29–35]. It can be shown that "strictly" diabatic basis do not exist [30, 35], being only possible to obtain non unique quasidiabatic representations in which a part of the derivative coupling is removable, fortunately those associated to singularities near conical intersections. Different methods to derive diabatic basis have been proposed [31, 34, 36–40].

Bibliography

[1] M. Born and J. R. Oppenheimer, Ann. Phys. **84**, 457 (1927).

[2] M. Born and K. Huang, *Dynamical Theory of Crystal Lattices* (Oxford, London, 1954).

[3] A. S. Davidov, *Quantum Mechanics* (Pergamon, Oxford, 1965).

[4] A. Messiah, *Quantum Mechanics* (Wiley, New York, 1966).

[5] D. R. Yarkony, Rev. Mod. Phys. **68**, 985 (1996).

[6] W. Kołos and L. Wolniewicz, Rev. Mod. Phys. **35**, 473 (1963).

[7] E. Deumens, A. Diz, R. Longo, and Y. Ohrn, Rev. Mod. Phys. **66**, 917 (1994).

[8] B. T. Sutcliffe, in *Potential Energy Surfaces*, edited by A. F. Sax (Springer, Berlin, 1999), pp. 61–95.

[9] W. Kutzelnigg, Mol. Phys. **90**, 909 (1997).

[10] G. A. Worth and L. S. Cederbaum, Annu. Rev. Phys. Chem. **55**, 121 (2004).

[11] G. Herzberg and H. C. Longuet-Higgins, Faraday Discuss. Chem. Soc. **35**, 77 (1963).

[12] E. Teller, J. Phys. Chem. **41**, 109 (1937).

[13] H. C. Longuet-Higgins, Proc. R. Soc., London **A.344**, 147 (1975).

[14] M. V. Berry, Proc. R. Soc. **A392**, 45 (1984).

[15] C. A. Mead and D. G. Truhlar, J. Chem. Phys. **70**, 2284 (1979).

[16] J. Moody, A. Shapere, and F. Wilczek, Phys. Rev. Lett. **56**, 893 (1986).

[17] C. A. Mead, Phys. Rev. Lett. **59**, 161 (1987).

[18] T. Pacher, C. A. Mead, L. S. Cederbaum, and H. Köppel, J. Chem. Phys. **91**, 7057 (1989).

[19] B. Zygelman, Phys. Rev. Lett. **64**, 256 (1990).

[20] C. A. Mead, Rev. Mod. Phys. **64**, 51 (1992).

[21] J. P. Ralston, Phys. Rev. D **51**, 2018 (1995).

[22] B. K. Kendrick and R. T Pack, J. Chem. Phys. **104**, 7475 (1996).

[23] D. M. Bishop and L. M. Cheung, J. Chem. Phys. **78**, 1396 (1983).

[24] D. M. Bishop and L. M. Cheung, J. Chem. Phys. **80**, 4341 (1984).

[25] J. O. Jensen and D. R. Yarkony, J. Chem. Phys. **89**, 3853 (1988).

[26] Y. Aharonov and B. Bohm, Phys. Rev. **115**, 485 (1959).

[27] C. A. Mead, Chem. Phys. **49**, 23 (1980).

[28] C. A. Mead, Chem. Phys. **49**, 33 (1980).

[29] M. Baer, Chem. Phys. Lett. **35**, 112 (1975).

[30] C. A. Mead and D. G. Truhlar, J. Chem. Phys. **77**, 6090 (1982).

[31] M. Baer and A. Alijah, Chem. Phys. Lett. **319**, 489 (2000).

[32] B. K. Kendrick, C. A. Mead, and D. G. Truhlar, Chem. Phys. Lett. **330**, 629 (2000).

[33] M. Baer, Chem. Phys. Lett. **330**, 633 (2000).

[34] M. Baer, Chem. Phys. **259**, 123 (2000).

[35] B. K. Kendrick, C. A. Mead, and D. G. Truhlar, Chem. Phys. **277**, 31 (2002).

[36] H. Werner and W. Meyer, J. Chem. Phys. **74**, 5802 (1981).

[37] T. Pacher, L. S. Cederbaum, and H. Köppel, Adv. Chem. Phys. **84**, 293 (1993).

[38] G. J. Atchity and K. Ruedenberg, Theor. Chem. Acc. **97**, 47 (1997).

[39] P. Cattaneo and M. Persico, Chem. Phys. **214**, 49 (1997).

[40] H. Nakamura and D. G. Truhlar, Chem. Phys. **115**, 10353 (2001).

Chapter 2

Calculation and modeling of potential energy surfaces

Ab initio energies to mapping a potential energy surface can be gathered by any of the *electronic structure calculation* methods aimed at solving the equation (1.2), for an specific electronic state. The problem of describing the motion of electrons in the field of fixed nuclear point charges is the central subject of quantum chemistry and significant advances have been made, over many years, to approach the exact many-electron Hamiltonian in a rigorous quantum-mechanical way [1].

A general strategy consists of solving the electronic problem in a systematic fashion, where an starting solution is obtained from an uncorrelated Hartree-Fock calculation (see section 2.1.1). At higher levels of approximation, the quality of the wave function is improved, so as to yield more and more elaborate solutions until in principle the exact solution is recovered. Such an approach combine the named *standard models* for the construction of approximated electronic wave functions [1]. The advantage of exploring different levels of theory rest in the possibility of extrapolate the results to the "exact" limit (see section 2.1.5).

A large number of *ab initio* methods are available in many package programs to perform quantum chemistry calculations. One of the most commonly used, for high level electronic structure calculation, is the program suite code MOLPRO by Werner and Knowles [2]. In the following sections a brief discussion of the standard models, adopted for the present calculations, is presented.

2.1 Overview on *ab initio* calculations

The zero-order electronic wave function is expressed, as correspond to a many-body fermion problem, as an antisymmetrized product (Slater determinant), of one-electron spin orbitals, in the form

$$|\Phi\rangle = |\phi_p, \phi_q, \ldots, \phi_n| \tag{2.1}$$

where p, q identify electronic states and $\{|\phi_p\rangle\}$ is an orthogonal basis set of one-electron molecular wave functions (molecular orbitals) whose components are expressed, as adopted in most applications, as linear combination of *atomic basis functions*, $\{|\mu\rangle\}$

$$|\phi_p\rangle = \sum_{\mu} |\mu\rangle \, c_{\mu p} \tag{2.2}$$

A *variational* solution of the electronic problem (1.2) with the trials (2.1) and (2.2), is obtained by solving the Roothaan-Hall [3, 4] Hartree-Fock equations

$$\mathbf{f}^{\mathrm{AO}}\mathbf{c} = \mathbf{S}\mathbf{c}\boldsymbol{\epsilon} \tag{2.3}$$

where $\boldsymbol{\epsilon}$ is a diagonal matrix of the orbital energies, $S_{\mu\nu} = \langle\mu|\,\nu\rangle$ and $\mathbf{f}^{\mathrm{AO}}$ is the Fock matrix with elements

$$f^{\mathrm{AO}}_{\mu\nu} = h_{\mu\nu} + 2\sum_{\rho\sigma}\sum_{i} c_{\rho i} c_{\sigma i}\left(J_{\mu\nu\rho\sigma} - \frac{1}{2}K_{\mu\sigma\rho\mu}\right) \tag{2.4}$$

containing the usual one-electron and two-electron matrix contributions.

The coefficients $c_{\mu p}$ in (2.2) play the role of variational parameters for the optimization of the Hartree-Fock energy, subjected to the orthogonality condition

$$\langle\phi_p|\,\phi_q\rangle = \delta_{pq} \tag{2.5}$$

The equations (2.3) are solved using the well known *self-consistent field* (SCF) method taking into account that the Fock matrix depends on the coefficients to be optimized. In practice, the convergent and robustness of the Roothaan-Hall SCF scheme is improved by using the direct inversion in the iterative subspace (DIIS) algorithm [5], which consist in use the information from the preceding iterations to generate the orbitals from an *average effective Fock matrix*

$$\bar{\mathbf{f}}^{\mathrm{AO}}_n = \sum_{i=1}^{n} w_i \mathbf{f}^{\mathrm{AO}}_i \tag{2.6}$$

where, to ensure that the exact one-electron part of the Hamiltonian is recovered, the sum of the weights is normalized up to the n-th iteration.

2.1.1 CI method

In the Hartree-Fock (HF) treatment the electronic repulsion is considered in an average way, discarding the correlated electronic movements due to one-particle instantaneous interactions. One general strategy to include the *correlation energy* consist in to seek the electronic wave function as linear combination of Slater determinants (configurations)[1]

$$|\Psi\rangle = C_0 |\Phi_0\rangle + \sum_{pa} C_p^a |\Phi_p^a\rangle + \sum_{\substack{p<a \\ q<b}} C_{pq}^{ab} |\Phi_{pq}^{ab}\rangle + \dots \tag{2.7}$$

where the coefficients can be estimated by a variational procedure and $\left|\Phi_p^a\right\rangle$ is obtained by promoting one electron from the occupied orbital $|p\rangle$ to the virtual orbital $|a\rangle$, $\left|\Phi_{pq}^{ab}\right\rangle$ is obtained by promoting simultaneously two electrons from the occupied orbitals $|p\rangle$ and $|q\rangle$ to the virtual orbitals $|a\rangle$ and $|b\rangle$, and so on.

The *ansatz* (2.7) is the so-called *configuration interaction* (CI) wave function [1], which recover, in principle, the exact electronic solution if a complete set of configurations is involved in the expansion. In practice, finite sets of atomic basis functions are used to represent the MOs [Eq. (2.2)] and, hence, a finite set of configurations will appear in the sum (2.7). If all possible configurations obtained by promoting all the electrons among the occupied and virtual orbitals are included in Eq. (2.7), we will have a *full configuration interaction* (FCI) model [1], a very high quality wave function which is exact within the chosen one-electron basis.

The number of determinants in an FCI wave function is given by the expression

$$N_{det} = \left(\begin{array}{c} M \\ N \end{array} \right) = \frac{M!}{N!\,(M-N)!} \tag{2.8}$$

where N is the number of electrons and M is the number of spin orbitals.

---

[1] Is often advantageous to write such an expansion in terms of the named *configuration state functions* (CSFs), which are *eigen*functions of the total and projected spins and can be obtained as linear combinations of Slater determinants (*eigen*functions of the projected spin only).

With the increase of the size of the system the FCI wave function quickly becomes intractable and one must truncate the CI expansion using only a small fraction of determinants. For most applications a CI singles and doubles (CISD) model is adopted [6] [the CISD wave function contains just the three right-hand side terms in Eq. (2.7)], given a good description of the electronic correlation energy.

2.1.2 MCSCF method

The *multiconfigurational self-consistent field* (MCSCF) wave function is a truncate CI expansion of configurations in which both the expansion coefficients and the molecular orbitals (MOs) ϕ_p are variationally optimized. This model allows for a flexible description of the electronic system, where both the one-electron functions (the MOs) and the N-electron configurations may adapt to the physical situations.

Simultaneous optimization of orbitals and coefficients is a difficult nonlinear task and a compromise appear between generate a MCSCF configuration space sufficiently flexible to describe the physical problems and yet sufficiently small to be computationally tractable. A successful approach, to select MCSCF configurations, consist in partitioning the MO space into three subspaces containing *inactive*, *active* and *virtual* (*unoccupied*) orbitals [7]. Typically, the core orbitals of a system are treated as inactive and the valence orbitals as active. In this picture, a *complete active space* (CAS) consists of all configurations obtained by distributing the valence electrons in all possible ways among the active orbitals, keeping the core orbitals doubly occupied in all configurations [7]. This model is usually called *full valence complete active space* (FVCAS). The configurations so obtained are often referred to as the *reference configurations* and the corresponding space spanned by these is called the *reference space.*

In a CASSCF wave function a part of the electronic correlation is recovered, those called *static* or *nondynamical correlation* which arise from the strong interaction between configurations nearly degenerated and is unrelated to the instantaneous repulsion between the electrons. This last energy contribution constitutes the *dynamical correlation* energy which can be subsequently recovered by adding to the wave function configurations generated by electronic excitations out of the reference space.

The MCSCF is an useful method for the treatment of the electronic structure of bonded molecular systems, for excited states calculations, and very important is its ability to describe bond breaking and molecular dissociation processes. In particular, for exploring potential energy surface, where the relative importance of the configurations changes across the surface, an optimized set of *reference configurations* obtained at the MCSCF level is a good starting wave function to do a subsequent correlated treatment.

2.1.3 MRCI method

A highly flexible CI expansion is obtained by taking as the reference not a single Slater determinant like in (2.7), but a set of *reference configurations* optimized at the MCSCF level. This constitute the *multireference configuration interaction* (MRCI) wave function [1] and its general form, including only all the single and double excitations (MRCISD), can be written as

$$|\Psi\rangle = \sum_I C^I |\Phi_I\rangle + \sum_S \sum_a C_a^S |\Phi_S^a\rangle + \sum_P \sum_{ab} C_{ab}^P \left|\Phi_P^{ab}\right\rangle \tag{2.9}$$

where a and b denote *external* orbitals (not occupied in the reference configurations) and S and P denote *internal* (containing inactive+active orbitals) $N-1$ and $N-2$ electron hole states. $|\Phi_I\rangle$, $|\Phi_S^a\rangle$ and $\left|\Phi_P^{ab}\right\rangle$ are internal, singly external and doubly external configurations, respectively.

The main bottleneck of the MRCISD method is the fact that the size of the configurations expansion and the computational effort rapidly increases with the number of reference configurations. This handicap become dramatic when studying potential energy surfaces, where an reasonable number of configurations is needed to describe all the configuration space in a balanced way.

In order to include all single and double excitations relative to the reference configurations and use much larger reference spaces, reducing the number of variational parameters, different contraction schemes have been proposed. In the "externally" contracted CI [8, 9] the singly and doubly external configurations are contracted as

$$|\Phi_S\rangle = \sum_a \alpha_a^S |\Phi_S^a\rangle \tag{2.10}$$

$$\left|\Phi_P\right\rangle = \sum_{ab} \alpha_{ab}^P \left|\Phi_P^{ab}\right\rangle \tag{2.11}$$

where the contraction coefficients α are obtained by first order perturbation theory.

In another contraction scheme the configurations are generated by applying pair excitation operators^2 to the reference wave function as a whole. This effectively generates linear combinations of the configurations $\left|\Phi_P^{ab}\right\rangle$ with different internal states P and is therefore called "internally contracted CI" [10, 11]. In the Werner and Knowles proposal [12], the internally contracted doubly external configurations are defined as

$$\left|\Phi_{pq,\omega}^{ab}\right\rangle = \frac{1}{2}\left(\hat{E}_{ap,bq} + \omega\hat{E}_{bp,aq}\right)\left|0\right\rangle \tag{2.12}$$

where $\omega = +1$ for external singlet pairs and $\omega = -1$ for triplet pairs, and $\left|0\right\rangle$ is the reference wave function, which may be composed of many configurations

$$\left|0\right\rangle = \sum_R \alpha^R \left|\Phi_R\right\rangle \tag{2.13}$$

The contracted configurations $\left|\Phi_{pq,\omega}^{ab}\right\rangle$ can be expanded in terms of the set of standard uncontracted doubly external CSFs $\left|\Phi_P^{ab}\right\rangle$ according to

$$\left|\Phi_{pq,\omega}^{ab}\right\rangle = \sum_P \left\langle\Phi_P^{ab} \middle| \Phi_{pq,\omega}^{ab}\right\rangle \left|\Phi_P^{ab}\right\rangle \tag{2.14}$$

where the contraction coefficients are given by

$$\left\langle\Phi_P^{ab} \middle| \Phi_{pq,\omega}^{ab}\right\rangle = \frac{1}{2}\sum_R \alpha^R \left\langle\Phi_P^{ab}\right| \hat{E}_{ap,bq} + \omega\hat{E}_{bp,aq} \left|\Phi_R\right\rangle \tag{2.15}$$

showing that these configurations are obtained by contracting different *internal* states.

---

[2] In second quantization such are two-electron operators in the form

$$\hat{E}_{ap,bq} = \sum_{\rho\sigma} \eta_{b\rho}^\dagger \eta_{a\sigma}^\dagger \eta_{p\sigma}\eta_{q\rho} = \hat{E}_{ap}\hat{E}_{bq} - \delta_{pb}\hat{E}_{aq}$$

where $\eta_{a\rho}^\dagger$, $\eta_{p\sigma}$ are creation and annihilation operators, ρ, σ denote electron-spin states and $\hat{E}_{ap}$ are one-electron excitation operators.

The configurations (2.12) are orthogonalized by the symmetry orthogonalization

$$\left|\Phi^{ab}_{rs,\omega}\right\rangle = \sum_{i\geq j} \left(S^{(\omega)}_{pq,rs}\right)^{-1/2} \left|\Phi^{ab}_{pq,\omega}\right\rangle \tag{2.16}$$

where $\mathbf{S}^{(\omega)}$ is a two electron density matrix with elements

$$S^{(\omega)}_{pq,rs} = \langle 0| \hat{E}_{pr,qs} + \omega \hat{E}_{ps,qr} |0\rangle \tag{2.17}$$

The Hamiltonian matrix can be diagonalized by using the popular procedure of Davidson[3] [12–14], which relies upon the formation of residual vectors that can then be used to generate an updated vector of CI expansion coefficients. The residual vectors are written as

$$\left\langle \Phi^{ab}_{D,\omega}\right| \hat{H} - E \left|\Phi\right\rangle = \left\{ \frac{1}{2} \left[\mathbf{G}^{D,\omega} + \omega \left(\mathbf{G}^{D,\omega}\right)^{\dagger} \right] - E\mathbf{C}^{D,\omega} \right\}_{ab} \tag{2.18}$$

$$\left\langle \Phi^{a}_{S}\right| \hat{H} - E \left|\Phi\right\rangle = \left(\mathbf{g}^{S} - E\mathbf{C}^{S}\right)_{a} \tag{2.19}$$

$$\left\langle \Phi_{I}\right| \hat{H} - E \left|\Phi\right\rangle = g^{I} - EC^{I} \tag{2.20}$$

where D denotes orthogonalized internally contracted $N-2$ electron states and explicit formulas for the quantities $\mathbf{G}^{D,\omega}$, $\mathbf{g}^{S}$ and g^{I} are obtained as functions of the coupling coefficients [8, 9], which are calculated using an efficient direct CI method [12, 15], in which the coupling coefficients are obtained from a relatively small number of quantities by factorizing the high order density matrices into lower order density matrices.

2.1.4 Atomic basis sets

The accuracy of the molecular electronic structure calculations is very sensitive to the size and quality of the atomic basis sets used to represent the proper molecular orbitals [Eq. (2.2)]. Hence, a careful selection of the basis functions have to be done in order to get an accurate solution in a reasonable computational time.

---

[3] An second order *quasi-Newton* method in which a new trial vector is calculated as $\Delta\mathbf{C} = -\left(\mathbf{H}_0 - E^{(0)}\mathbf{1}\right)^{-1}\left(\mathbf{H} - E^{(0)}\mathbf{1}\right)\mathbf{C}^{(0)}$, where $\mathbf{C}^{(0)}$ is a reference vector and $\mathbf{H}_0$ can be taken to be a diagonal matrix with elements equal to those of $\mathbf{H}$.

A complete basis set commonly include some expansions of nodeless *Gaussian type orbitals* (GTOs) expressed in the general form

$$\psi_{nlm}^{\mathrm{GTO}}(r,\theta,\varphi) = R_{nl}^{\mathrm{GTO}}(r)\, Y_{lm}(\theta,\varphi) \tag{2.21}$$

where $Y_{lm}(\theta,\varphi)$ are real solid harmonics and $R_{nl}(r)$ is the radial part obtained by retaining the highest power of r in *harmonic oscillator* wave functions [1].

The GTOs are used for practical reasons, even when a GTO is far from reproduce the correct shape of an atomic orbital, when compared, for example, with the *Slater type orbitals* (STO). In fact, an atomic orbital can be approximated by a linear combination of many GTOs, but the slow convergence of the expansion is more than compensated by the faster evaluation of the molecular integrals, allowing a greater number of Gaussian type functions to be used in the calculation. The GTOs are practically well suited since they are separable in the three Cartesian directions and since the product of two or more Cartesian GTOs on different centers may be written as a simple linear combination of Cartesian GTOs [1].

To construct Gaussian basis sets different contraction scheme have been proposed where the atomic orbital functions (*contracted*) of the atom are represented by fixed linear combinations of GTOs (*primitives*) [16, 17]. The coefficients of the expansion can be determined by least-square fits to accurate atomic orbitals or by minimization of the total Hartree-Fock energy. Usually a *segmented contracted* scheme is used, where each primitive function is allowed to contribute to only one contracted orbital, simplifying the evaluation of molecular integrals [18, 19].

When each occupied atomic orbital is represented using two contracted functions of the same symmetries as those of the occupied AOs, the basis is called *double-zeta* (DZ); if the number of contracted functions involved are three is called *triple-zeta* (TZ) and so on. An example particularly popular are the *split-valence* basis sets of Pople and coworkers [20, 21], in which a single-zeta representation of the core shell and a n-zeta representation of the valence shell is done. In the 6-31G basis [20], for example, the $1s$ core orbital is described by a single function expanded in six GTOs, whereas the valence $2s$ and $2p$ orbitals are each represented by two contracted functions. Each inner-valence functions is expanded in three GTOs and each outer-valence function is represented by a single primitive

GTO.

When basis functions of angular momentum higher than that of the occupied AOs are involved in the expansion, we have a *polarized basis.* The polarized functions are suited to describe the lower symmetry of molecules compared with that of their constitutes atoms and some properties due to physical perturbations. For example, in the 6-31G** basis, the first asterisk indicate the addition of a set of d functions on the first-row atoms and the second asterisk the addition of a p set on hydrogen [22]. Another type of functions can be added to the basis for a good description of the diffuse electron distributions characteristic of anionic systems, excited states and some properties as dipole moments and polarizabilities, in this case we have a *diffuse basis*, which is indicated with a "+" sign, *e. g.*, 6-31G**+.

For correlated calculations, the basis set requirements are different and more demanding since we must then describe the polarizations of the charge distribution and also provide an orbital space suitable for recovering correlation effects. For this purpose are very suited the *correlation-consistent basis sets*, where each correlating orbital is represented by a single primitive Gaussian chosen so as to maximize its contribution to the correlation energy, and where all correlating orbitals that make similar contributions to the correlation energy are added simultaneously [23, 24]. The *correlation-consistent polarized valence basis sets* is denoted by cc–pVXZ, where X is known as the *cardinal number.* X=D, T, Q or 5 indicate double-zeta, triple-zeta, quadruple-zeta or quintuple-zeta correlation-consistent basis sets respectively. By adding diffuse functions so as to improve the flexibility in the outer valence region we get the *augmented correlation-consistent basis sets* aug–cc–pVXZ [24], where one set of diffuse functions is added for each angular momentum present in the cc–pVXZ basis.

In molecular electronic structure calculations an important phenomenon is referred as the *basis-set superposition error* (BSSE) [1], which arise in calculations of interactions energies using a finite set of basis functions (as usual in practice). The BSSE appear as an spurious attractive interaction between two molecular fragments due to the fact that one fragment is describe in the presence of the basis of the other fragment. By contrast, in the calculations on the separate fragments, only the basis belonging to the separate fragments is used. An strategy to correct this error is to added a *counterpoise-corrected interaction energy* which consist in carried out all calculations, those on the fragments as well as those on the complex, in the same combined atomic basis [25]. On the other hand the BSSE can be corrected by using an approach, as discussed in the next section, to scale the *ab initio* energies to the complete basis set limit.

2.1.5 Semiempirical correction of *ab initio* energies

By truncating the atomic basis set we introduce some errors like the BSSE previously discussed, but major problems appears by using a truncate CI wave functions: the lack of *size-extensivity*. A method is said to be size extensive if the energy calculated thereby scales linearly with the number of electrons [26]. In this sense, numerical studies reveal a systematic degradation of the CISD description when the size of the system increase [1]. Indeed, as the system increase progressively, higher-order excitations become more important for a good description of the system and hence an smaller proportion of the correlation energy will be recovered by the truncate CI expansion[4].

An approach to correct the CI energy for the lack of size-extensivity is the *Davidson correction* (DC) [27], which consist in adding to the variationally determined CI energy the amount

$$E^{Q} = E_{corr}\left(1 - C_0^2\right) \tag{2.22}$$

where E_{corr} is the correlation energy obtained from CISD calculations and C_0 is the coefficient of the reference configuration.

The superscript Q in (2.22) indicate that the DC may be considered to correct for the lack of quadruple excitations effects. Using many body perturbation theory was justified the validity of (2.22) [28], although the final justification for the use of the DC is a empirical one, based on a large number of calculations. A multireference version of the DC can be obtained by replacing C_0^2 with a sum of the squares of coefficients over the reference space [26], i.e.,

$$C_0^2 \longrightarrow \sum_{i \in \mathrm{Ref}} |C_i|^2 \tag{2.23}$$

---

[4] Another effect is referred as the lack of *size-consistency* [26], associated to the inability of the method to describe properly the energy of molecular fragments in the limiting case of infinity separation.

and taken as E_{corr} the *dynamical correlation* energy obtained by the difference between MRCISD and MCSCF energies.

The lack of size-extensivity is linked to the fact that the truncate CI wave function do not include as much of the *dynamical* or *external* electron correlation effects. A method to incorporated semiempirically the *external valence*[5] correlation energy was proposed by Brown and Truhlar [29]. In such approach the *non-dynamical* (*static*) or *internal* correlation energy is obtained by an MCSCF calculation and the part of external valence correlation energy by an MRCISD calculation based on the MCSCF wave functions as references. Then, is assume that the MRCISD include a constant (*geometry independent*) fraction F of the external valence correlation energy, which can be extrapolate with the formula

$$E_{\mathrm{SEC}}\left(\mathbf{R}\right) = E_{\mathrm{MCSCF}}\left(\mathbf{R}\right) + \frac{E_{\mathrm{MRCISD}}\left(\mathbf{R}\right) - E_{\mathrm{MCSCF}}\left(\mathbf{R}\right)}{F} \tag{2.24}$$

where $E_{\mathrm{SEC}}\left(\mathbf{R}\right)$ denotes the scaled external correlation (SEC) energy, and the empirical factor F is chosen for diatomic to reproduce a bond energy and for systems with more atoms chosen to reproduce more than one bond energy in an average sense [29].

As point out by these authors [29], the SEC method requires large enough MCSCF calculation and one-electron basis sets, in order to include dominant geometry dependent internal correlation effects and an appreciable fraction of the external valence correlation energy.

By including information relative to experimental dissociation energies, the SEC method attempt to account for the incompleteness of the one-electron basis set [30]. An MRCISD calculation based on large enough basis set contribute to minimize undesirable BSSE, which may be corrected subsequently by scaling the external correlation energy.

Varandas [30] suggested a generalization of the SEC method by noticing the conceptual relationship between it and the double many-body expansion (DMBE) method [31] (the DMBE method is presented in section 2.2.2). In fact, in the DMBE scheme each n-body potential energy term is partitioned into extended-Hartree-Fock (internal correlation) and dynamic correlation (external correlation)

---

[5] The external or dynamical correlation has a *core* contribution which may be as large as the *valence* contribution, but it can often be neglected since it is nearly constant across the potential energy surface.

parts. In his proposal, denoted as DMBE-SEC [30], this author write the total interaction energy, relative to infinitely separated atoms in the appropriate electronic states, in the form

$$V\left(\mathbf{R}\right) = V_{\mathrm{MCSCF}}\left(\mathbf{R}\right) + V_{\mathrm{SEC}}\left(\mathbf{R}\right) \tag{2.25}$$

where

$$V_{\mathrm{MCSCF}}\left(\mathbf{R}\right) = \sum V^{(2)}_{\mathrm{AB,MCSCF}}\left(R_{\mathrm{AB}}\right) + \sum V^{(3)}_{\mathrm{ABC,MCSCF}}\left(R_{\mathrm{AB}}, R_{\mathrm{BC}}, R_{\mathrm{AC}}\right) + \ldots \tag{2.26}$$

$$V_{\mathrm{SEC}}\left(\mathbf{R}\right) = \sum V^{(2)}_{\mathrm{AB,SEC}}\left(R_{\mathrm{AB}}\right) + \sum V^{(3)}_{\mathrm{ABC,SEC}}\left(R_{\mathrm{AB}}, R_{\mathrm{BC}}, R_{\mathrm{AC}}\right) + \ldots \tag{2.27}$$

and the summations runs over the subcluster of atoms (dimers, trimers, ...) which compose the molecule.

The scaled external correlation energy component for the n-th terms is given by

$$V^{(n)}_{\mathrm{AB\ldots,SEC}} = \frac{V^{(n)}_{\mathrm{AB\ldots,MRCISD}} - V^{(n)}_{\mathrm{AB\ldots,MCSCF}}}{\mathcal{F}^{(n)}_{\mathrm{AB\ldots}}} \tag{2.28}$$

where $\mathcal{F}^{(n)}_{\mathrm{AB\ldots}}$ is the n-body geometry independent scaling factor.

As in the original SEC method, optimal values for two-body factors $\mathcal{F}^{(2)}_{\mathrm{AB}}$ are chosen to reproduce experimental dissociation energies, a criterion which may be adopted for higher-order terms if accurate dissociation energies exist for the relevance subsystems [30]. For the triatomic case a good guest for $\mathcal{F}^{(3)}_{\mathrm{ABC}}$ can be the average of the two-body factors

$$\mathcal{F}^{(3)}_{\mathrm{ABC}} = \frac{1}{3}\left[\mathcal{F}^{(2)}_{\mathrm{AB}} + \mathcal{F}^{(2)}_{\mathrm{BC}} + \mathcal{F}^{(2)}_{\mathrm{AC}}\right] \tag{2.29}$$

Improved agreement with experiment and best theoretical estimates, are obtained when *ab initio* energies are corrected with the DMBE–SEC method. Particularly important, for dynamics calculations, is the correct exothermicities for all arrangement channels, exhibit by the DMBE–SEC potential surfaces [30].

2.2 Analytical representation of potential energy surfaces

Once collected and scaled an extensive data set of *ab initio* energies to map the potential energy surface, the major problem is the development of a realistic global representation of such potential. A function that match the *ab initio* data within the 'chemical accuracy' provide a visualization of topographical surface features, that may not be evident from a coarse-grained *ab initio* study. Moreover, smooth and well behaved potential function can be used in dynamical studies, as theoretical counterpart of experimental reaction dynamics.

A good representations of the PES should smoothly connect the asymptotic and interaction regions of the configuration space, and have the correct symmetry properties of the molecule. It should represent the true potential energy accurately in regions of the configuration space for which experimental or theoretical data are available and it even must predict those parts of the interaction region for which no experimental or theoretical data are available. Many other criteria, that a successful representation of a PES must satisfy, can be found in the literature [32–34].

Methods to construct analytical potential energy surfaces have been developed for many years. Among the most popular approaches can be mentioned the semiempirical London-Eyring-Polanyi-Sato (LEPS) [35–37] and diatom-in-molecule (DIM) [38–40] methods, which use theoretical and experimental information to fit a functional form derived from simple molecular orbital theory. A general approach due to Murrel and co-workers [41–43] propose to represent the potential energy surface of a molecule as an expansion in energy terms of subclusters of atoms. This many-body expansion (MBE) function is an useful analytical representation even when the convergence of the series is poor [34, 43]. A practical advantage of the MBE approach is that relatively simple polynomial forms, in the internal coordinates of the molecule, need to be fitted, in the least-squared sense, to gain chemical accuracy. The potential energy surfaces discussed in the present thesis are represented using an improved version of MBE due to Varandas [31]: the double many-body expansion (DMBE) method, which consists in partitioning each n-body contribution in short-range and long-rang parts.

2.2.1 MBE method

In the MBE [41–43] method the single-valued potential energy surface of N-nucleus molecule, is represented as a cluster expansion in the form

$$V\left(\mathbf{R}^N\right)=\sum_{n=1}^{N}\sum_{i=1}^{K}V_i^{(n)}\left(\mathbf{R}^n\right) \tag{2.30}$$

where $K=N!/n!\,(N-n)!$ is the number of n-body terms in an N-atom system and $\mathbf{R}^n$ represent an n-body collective coordinates such that $\mathbf{R}^n\subset\mathbf{R}^N$.

To the expansion (2.30) is imposed the boundary condition that each n-body term vanish when one of the atoms, involved in the corresponding molecular cluster, is adiabatically removed to infinity[6]. A simple form which satisfy such requirement is written as

$$V^{(n)}\left(\mathbf{R}\right)=P\left(\mathbf{R}^n\right)T\left(\mathbf{R}^n\right) \tag{2.31}$$

where $P\left(\mathbf{R}^n\right)$ is a polynomial in the internuclear distances and $T\left(\mathbf{R}^n\right)$ is a range function which tend to zero when one of the internuclear coordinates in the n-body species tends to infinity [43].

The potential written in this form is guaranteed to satisfy all dissociation limits, an essential requirement for molecular dynamics studies. The second advantage is that the MBE suggests an strategy for building up a polyatomic potential by studying the potentials of all the fragments. Thus, a first estimate of the MBE-PES for a molecule can be made from the potentials for the relevance states of the fragments involved. Also significant is the fact that the MBE becomes most suited for implementation as a data bank of potential energy surfaces of small polyatomics [43].

2.2.2 DMBE method

Varandas [31] proposed an extension of the MBE approach by further partitioning each n-body term of (2.30), into extended Hartree-Fock ($V_{\mathrm{EHF}}^{(n)}$) and dynamic correlation ($V_{\mathrm{dc}}^{(n)}$) energy contributions. This double many-body expansion (DMBE)

---

[6] If the atoms dissociates to the ground state, the one-body term is the sum of the atom energies and can be nullified chosen a convenient energy reference. If any atom, on dissociation, left in an excited state, the "one-body" term will be a function of the $3n$-6 nuclear coordinates.

method advocate for a reliable description of the potential surface from short to large interatomic separations, by including, through a semiempirical potential, $V_{\rm dc}^{(n)}$, the dynamical correlation energy, in principle discarded in an uncorrelated electronic structure calculation [31].

At large interatomic separation, when charge overlap and electronic exchange effects can be neglected, the 'dynamic correlation energy' term can be estimated using the Rayleight-Schrödinger perturbation theory combined with the multipolar expansion of the perturbation operator [44, 45]. The resulting potential energy is partitioned in three main contributions: in first order, the electrostatic energy and, in second order, the polarization energies, which are a sum of two contributions, the induction and the dispersion energies [44, 45].

In a series of papers Varandas and coworkers [31, 46–51] propose general expressions for the n-body dynamics correlation energy term, to reproduce the proper anisotropy and asymptotic behavior of the potential energy surface for the entire configuration space (for details see cases studies). An important result refers to the introduction of an universal charge-overlap damping function to account for the damping of the dispersion coefficients for intermediate and small interatomic separations [46].

Extended Hartree-Fock approximate correlation energy for two- and three-body interactions (EHFACE2 and EHFACE3) models have been proposed [47], from simple, yet reliable, physical motivated forms. To represent the global short-range energy for two-body potential, is adopted an screened extended-Rydberg form (with an extra R^{-1} term), which reproduce, the exact $Z_A Z_B/R$ behavior at the united atom limit (EHFACE2U model [49]). In turn, the three-body EHF potential is represented by a product (2.31) with general form

$$V_{\rm EHF}^{(3)}(\mathbf{R}) = \sum_{i=1}^{m} P^{(i)}(Q_1, Q_2, Q_3) \prod_{j=1}^{3} \left\{1 - \tanh\left[\gamma_j^{(i)}\left(R_j - R_j^{i,ref}\right)\right]\right\} \tag{2.32}$$

where $P^{(i)}(Q_1, Q_2, Q_3)$ are polynomials in the symmetric coordinates $\{Q_k\}$, expressed as combinations of the internuclear coordinates $\{R_j\}$, which transform as irreducible representations of the permutation group of the molecule [43]. In turn, $R_j^{i,ref}$ represent a convenient reference geometry to which the i-th component of (2.32) is referred [52]. If extensive *ab initio* data is available, the optimized coefficients for the two-body and three-body terms can be obtained using linear or non-linear least-square fits [53].

2.2.3 Approximate single-sheeted representations

When two or more potential energy surfaces cross, an exact treatment demands a multi-sheeted representation of the PES. A such representation of the potential can be expressed as the lowest eigenvalues of a square matrix of order equal to the number of states involved [54]. Thus, the elements of the diabatic potential matrix can be written as many-body expansions or double-many body expansions involving the appropriate electronic states of the fragments.

However, for many situations an approximated single-sheeted representation can provide a good analytical form for dynamical purposes. For example, if a crossing between states is present, it can be avoided in such a way that the potential function smooths the region around the intersection point. If the crossing is located above enough respect to the dissociation channels or the stationary points of the molecule, it is expected to have a minor influence in the dynamics of the system. In the present work DMBE potential energy surfaces for the systems $HN_2\,(^2A')$ and $NH_2\,(^4A'')$ were calibrated following this procedure. Further dynamics calculations using the obtained DMBE-PES for HN_2 were carried out for the reaction $N\,(^4S) + NH\,(X^3\Sigma^-) \rightarrow N_2\left(X^1\Sigma_g^+\right) + H\,(^2S)$ showing the reliability of the approximated single-sheeted form (see paper 2 of Chapter 4).

A single-sheeted representation use switching functions to account for the presence of different states of fragments for different regions of the configuration space. A such procedure was firstly applied by Murrel and Carter [55] to construct a MBE-PES for ground-state H_2O. These authors introduce a switching one-body term for oxygen, allowing that in the potential energy surface the atomic state $O\,(^1D)$ is connected for the channel $H_2\left(X^1\Sigma_g^+\right) + O\,(^1D)$ and disconnected for the other dissociation limits. An smooth description of the PES which account for such a behavior of the oxygen atomic state, is warrant employing a switching function in the form

$$f\,(x) = \frac{1}{2}\left[1 - \tanh\left(\alpha x\right)\right] \qquad (2.33)$$

which has the limits unity as $x \rightarrow -\infty$ and zero as $x \rightarrow +\infty$.

By choosing the variable x as

$$x = n\rho_3 - \rho_1 - \rho_2 \tag{2.34}$$

where $\rho_i = R_i - R_i^0$ are the displacements of the internuclear distances from a reference structure (R_3 the H–H distance, and R_1, R_2 the OH distance), then it is easy to see that x takes the limit $-\infty$ for dissociation into $H_2 + O$ and $+\infty$ for dissociation to $OH + H$ provided $n \geq 2$.

The resulting approximated single-valued many-body expansion potential energy surface for H_2O is written as

$$V_{\mathrm{HHO}}\left(\mathbf{R}\right) = V_{\mathrm{O}(^1D)} f\left(\mathbf{R}\right) + \sum_{i=1}^{3} V_i^{(2)}\left(R_i\right) + V_{\mathrm{HHO}}^{(3)}\left(\mathbf{R}\right) \tag{2.35}$$

where the sum runs over the three diatomic pairs of the H_2O molecule and $V_{\mathrm{O}(^1D)}$ is the excited atomic potential of the oxygen referred to the ground state. The three-body energy term $V_{\mathrm{HHO}}^{(3)}\left(\mathbf{R}\right)$ is a quartic polynomial in ρ_i, calibrated to *ab initio* energies and variationally calculated vibration frequencies of H_2O [55].

Although the function (2.33) shows a proper behavior for short and intermediate distances of the triatomic, it cannot reach an unique value at the three-atom limit [55]. In fact, even for large H–H separation, the function (2.33) switches from 0 to 1 when oxygen move far away from the diatomic. To correct such unphysical behavior a most realistic switching function is proposed in the present thesis to construct an approximated single-valued DMBE-PES for $NH_2\,(^2A'')$. The improved switching form is obtained by fitting a flexible and globally valid functional form to *ab initio* data.

Bibliography

[1] T. Helgaker, P. Jøgensen, and J. Olsen, *Molecular Electronic-Structure Theory* (Wiley, London, 2000).

[2] H.-J. Werner and P. J. Knowles, MOLPRO is a package of *ab initio* programs written by H.-J. Werner, P. J. Knowles, with contributions from J. Almlöf, R. D. Amos, M. J. O. Deegan, S. T. Elbert, C. Hampel, W. Meyer, K. A. Peterson, R. Pitzer, A. J. Stone, P. R. Taylor, R. Lindh, (1998).

[3] C. C. J. Roothaan, Rev. Mod. Phys. **23**, 69 (1951).

[4] G. C. Hall, Proc. Roy. Soc. **A205**, 541 (1951).

[5] P. Pulay, J. Comput. Chem. **3**, 556 (1982).

[6] B. O. Roos and P. E. M. Siegbahn, in *Modern Theoretical Chemistry*, edited by H. Schaefer (Plenum, New York, 1977), vol. 3, chap. 7.

[7] B. O. Roos, P. R. Taylor, and P. E. M. Siegbahn, Chem. Phys. **48**, 157 (1980).

[8] P. E. M. Siegbahn, Chem. Phys. **25**, 197 (1977).

[9] P. E. M. Siegbahn, Int. J. Quantum Chem. **23**, 1869 (1983).

[10] P. E. M. Siegbahn, Int. J. Quantum Chem. **18**, 1229 (1980).

[11] H.-J. Werner and E.-A. Reinsch, J. Chem. Phys. **76**, 3144 (1982).

[12] H.-J. Werner and P. J. Knowles, J. Chem. Phys. **89**, 5803 (1988).

[13] E. R. Davidson, J. Chem. Phys. **17**, 87 (1975).

[14] E. R. Davidson, Comput. Phys. Commun. **53**, 49 (1989).

[15] B. O. Roos, Chem. Phys. Lett. **15**, 153 (1972).

[16] R. C. Raffenetti, J. Chem. Phys. **58**, 4452 (1973).

[17] J. Almlöf and P. R. Taylor, Chem. Phys. **87**, 4070 (1987).

[18] T. H. Dunning, J. Chem. Phys. **53**, 2823 (1970).

[19] T. H. Dunning, J. Chem. Phys. **55**, 716 (1971).

[20] W. J. Hehre, R. Ditchfield, and J. A. Pople, J. Chem. Phys. **56**, 2257 (1972).

[21] J. S. Binkley, J. A. Pople, and W. J. Hehre, J. Am. Chem. Soc. **102**, 939 (1980).

[22] P. C. Hariharan and J. A. Pople, Theor. Chim. Acta **28**, 213 (1973).

[23] T. H. Dunning, J. Chem. Phys. **90**, 1007 (1989).

[24] R. Kendall, T. Dunning Jr., and R. Harrison, J. Chem. Phys. **96**, 6769 (1992).

[25] S. F. Boys and F. Bernardi, Mol. Phys. **19**, 553 (1970).

[26] W. Duch and G. H. F. Diercksen, J. Phys. Chem. **101**, 3018 (1994).

[27] S. R. Langhoff and E. R. Davidson, Int. J. Quantum Chem. **8**, 61 (1974).

[28] K. Jankowski, L. Meissner, and J. Wasilewski, Int. J. Quantum Chem. **28**, 931 (1985).

[29] F. B. Brown and D. G. Truhlar, Chem. Phys. Lett. **117**, 307 (1985).

[30] A. J. C. Varandas, J. Chem. Phys. **90**, 4379 (1989).

[31] A. J. C. Varandas, Mol. Phys. **53**, 1303 (1984).

[32] J. S. Wright and S. K. Gray, J. Chem. Phys. **69**, 67 (1978).

[33] J. N. L. Connor, Comp. Phys. Comm. **17**, 117 (1979).

[34] G. C. Schatz, Rev. Mod. Phys. **61**, 669 (1989).

[35] F. London, Z. Electrochem. **35**, 552 (1929).

[36] S. Sato, J. Chem. Phys. **23**, 2465 (1955).

[37] H. Eyring and M. Polanyi, Z. Phys. Chem. Abt. **12**, 279 (1931).

[38] F. O. Ellison, J. Am. Chem. Soc. **85**, 3540 (1963).

[39] J. C. Tully, in *Potential Energy Surfaces*, edited by K. Lawley (Wiley, New York, 1980), p. 63.

[40] P. J. Kuntz, in *Atom-Molecule Collision Theory*, edited by R. Bernstein (Plenum, New York, 1979), p. 79.

[41] K. S. Sorbie and J. N. Murrell, Mol. Phys. **29**, 1387 (1975).

[42] A. J. C. Varandas and J. N. Murrell, Faraday Discuss. Chem. Soc. **62**, 92 (1977).

[43] J. N. Murrell, S. Carter, S. C. Farantos, P. Huxley, and A. J. C. Varandas, *Molecular Potential Energy Functions* (Wiley, Chichester, 1984).

[44] J. S. Dahler, J. Chem. Phys. **25**, 986 (1956).

[45] A. D. Buckingham, Adv. Chem. Phys. **12**, 107 (1967).

[46] A. J. C. Varandas and J. Brandão, Mol. Phys. **45**, 857 (1982).

[47] A. J. C. Varandas, J. Mol. Struct. Theochem **120**, 401 (1985).

[48] A. J. C. Varandas and J. Brandão, Mol. Phys. **57**, 387 (1986).

[49] A. J. C. Varandas and J. D. Silva, J. Chem. Soc., Faraday Trans. 2 **82**, 593 (1986).

[50] A. J. C. Varandas, Adv. Chem. Phys. **74**, 255 (1988).

[51] A. J. C. Varandas, Chem. Phys. Lett. **194**, 333 (1992).

[52] E. Martínez-Nuñez and A. J. C. Varandas, J. Phys. Chem. A **105**, 5923 (2001).

[53] W. H. Press, S. A. Teukolsky, W. T. Vetterling, and B. P. Flannery, *Numerical Recipes in Fortran: the Art of Scientific Computing* (Cambridge University Press, New York, 1992).

[54] J. N. Murrell and A. J. C. Varandas, Mol. Phys. **57**, 415 (1986).

[55] J. N. Murrell and S. Carter, J. Phys. Chem. **88**, 4887 (1984).

Chapter 3

Probing PESs via spectroscopic and dynamics calculations

The main goal of modeling potential energy surfaces is to study spectroscopic and dynamical properties of molecular systems. Being simple analytical forms, the DMBE-PESs here presented can be used in accurate and fast procedures to numerically evaluate the corresponding equations of motion. The spectroscopic and dynamical quantities are very sensitive to the details of the potential energy surface and, such studies, besides their predictive purposes, prove the accuracy of the PES and provides additional information for further refinements. In the present chapter, methods to calculate resonance state and rate constants, will be addressed.

Approximated techniques for the calculation of resonance states are based on the assumption that the wave function has some chosen behavior at the selected outer boundary [1]. In the complex scaling method [2–4] the resonances eigenvalues can be directly obtained upon scaling the internal degree of freedom of the Hamiltonian by an complex phase factor $exp\,(i\theta)$, which represent a 2θ rotation of the lower half complex energy plane. Such a transformation enables the resonances wavefunctions to be obtained in a square-integrable form, and use standard bound-state procedures to calculate resonance positions and widths. The complex absorbing potential (CAP) method [5–7], employed in the following thesis (see paper 2 of chapter 4), transform the Hamiltonian representing resonances to an L^2 non Hermitian effective Hamiltonian by introducing an optical potential (OP) in the asymptotic potential region. To overcome the difficulties of continually repeating the diagonalization of large matrices, various schemes combine a complex method with perturbative [8], coupled-channel [9] or finite difference [7] approaches. In the present work the CAP method is combined with the discrete variable representation (DVR) method [10], a very suited approach for study of large amplitude motion vibrations.

A rigorous treatment of the dynamics of molecular collisions require the use of quantum scattering methods, based on the resolution of the time-dependent Schrödinger equation [11]. In fact, Schrödinger equation constitute the basic concept to understand, at the atomic and molecular levels, the collision processes and correlated this with observable phenomena. However, if the process under study can be assumed as an adiabatic one, a more simple and useful treatment involves the use of a potential energy surface as an interparticle interaction potential in classical equations of motion. Indeed, when dealing with slow molecular collisions, a potential energy surface, as discussed in the present work, provide the interaction energy as a function of the configuration of the system throughout the rearrangement from reactants to products. A common approach to study the dynamics of chemical reactions is the quasiclassical trajectory (QCT) method [12–15], in which the time evolution of the system is obtained by numerical integration of the classical equations of motion and the prefix "quasi" indicate that initial conditions are chosen such that the energy in the various degrees of freedom approximately correspond to a quantum mechanical energy level.

3.1 The CAP-DVR method

The complex absorbing potential method [5] is based in the main premise that the exact asymptotic form of the exact wavefunction is not required for derivation of the resonances eigenvalues. In this way, square integrable functions are derived from the asymptotically diverging resonance states by introducing an imaginary optical potential (OP) iV which absorbs the purely outgoing wave. Thus, an L^2 complex Hamiltonian determine the n*th* resonance state through the Schrödinger equation

$$\left(\hat{H} - iV\right)\psi_n = \left(E_n - i\frac{\Gamma_n}{2}\right)\psi_n \tag{3.1}$$

where $\hat{H}$ is the usual L^2 real Hamiltonian, E_n is the resonance position and Γ_n the resonance width (inverse lifetime).

For the one-dimensional case, the equation (3.1) is analyzed in the finite interval $[0, R_{\max}]$, where the boundary region $[R_B, R_{\max}]$ define the range of the absorbing potential. As demanded, for a "free potential" intermediate interval $[R_A, R_B]$ the resonance states satisfies the appropriate Siegert [16] boundary conditions, providing that in such interval the system is not strongly perturbed by the addition of the optical potential[1].

The solutions of the equation (3.1) can be found by representing the complex Hamiltonian in a finite basis set of the real vibrational Hamiltonian $\hat{H}$. In order to minimize errors associated to basis set truncation and artificial perturbations induced by the absorbing potential, a variational parameter (λ) is included in the potential, which is then optimized respect to the complex eigenvalue of (3.1) [5, 6, 17]. The latter is carried out by diagonalizing the complex Hamiltonian for a set of λ values. Thus, the complex eigenvalue for the optimal λ is the best estimate to the exact resonance, $E_n - i\,(\Gamma/2)$.

A simple and fast numerical procedure to solve (3.1) is attained by using a discrete variable representation (DVR) method as suggested by Light and coworkers [10, 18–21], for the calculation of ro-vibrational states. Besides a basis sets $\{\phi_i; i = 1, \ldots, N\}$ to expand the Hamiltonian, the implementation of the DVR require a Gauss quadrature rule with a set of quadrature points $\{x_\alpha; \alpha = 1, \ldots, N\}$ and weights $\{\omega_\alpha; \alpha = 1, \ldots, N\}$. The standard DVRs are defined in terms of classical polynomials such as particle-in-a-box functions (Chebyshev polynomials), harmonic oscillator functions (Hermite polynomials), Legendre polynomials, Laguerre polynomials, etc., their related weight functions and Gaussian quadratures.

The Hamiltonian evaluation in the DVR relied in the fact that an "exact" representation of the Hamiltonian matrix in a variational basis set (*variational basis representation*), can be approximated by an *finite basis representation* (FBR), in which some matrix elements of the Hamiltonian are determined by numerical quadrature over the DVR points [22]. In turn, for basis of N classical orthog-

---

[1] Indeed, partial waves are reflected on the wall of the optical potential, resulting in non purely exponentially decaying behavior of the resonance states.

onal polynomials exist an isomorphism between DVR and FRB defined by the orthogonal transformation [23]

$$\mathbf{U}_{i\alpha} = \boldsymbol{\phi}_i\left(x_\alpha\right)\boldsymbol{\omega}_\alpha^{1/2} \tag{3.2}$$

Thus, in the orthonormal DVR basis, obtained by direct diagonalization of the position operator [24] or from the polynomial themselves via

$$\varphi_\alpha\left(x\right) = \sum_{i=1}^{N} U_{i\alpha}^{\dagger}\phi_i\left(x\right) \tag{3.3}$$

the potential matrix is approximated by the simple diagonal form

$$\left(\mathbf{U}^{\dagger}\mathbf{V}^{\mathrm{FBR}}\mathbf{U}\right)_{\alpha\beta} = \left(\mathbf{V}^{\mathrm{DVR}}\right)_{\alpha\beta} = V\left(x_\alpha\right)\delta_{\alpha\beta} \tag{3.4}$$

In practice the appropriate Gaussian quadrature scheme is generated from (3.2), and for the multidimensional case the required composite transformation is written as a product of 1D transformations [21]. Hence, a sequential truncation/diagonalization procedure can be used, in which the structure sparseness of the DVR Hamiltonian is exploited to generate in a sequential fashion good contracted basis sets in an increasing number of dimension [24].

3.2 The QCT method

In the quasiclassical trajectories (QCT) method the time evolution of the classical degrees of freedom of individual atoms are simulated by solving Hamilton's or Newton's equations of motion expressed in term of the coordinates $\mathbf{q}$ and momentum $\mathbf{p}$ of the system. In the Hamilton formulation [25] propagation is done by numerical integration of the first-order differential equations

$$\frac{dq_i}{dt} = \frac{\partial H\left(\mathbf{q},\mathbf{p}\right)}{\partial p_i}, \qquad \frac{dp_i}{dt} = -\frac{\partial H\left(\mathbf{q},\mathbf{p}\right)}{\partial q_i} \tag{3.5}$$

where the Hamiltonian

$$H\left(\mathbf{q},\mathbf{p}\right) = T\left(\mathbf{q},\mathbf{p}\right) + V\left(\mathbf{q}\right) \tag{3.6}$$

is the sum of the kinetic $T\left(\mathbf{q},\mathbf{p}\right)$ and potential energies $V\left(\mathbf{q}\right)$.

For integrating Eq. (3.5) can be used symplectic or nonsymplectic schemes depending on whether or not the numerical method preserves geometric properties of the exact flow of the differential equations [26]. The symplectic algorithms has the desirable property of preserving Poincaré integral invariants and phase space volume, features of the exact Hamiltonian dynamics [25], by using a canonical mapping of the coordinates and momentum at each time step [26, 27]. However, the use of one integrator or another depends on the physical system and the properties being studies [28]. Thus, nonsymplectic schemes, as the high-order Runge-Kutta method [29], are more accurate for short time trajectories of small systems [30], whereas for long time integration of large systems, the symplectic integrators shows a greater stability [28].

The remaining problem of a quasiclassical trajectory simulation is choosing the initial conditions so that the results from an ensemble of trajectories may be compared with experiment and/or theory, and used to make predictions about the chemical system's molecular dynamics.

3.2.1 Unimolecular decomposition

In the unimolecular dissociation, a molecule is prepared in a vibrational-rotational excited state A^* above the unimolecular threshold from which the molecule has a probability to dissociated to products. Assuming that the system is initially excited with a microcanonical ensemble and its intramolecular dynamics is ergodic[2], the probability of decomposition per unit time will be

$$P\left(t\right) = k\left(E\right)\exp\left[-k\left(E\right)t\right] \tag{3.7}$$

given equal probability during any time interval for reaction to occur [31–33].

However, for a large number of experiments the Eq. (3.7) does not hold, due to the not random character of the transition between states. Indeed, for a not sufficiently fast intramolecular vibrational-energy redistribution (IVR), the transition between some states will be more probable than others.

An important question is whether an unimolecular decomposition is random in the sense (3.7), or does not obey such equation [34–36]. In this way, differ-

---

[2] Such is called Rice-Ramsperger-Kassel-Marcus (RRKM) behavior [31–33], for which all the accessible states of the molecule are occupied in random order.

ent schemes have been developed, as the Monte Carlo sampling, for exciting A^* randomly with a microcanonical ensemble of states, and nonrandomly excitation procedures, involving specific state selection [15, 37].

3.2.2 Bimolecular reactions

For bimolecular reactions the quantities of interest in such studies commonly included the reaction cross-section and the thermal bimolecular rate constant. For the simple case of an atom B plus a symmetric top polyatomic molecule A, the reactive cross-section may be expressed as $\sigma_r\left(v_{rel}, \nu_A, J_A, K_A\right)$, where v_{rel} is the $A+B$ relative velocity and ν_A, J_A and K_A are the polyatomic's vibrational and rotational quantum numbers.

Assuming Boltzmann distributions of vibrational-rotational levels specified by temperature T_A, the reactive Boltzmann-average cross-section can be obtained as

$$\sigma_r\left(v_{rel}; T_A\right) = \sum_{\nu_A} \sum_{J_A, K_A} \sigma_r\left(v_{rel}, \nu_A, J_A, K_A\right) P\left(\nu_A; T_A\right) P\left(J_A, K_A; T_A\right) \tag{3.8}$$

where $P\left(\nu_A; T_A\right)$ and $P\left(J_A, K_A; T_A\right)$ are the normalized Boltzmann distribution for ν_A and J_A, K_A at temperature T_A.

The bimolecular rate constant for a fixed relative velocity is obtained by multiplying Eq. (3.8) by v_{rel}. By integrating such a product over the Boltzmann relative velocity distribution $P\left(v_{rel}; T\right)$ for temperature $T = T_A$ gives the thermal bimolecular rate constant:

$$k\left(T\right) = \int_0^\infty v_{rel} \sigma_r\left(v_{rel}; T\right) P\left(v_{rel}; T\right) dv_{rel} \tag{3.9}$$

Inserting the Maxwell-Boltzmann distribution for $P\left(v_{rel}; T\right)$ into (3.9) and introducing the translational energy by the relation $E_{tr} = \mu_{AB} v_{rel}^2/2$, the thermal rate constant may be written as

$$k\left(T\right) = \left(\frac{8kT}{\pi\mu}\right)^{1/2} \left\langle \sigma_r\left(E_{tr}\right)\right\rangle \tag{3.10}$$

where the average cross section for temperature T will be

$$\left\langle \sigma_r\left(E_{tr}\right)\right\rangle = \int_0^\infty \sigma_r\left(E_{tr}\right) \frac{E_{tr}}{\left(kT\right)^2} e^{-E_{tr}/kT} dE_{tr} \tag{3.11}$$

Then, the integral (3.11) can be evaluated by sampling randomly the translational energy E_{tr} by the von Neumann rejection method [38] or by the cumulative distribution function (CDF) [12]

$$E_{tr} = -kT \ln \left(\xi_{tr}^{(1)} \xi_{tr}^{(2)} \right) \tag{3.12}$$

where $\xi_{tr}^{(1)}$ and $\xi_{tr}^{(2)}$ are independent random numbers.

In turn, a simple expression for the reaction cross section can be derived from the classical mechanical expression for this quantity [39]

$$\sigma_r = \int_0^{b_{max}} P_r \left(b \right) 2\pi b db \tag{3.13}$$

where b is the collision impact parameter, b_{max} is its largest value that leads to reaction and $P_r \left(b \right)$ is the so-called opacity function given the impact parameter distribution.

From (3.13) it is derived [37] that

$$\sigma_r = \langle P_r \left(b \right) \rangle \pi b_{max}^2 \tag{3.14}$$

Random values of b between 0 and b_{max} may be sampled with the CDF

$$\xi = \int_0^{b} P \left(b \right) db \tag{3.15}$$

where ξ is a random number. Then, the average reaction probability is $\langle P_r \left(b \right) \rangle = N_r / N$, where N is the total number of trajectories and N_r the number which are reactives. By substituting in (3.14), the reaction cross-section is [15]

$$\sigma_r = \frac{N_r}{N} \pi b_{max}^2 \tag{3.16}$$

In the same way, as the translational energies are randomly sampled, the bimolecular rate constant (3.10) may be expressed as [15]

$$k \left(T \right) = g_e \left(T \right) \left(\frac{8kT}{\pi \mu} \right)^{1/2} \frac{N_r}{N} \pi b_{max}^2 \tag{3.17}$$

where $g_e \left(T \right)$ is the temperature-dependent electronic degeneracy factor [40–43], introduced to account for the probability of a collision occurring on a particular surface.

A similar procedure as describe above, to choose b and E_{tr}, is used to sampled reactant's Cartesian coordinates and momenta for study polyatomic+polyatomic collisions. Within the quasi-classical spirit, initial coordinates and momenta should correspond, as much as possible, to a quantum mechanical description of the colliding entities.

For the simple case of atom+diatom ($B + A$) reaction, the Cartesian coordinates and momenta for the diatomic are chosen as corresponding to vibrational (ν_A) and rotational (J_A) quantum numbers and then randomly rotating these coordinates about the center of mass of the diatom.

First, the diatomic distance, r, and the momentum along the line-of-center of A, p_r, are randomly sampled for fixed values of the vibration-rotation energy given by

$$E_{vr} = \frac{p_r^2}{2\mu} + \frac{J_A\left(J_A+1\right)\hbar^2}{2\mu r^2} + V\left(r\right) \tag{3.18}$$

where $V\left(r\right)$ is the diatomic potential.

The values of E_{vr} are determined from ν_A and J_A by satisfying the semiclassical quantization condition [44–46]

$$\left(\nu_A + \frac{1}{2}\right) h = \oint \left\{2\mu\left[E_{vr} - \frac{J_A\left(J_A+1\right)\hbar^2}{2\mu r^2} - V\left(r\right)\right]\right\} dr \tag{3.19}$$

Then, the von Neumann rejection method [38] can be used to randomly choose an r,p_r pair, in the interval between the outer and inner turning points.

The preceding values for r, p_r, and the rotational angular momentum, given by $j = \sqrt{J_A\left(J_A+1\right)}\hbar$, are then transformed to Cartesian coordinates and momenta. The polyatomic molecule is now randomly oriented in space by multiplying the obtained Cartesian pairs ($\mathbf{q}^0$,$\mathbf{p}^0$) by the Euler rotation matrix [25]

$$\mathbf{q} = \mathbf{R}\left(\theta,\phi,\chi\right)\mathbf{q}^0 \qquad \mathbf{p} = \mathbf{R}\left(\theta,\phi,\chi\right)\mathbf{p}^0 \tag{3.20}$$

with the Euler's angles chosen randomly, using three different random numbers $(\xi_\theta, \xi_\phi, \xi_\chi)$, according to

$$cos\theta = 2\xi_\theta - 1 \qquad \phi = 2\pi\xi_\phi \qquad \chi = 2\pi\xi_\chi \tag{3.21}$$

Since A has a random orientation in a space-fixed coordinate frame, the B atom may be placed in the y,z plane without loss of generality [15]. The x,y,z

coordinates of B are then

$$x = 0 \qquad y = b \qquad z = \left(s^2 - b^2\right)^{1/2} \tag{3.22}$$

where s is the initial separation between B and the A center of mass, and b is the impact parameter.

For the atom+diatom collisions, the Boltzmann-average cross-section (3.8) can be determined by sampling the corresponding Boltzmann distributions by the rejection method [38] or by the CDFs

$$\sum_{\nu_A=0}^{\nu_A} \frac{e^{-(\nu_A+1/2)\hbar\omega_A/kT}}{Q_{vib}} = \xi_{vib} \tag{3.23}$$

and

$$\sum_{J_A=0}^{J_A} \frac{(2J_A+1)\, e^{-J_A(J_A+1)\hbar^2/2I_AkT}}{Q_{rot}} = \xi_{rot} \tag{3.24}$$

The polyatomic+polyatomic case follow the same procedure as those above described, except for polyatomics there are more vibrational and rotational quantum numbers to consider.

3.2.3 Products properties from QCT runs

The end point of a trajectory occurs when it enters a regions of phase space designated as reactants or products space. Once the product molecules have been determined by testing interatomic distances, using geometric and energetic criteria can be determined whether the molecules are in bound, quasi-bound or dissociative states.

Among the products properties in a QCT run are the relative translational energy of the formed molecules, the scattering angle between the initial and final relative velocity vectors and their vibrational and rotational energies. For diatomics, almost all of these quantities are straightforward from the coordinates and velocities of the product molecules [15]. For example, vibrational and rotational quantum numbers are determined for a diatomic from the Eintein-Brillouin-Keller (EBK) semiclassical quantization condition [44–46]. For polyatomics, no general algorithm have been established for finding their vibrational and rotational quantum numbers [15], mainly due to vibrational-rotational couplings, the multidimensionality of the problem, and possible resonances between the vibrational modes [15].

Bibliography

[1] J. L. Jackon and R. E. Wyatt, Chem. Phys. Lett. **4**, 643 (1970).

[2] J. Aguilar and J. M. Combes, Commun. Math. Phys. **22**, 269 (1971).

[3] E. Baslev and J. M. Combes, Commun. Math. Phys. **22**, 280 (1971).

[4] B. Simon, Commun. Math. Phys. **27**, 1 (1972).

[5] G. Jolicard and E. J. Austin, Chem. Phys. Lett. **121**, 106 (1985).

[6] G. Jolicard, C. Leforestier, and E. J. Austin, J. Chem. Phys. **88**, 1026 (1987).

[7] G. Jolicard and G. D. Billing, J. Chem. Phys. **97**, 997 (1992).

[8] N. Moiseyev and P. R. Certain, Mol. Phys. **37**, 1621 (1979).

[9] O. Atabek and R. Lefebvre, Phys. Rev. **22**, 1817 (1980).

[10] J. V. Lill, G. A. Parker, and J. C. Light, Chem. Phys. Lett. **89**, 483 (1982).

[11] J. Z. H. Zhang, *Theory and Application of Molecular Dynamics* (Worl Scince, Singapore, 1999).

[12] D. L. Bunker, Meth. Comp. Physics **10**, 287 (1971).

[13] D. G. Truhlar and D. A. Dixon, in *Atom-Molecule Collision Theory: A Guide for the Experimentalist*, edited by R. Bernstein (Plenum Press, New York, 1979), p. 595.

[14] L. M. Raff and D. L. Thompson, in *Theory of Chemical Reaction Dynamics*, edited by M. Baer (Chemical Rubber, Boca Raton, 1985), p. 1.

[15] W. L. Hase, *Encyclopedia of Computational Chemistry* (Wiley, New York, 1998).

[16] A. F. J. Siegert, Phys. Rev. **56**, 750 (1939).

[17] G. Jolicard and E. J. Austin, Chem. Phys. **103**, 295 (1986).

[18] R. W. Heather and J. C. Light, J. Chem. Phys. **79**, 147 (1983).

[19] Z. Bačić and J. C. Light, J. Chem. Phys. **85**, 4594 (1986).

[20] Z. Bačić and J. C. Light, J. Chem. Phys. **86**, 3065 (1987).

[21] Z. Bačić and J. C. Light, Annu. Rev. Phys. Chem. **40**, 469 (1989).

[22] D. O. Harris, G. G. Engerlhom, and W. D. Gwinn, J. Chem. Phys. **43**, 1515 (1965).

[23] A. S. Dickinson, J. Chem. Phys. **49**, 4209 (1968).

[24] J. C. Light and T. Carrington Jr., Adv. Chem. Phys. **114**, 263 (2000).

[25] H. Goldstein, *Classical Mechanics* (Addison-Wesley, Reading, 1980).

[26] V. L. Arnold, *Mathematical Methods of Classical Mechanics* (Springer-Verlag, New York, 1978).

[27] J. D. Meiss, Rev. Mod. Phys. **64**, 795 (1992).

[28] F. Zhang, J. Chem. Phys. **99**, 53 (1996).

[29] W. H. Press, S. A. Teukolsky, W. T. Vetterling, and B. P. Flannery, *Numerical Recipes in Fortran: the Art of Scientific Computing* (Cambridge University Press, New York, 1992).

[30] K. Bolton and S. Nordholm, J. Comp. Chem. **113**, 320 (1994).

[31] R. A. Marcus and O. K. Rice, J. Phys. and Colloid Chem. **55**, 894 (1951).

[32] R. A. Marcus, J. Chem. Phys. **20**, 359 (1952).

[33] D. M. Wardlaw and R. A. Marcus, Adv. Chem. Phys. **70**, 231 (1988).

[34] D. L. Bunker, J. Chem. Phys. **40**, 1946 (1964).

[35] D. L. Bunker and W. L. Hase, J. Chem. Phys. **54**, 4621 (1973).

[36] T. Baer and W. L. Hase, *Unimolecular Reaction Dynamics. Theory and Experiments* (Oxford University Press, New York, 1996).

[37] G. H. Peslherbe, H. B. Wang, and W. L. Hase, Adv. Chem. Phys. **105**, 171 (1999).

[38] J. H. Hammersley and D. C. Handscomb, *Monte Carlo Methods* (Chapman and Hall, London, 1964).

[39] G. D. Billing, *Introduction to Molecular Dynamics and Chemical Kinetics* (Wiley, New York, 1996).

[40] J. Keck, J. Chem. Phys. **29**, 410 (1958).

[41] D. L. Bunker, J. Chem. Phys. **32**, 1001 (1960).

[42] D. G. Truhlar, J. Chem. Phys. **56**, 3189 (1972).

[43] J. T. Muckerman and M. D. Newton, J. Chem. Phys. **56**, 3191 (1972).

[44] A. Einstein, Verh. Dtsch. Phys. Ges. (Berlin) **19**, 82 (1917).

[45] L. Brillouin, J. Phys. Radium **7**, 353 (1926).

[46] J. B. Keller, Ann. Phys. (NY) **4**, 180 (1958).

Part II

Cases Studies

Chapter 4

DMBE-PES and dynamics study of HN_2 triatomic

J. Phys. Chem. A **107**, 7923–7930 (2003).

Accurate single-valued double many-body expansion potential energy surface for ground-state HN_2

L.A. Poveda and A.J.C. Varandas

Departamento de Química, Universidade de Coimbra
P-3049 Coimbra Codex, Portugal.

(Received: May 5, 2003; In final form: July 11, 2003)

Abstract

A single-valued double many-body expansion potential energy surface is reported for ground-state HN_2 by fitting accurate *ab initio* energies that have been suitably corrected by scaling for the $H-N_2$ and $N-NH$ regions. The energies of $\sim$ 900 geometries have been calculated at the multireference configuration interaction level, using aug-cc-pVQZ basis sets of Dunning and the full valence complete active space wavefunction as reference. The topographical features of the novel global potential energy surface are examined in detail.

1 Introduction

Several experimental and theoretical studies have attempted to elucidate the possible role of the HN_2 species as a critical step in various reactions. Although this molecule has never been observed experimentally, it has been postulated to be an important intermediary in thermal $\mathrm{De-NO}_x$ processes,[1, 2] with indirect evidence that suggests its existence through the three possible product channels proposed for the $NH_2 + NO$ reaction:

$$\mathrm{NH_2 + NO} \rightarrow \begin{cases} \mathrm{HN_2 + OH} \\ \mathrm{N_2 + H + OH} \\ \mathrm{N_2 + H_2O} \end{cases} \tag{1}$$

The experiments that are focused to determine the rate coefficient and the major pathway of reaction 1 are far from consistent: although the experimental studies vary widely, in regard to the branching ratio for OH production, none of the experiments observed H atoms.[3] This result, along with the assumed product channels, argues for the existence of the HN_2 species. However, a controversy persists from the kinetics modeling studies.[2, 4] In fact, while an estimate of $10^{-4}\,\mathrm{s}$ for the lifetime produces a reasonable match to experimental observations, the theoretical studies of HN_2 unimolecular decay predict a much shorter value of $10^{-8} - 10^{-9}\,\mathrm{s}$, for the ground vibrational state.[5–7]

Many *ab initio* studies of the reaction

$$\mathrm{H + N_2 \rightarrow HN_2} \tag{2}$$

has previously been made to characterize the geometry and energetics of the reactants, transition state, and products.[3] All previous calculations concluded that the title system is quasibound (the global minimun is located above the $H + N_2$ asymptote) with a barrier height to dissociation of $\sim 11\,\mathrm{kcal\,mol^{-1}}$. From such studies, a global potential energy surface was reported by Walch[5, 8, 9] and Koizumi *et al.*[6] for the $H + N_2$ channel. On the basis of a spline fit of the *ab initio* points calculated using the completed active space self-consistent field/externally contracted configuration interaction (CASSCF/CCI) method and two different basis sets, Walch and coworkers predicted, depending on the basis set used, a barrier height of 10.2 or $11.3\,\mathrm{kcal\,mol^{-1}}$ and a global minimum of 5.6 or $3.9\,\mathrm{kcal\,mol^{-1}}$ above the $H + N_2$ asymptote.

In a subsequent paper,[10] Walch and Partidge attempted a conclusive and accurate prediction of the HN_2 unimolecular decomposition. They reported a systematic study of the HN_2 energetics using the complete active space self-consistent field/internally contracted configuration interaction (CASSCF/ICCI) method and the cc-pVDZ, cc-pVTZ, cc-pVQZ, and cc-pV5Z basis sets of Dunning.[11, 12] From such results, an extrapolation to the complete basis set limit has been obtained, which yields a barrier height of $11.34\,\mathrm{kcal\,mol^{-1}}$ and a global minimum $4.31\,\mathrm{kcal\,mol^{-1}}$ above the $H + N_2$ asymptote. A slight difference between the constrained minimum path calculated at this level of theory and the one previously estimated using a potential energy surface[6] has induced those authors to conclude "…we are very confident of the theoretical lifetime predictions for the HN_2 radical".

In a more recent publication, Gu *et al.*[13] reported a high level CCSD(T)/aug-cc-pVQZ calculation of the stationary points for the title system. They predict the classical barrier height for the reaction $HN_2 \rightarrow H + N_2$ to be $10.7\,\mathrm{kcal\,mol^{-1}}$, thus lying $0.6\,\mathrm{kcal\,mol^{-1}}$ below the extrapolated value reported by Walch and Partridge.[10] In turn, the calculated[13] exothermicity for the reaction $H + N_2 \rightarrow HN_2$ is $3.8\,\mathrm{kcal\,mol^{-1}}$, thus slightly smaller than the extrapolated value[10] of $4.31\,\mathrm{kcal\,mol^{-1}}$. We may therefore argue that there is not a conclusive result yet for the HN_2 lifetime.

In this work we report the first realistic global potential energy surface for the ground electronic state of the title system, based on the double many-body expansion[14–17] (DMBE) method. Being a potential fragment of larger N_xH_y species, such as those of relevance in studying the synthesis of ammonia, it may also be of crucial importance in constructing the corresponding global DMBE forms for larger hydrogen-nitrogen polyatomic species. Specifically, the analytic HN_2 DMBE potential energy surface will be calibrated from $\sim$ 900 *ab initio* points that were calculated at the multireference configuration interaction (MRCI) level, using the full valence complete active space (FVCAS) reference function and the aug-cc-pVQZ (AVQZ) Dunning[11, 12] basis set. The *ab initio* energies calculated in this way have been subsequently corrected, using the double many-body expansion-scaled external correlation[18] (DMBE-SEC) method to extrapolate to the complete basis set/complete configuration interaction limits. As usual in

DMBE theory,[14–17] the potential energy surface so obtained shows the correct long-range behavior at all dissociation channels while providing a realistic representation at all interatomic separations (*e.g.*, Van der Waals wells at intermediate atom-diatom separations).

The paper is organized as follows. Section 2 describes the *ab initio* calculations that have been performed in the present work. In section 3, we examine the analytical representation of the potential energy surface; specifically, section 3.1 focuses on the two-body energy terms, whereas section 3.2 concentrates on the three-body energy terms. The main topographical features of the DMBE potential energy surface are discussed in section 4. Some concluding remarks are given in section 5.

2 *Ab initio* calculations

The *ab initio* calculations have been performed at the MRCI[19] level, using the FVCAS[20] wave function as reference. For the basis set we have selected the aug-cc-pVQZ (AVQZ) of Dunning,[11, 12] with the correlated *ab initio* calculations being performed using the MOLPRO[21] package. Approximately 900 grid points have been computed to map the potential energy surface over the region defined by $1.6 \leq R_{\mathrm{N}_2}/a_0 \leq 2.8$, $1.5 \leq r_{\mathrm{H-N}_2}/a_0 \leq 10.0$ and $0.0^\circ \leq \gamma \leq 90^\circ$ for $\mathrm{H-N}_2$ interactions, and $1.5 \leq R_{\mathrm{NH}}/a_0 \leq 2.4$, $1.5 \leq r_{\mathrm{N-NH}}/a_0 \leq 6.0$ and $0.0^\circ \leq \gamma \leq 180^\circ$ for $\mathrm{N-NH}$ interactions; r,R and γ are the corresponding atom-diatom Jacobi coordinates.

The *ab initio* energies calculated in this way have been subsequently corrected using the DMBE-SEC[16] method to account for the excitations beyond singles and doubles and, most importantly, for the incompleteness of the basis set. Thus, the total DMBE-SEC interaction energy is written as

$$V(\mathbf{R}) = V_{\mathrm{FVCAS}}(\mathbf{R}) + V_{\mathrm{SEC}}(\mathbf{R}) \tag{3}$$

where

$$V_{\mathrm{FVCAS}}(\mathbf{R}) = \sum_{\mathrm{AB}} V^{(2)}_{\mathrm{AB,FVCAS}}(R_{\mathrm{AB}}) + V^{(3)}_{\mathrm{ABC,FVCAS}}(R_{\mathrm{AB}}, R_{\mathrm{BC}}, R_{\mathrm{AC}}) \tag{4}$$

and

$$V_{\mathrm{SEC}}\left(\mathbf{R}\right)=\sum_{\mathrm{AB}}V^{(2)}_{\mathrm{AB,SEC}}\left(R_{\mathrm{AB}}\right)+V^{(3)}_{\mathrm{ABC,SEC}}\left(R_{\mathrm{AB}},R_{\mathrm{BC}},R_{\mathrm{AC}}\right) \tag{5}$$

with the first two terms of the SEC series expansion being given by

$$V^{(2)}_{\mathrm{AB,SEC}}\left(R_{\mathrm{AB}}\right)=\frac{V^{(2)}_{\mathrm{AB,FVCAS-CISD}}\left(R_{\mathrm{AB}}\right)-V^{(2)}_{\mathrm{AB,FVCAS}}\left(R_{\mathrm{AB}}\right)}{F^{(2)}_{\mathrm{AB}}} \tag{6}$$

$$\begin{gathered}V^{(3)}_{\mathrm{ABC,SEC}}\left(R_{\mathrm{AB}},R_{\mathrm{BC}},R_{\mathrm{AC}}\right)=\\ \frac{V^{(3)}_{\mathrm{ABC,FVCAS-CISD}}\left(R_{\mathrm{AB}},R_{\mathrm{BC}},R_{\mathrm{AC}}\right)-V^{(3)}_{\mathrm{ABC,SEC}}\left(R_{\mathrm{AB}},R_{\mathrm{BC}},R_{\mathrm{AC}}\right)}{F^{(3)}_{\mathrm{ABC}}}\end{gathered} \tag{7}$$

Following previous work,[16] the $F^{(2)}_{\mathrm{AB}}$ parameter in Eq. (6) has been chosen to reproduce the bond dissociation energy of the corresponding AB diatomic, while $F^{(3)}_{\mathrm{ABC}}$ has been estimated as the average of the two-body F-factors. Such a procedure leads to the following values: $F^{(2)}_{\mathrm{NN}}=0.758$, $F^{(2)}_{\mathrm{NH}}=0.948$, and $F^{(3)}_{\mathrm{NNH}}=0.885$.

3 Double many-body expansion potential energy surface

3.1 Two-body energy terms

The diatomic potential curves have been modeled using the extended Hartree-Fock approximate correlation energy method for diatomic molecules, including the united atom limit[22] (EHFACE2U), with the available parameters being determined by fitting experimental and *ab initio* data. Thus, they assume the general form[15, 22]

$$V=V_{\mathrm{EHF}}\left(R\right)+V_{\mathrm{dc}}\left(R\right) \tag{8}$$

where the label EHF refers to the extended Hartree-Fock type energy, and the label dc indicates the dynamical correlation energy. As usual, the latter is modeled semiempirically by[23]

$$V_{\mathrm{dc}}\left(R\right)=-\sum_{n=6,8,10}C_n\chi_n\left(R\right)R^{-n} \tag{9}$$

with the damping function for the dispersion coefficients assuming the form

$$\chi_n(R) = \left[1 - \exp\left(-A_n \frac{R}{\rho} - B_n \frac{R^2}{\rho^2}\right)\right]^n \tag{10}$$

In Eq. (10), A_n and B_n are auxiliary functions that are defined by

$$A_n = \alpha_0 n^{-\alpha_1} \tag{11}$$

$$B_n = \beta_0 \exp(-\beta_1 n) \tag{12}$$

where α_0, β_0, α_1 and β_1 are universal dimensionless parameters for all isotropic interactions:[14, 15] $\alpha_0 = 16.36606$, $\alpha_1 = 0.70172$, $\beta_0 = 17.19338$, and $\beta_1 = 0.09574$. In turn, the scaling parameter ρ is defined as

$$\rho = 5.5 + 1.25 R_0 \tag{13}$$

where $R_0 = 2\left(\langle r_{\mathrm{A}}^2\rangle^{1/2} + \langle r_{\mathrm{B}}^2\rangle^{1/2}\right)$ is the LeRoy[24] parameter for onset the undamped R^{-n} expansion, and $\langle r_{\mathrm{X}}^2\rangle$ is the expectation value of the squared radius for the outermost electrons of atom X (where $\mathrm{X} = A, B$). Finally, the exponential decaying portion of the EHF-type energy term assumes the general form

$$V_{\mathrm{EHF}}(R) = -\frac{D}{R}\left(1 + \sum_{i=1}^{n} a_i r^i\right) \exp(-\gamma r) \tag{14}$$

where

$$\gamma = \gamma_0 \left[1 + \gamma_1 \tanh(\gamma_2 r)\right] \tag{15}$$

$r = R - R_e$ is the displacement from the equilibrium diatomic geometry, and D and a_i $(i = 1, ..., n)$ are adjustable parameters to be obtained as described elsewhere.[15, 22] Specifically, the potential curve of ground-state $N_2\,(X^1\Sigma^+)$ has been calibrated by fitting simultaneously vibrational frequencies, Rydberg-Kleing-Rees (RKR) turning points,[25] and the *ab initio* energies calculated in the present work for the repulsive wing. Figure 1 shows that the final potential curve reproduces our calculated *ab initio* energies. In turn, for ground-state imidogen, NH $(X^3\Sigma^-)$, we have employed a previously reported potential energy curve[26] calibrated from the MRCI + Q *ab initio* points of Stallcop *et al.*[27] The numerical values of all parameters are, for both diatomic potentials, gathered in Table 1.

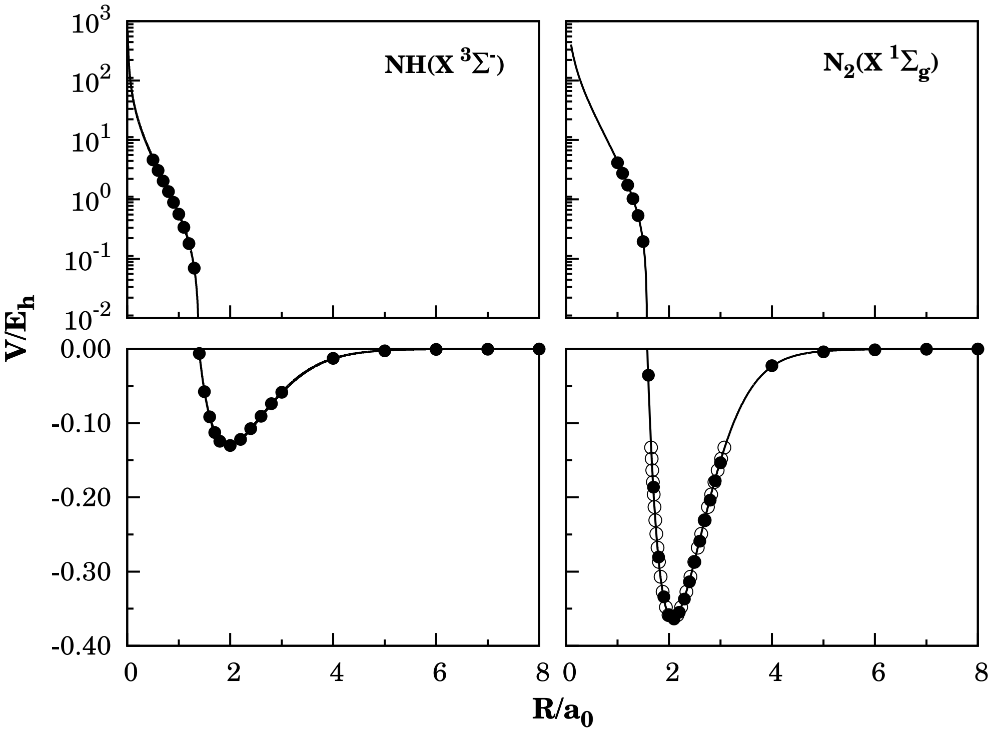

Figure 1. EHFACE2U potential energy curves for NH ($^3\Sigma^-$) and N$_2$ ($^1\Sigma_g$). Key for symbols: (○) Rydberg-Kleing-Ress data and (●) *ab initio* points.

Table 1. Parameters in the two-body extended Hartree-Fock energy.

	NH ($X^3\Sigma^-$)	N$_2$ ($X^1\Sigma_g$)
R_e/a_0	1.9650	2.0743
D/E_h	0.229 034 01	0.702 119 20
a_1/a_0^{-1}	2.146 641 73	2.211 672 95
a_2/a_0^{-2}	0.844 712 52	0.991 485 45
a_3/a_0^{-3}	0.525 908 29	1.553 769 29
γ_0/a_0^{-1}	1.563 792	1.678 669
γ_1/a_0^{-1}	0.661 116	0.674 118
γ_2/a_0^{-1}	0.282 985	0.716 957
$C_6/E_\mathrm{h}a_0^{-6}$	12.27	22.8
$C_8/E_\mathrm{h}a_0^{-8}$	232.6	442.6
$C_{10}/E_\mathrm{h}a_0^{-10}$	5775	9722

3.2 Three-body energy terms

In regard to the two-body energies, the three-body energy splits into several contributions. First, the three-body energy is divided into an extended Hartre-Fock part and a dynamical correlation part. For the three-body dynamical correlation, we select the form that was proposed elsewhere by one of us[28] for the water molecule, namely

$$V_{\mathrm{dc}}^{(3)} = \sum_i \sum_n f_i\left(\mathbf{R}\right) C_n^{(i)}\left(R_i, \theta_i\right) \chi_n\left(r_i\right) r_i^{-n} \tag{16}$$

where i label represents the $\mathrm{I} - \mathrm{JK}$ channel associated with the center of mass separation r_i; R_i is the $\mathrm{J} - \mathrm{K}$ bond distance, and $\cos\theta_i = \vec{r}_i\vec{R}_i/|\vec{r}_i\vec{R}_i|$. (For the notation, see Figure 1 of Ref. 16). For $n = 6$, 8 and 10, $C_n^{(i)}\left(R_i, \theta_i\right)$ are atom-diatom dispersion coefficients, which are given by

$$C_n^{(i)} = \sum_L C_n^L P_L\left(\cos\theta_i\right) \tag{17}$$

where $P_L\left(\cos\theta_i\right)$ denotes the L-th term of the Legendre polynomial expansion. In addition, the function $\chi_n\left(r_i\right)$ in Eq. (16) is the corresponding diatomic damping function. Moreover, $f_i\left(\mathbf{R}\right)$ is a switching function that is chosen from the requirement that its value must be $+1$ at $R_i = R_i^e$ and $r_i \rightarrow \infty$, and 0 when $R_i \rightarrow \infty$. One such a form is[28]

$$f_i = \frac{1}{2}\left\{1 - \tanh[\xi\left(\eta s_i - s_j - s_k\right)]\right\} \tag{18}$$

where $s_i = R_i - R_i^e$ (corresponding expressions apply to s_j, s_k, f_j and f_k), and η is a constant that is chosen to ensure the proper asymptotic behavior. Following previous work,[28] we adopt a value of $\eta = 3$. In addition, the parameter ξ has been assumed to be equal to $1.0\,a_0^{-1}$. Regarding the damping function $\chi_n\left(r_i\right)$, we still adopt Eq. (10) but replace R by the center-of-mass separation for the relevant atom-diatom channel. In addition, the value of ρ has been assumed by considering R_0 in Eq. (13) as the average of the LeRoy parameters for NO and SiH, which leads to $\rho = 15.9$.

3.3 Three-body dynamical correlation energy

The $L = 0$, 2 and 4 components of the atom-diatom dispersion coefficients have been considered, with the involved internuclear dependencies being estimated as

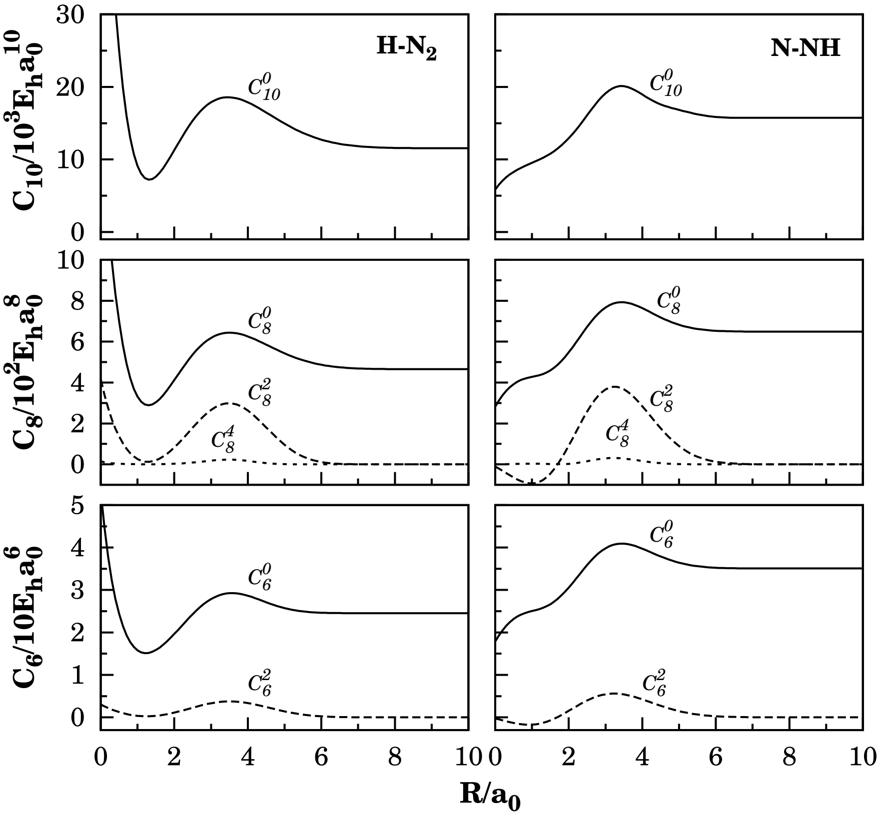

Figure 2. Dispersion coefficients for atom-diatom channels of HN_2, as a function of the corresponding internuclear distance R.

reported elsewhere,[29] *i.e.*, by using the dipolar polarizabilities calculated in the present work at the MRCI level of theory jointly with the generalized Slater-Kirkwood approximation.[30] The atom-diatom dispersion coefficients thus calculated were then fitted to the form

$$C_n^{\mathrm{A-BC}}(R) = C_n^{\mathrm{AB}} + C_n^{\mathrm{AC}} + D_{\mathrm{M}}\left(1+\sum_{i=1}^{3} a_i r^i\right)\exp\left(-a_1 r - \sum_{i=2}^{3} b_i r^i\right) \qquad (19)$$

where $r = R - R_{\mathrm{M}}$ is the displacement relative to the position of the maximum. The parameters that resulted from such fits are reported in Table 2, whereas the internuclear dependence of the dispersion coefficients are shown in Figure 2.

As noted out elsewhere,[28] Eq. (16) causes an overestimation of the dynamical correlation energy at the atom-diatom dissociation channels. To correct such a behavior, we have multiplied the two-body dynamical correlation energy for the

Table 2. Numerical values of the parameters in Eq (19).

	$C_6^0\,(R)$	$C_6^2\,(R)$	$C_8^0\,(R)$	$C_8^2\,(R)$	$C_8^4\,(R)$	$C_{10}^0\,(R)$
			$\mathrm{H-N_2}$			
R_M/a_0	3.5667	3.5090	3.5026	3.4863	3.4870	3.4608
$D_\mathrm{M}/E_\mathrm{h}$	4.7294	3.7419	178.7058	298.9732	22.9832	7028.8116
a_1/a_0^{-1}	1.277 799 82	0.851 582 13	1.131 083 35	0.884 602 42	0.879 306 21	1.090 186 28
a_2/a_0^{-2}	0.300 410 55	0.184 349 94	0.277 939 09	0.196 563 42	0.198 953 65	0.275 794 87
a_3/a_0^{-3}	−0.003 100 54	−0.000 969 88	−0.000 106 74	−0.000 933 54	0.000 965 52	0.001 704 86
b_2/a_0^{-2}	0.315 677 76	0.269 098 43	0.135 718 43	0.293 195 75	0.945 261 28	0.096 086 57
b_3/a_0^{-3}	0.047 870 65	0.028 844 54	0.009 978 24	0.044 310 67	0.216 377 09	0.006 945 65
			$\mathrm{N-NH}$			
R_M/a_0	3.4400	3.2316	3.4371	3.2506	3.2187	3.4352
$D_\mathrm{M}/E_\mathrm{h}$	5.8549	5.5978	143.9529	379.7076	31.0459	4394.6574
a_1/a_0^{-1}	1.595 253 94	1.026 484 21	1.584 495 87	0.931 566 40	1.644 505 86	−0.073 743 22
a_2/a_0^{-2}	0.708 758 04	0.270 832 16	0.703 651 10	0.182 778 32	0.865 513 27	−0.607 106 28
a_3/a_0^{-3}	0.104 478 27	0.015 983 88	0.103 522 65	−0.001 626 53	0.139 612 00	0.497 138 66
b_2/a_0^{-2}	0.284 813 14	0.270 234 30	0.289 780 70	0.318 737 43	0.684 793 26	0.553 195 06
b_3/a_0^{-3}	$1.0\text{x}10^{-8}$	$1.0\text{x}10^{-8}$	$1.0\text{x}10^{-8}$	$1.0\text{x}10^{-8}$	$1.0\text{x}10^{-8}$	0.106 836 28

i-th pair by $f_i\left(\mathbf{R}\right)$ and correspondingly for channels j and k. This ensures[28] that the only two-body contribution at the i-th channel is that of JK.

3.4 Three-body extended Hartree-Fock energy

By removing, for a given triatomic geometry, the sum of the two-body energy terms from the corresponding DMBE–SEC interaction energies (Eq. (3)), which was defined with respect to the infinitely separated ground-state atoms, one obtains the total three-body energy. Therefore, by subtracting the three-body dynamical correlation contribution [Eq. (16)] from the total three-body energy that is calculated in that way, one obtain the three-body extended Hartree-Fock energy contribution. To represent the latter, we use the following three-body distributed-polynomial[31] form

$$V_{\mathrm{EHF}}^{(3)} = \sum_{j=1}^{5} P^{(j)}\left(Q_1, Q_2, Q_3\right) \prod_{i=1}^{3} \{1 - \tanh[\gamma_i^j \left(R_i - R_i^{j,ref}\right)]\} \tag{20}$$

where $P^{(j)}\left(Q_1, Q_2, Q_3\right)$ is the j-th polynomial. To sixth-order, this assumes the form

$$\begin{aligned}
P^j\left(Q_1, Q_2, Q_3\right) &= c_1 + c_2 Q_1 + c_3 Q_3 + c_4 Q_1^2 + c_5 S_{2a}^2 + c_6 Q_1 Q_3 + c_7 S_{2b}^2 + c_8 Q_1^3 \\
&+ c_9 Q_1 S_{2a}^2 + c_{10} S_3^3 + c_{11} Q_1^2 Q_3 + c_{12} Q_1 S_{2b}^2 + c_{13} Q_3 S_{2a}^2 + c_{14} Q_1^4 \\
&+ c_{15} Q_1^2 S_{2a}^2 + c_{16} S_{2a}^4 + c_{17} Q_1 S_3^3 + c_{18} Q_1^3 Q_3 + c_{19} Q_1^2 S_{2b}^2 \\
&+ c_{20} Q_1 Q_3 S_{2a}^2 + c_{21} Q_3 S_3^3 + c_{22} S_{2a}^2 S_{2b}^2 + c_{23} Q_1^5 + c_{24} Q_1^3 S_{2a}^2 \\
&+ c_{25} Q_1 S_{2a}^4 + c_{26} Q_1^2 S_3^3 + c_{27} S_{2a}^2 S_3^3 + c_{28} Q_1^4 Q_3 + c_{29} Q_1^3 S_{2b}^2 \\
&+ c_{30} Q_1^2 Q_3 S_{2a}^2 + c_{31} Q_1 Q_3 S_3^3 + c_{32} Q_1 S_{2a}^2 S_{2b}^2 + c_{33} Q_3 S_{2a}^4 \\
&+ c_{34} S_{2b}^2 S_3^3 + c_{35} Q_1^6 + c_{36} Q_1^4 S_{2a}^2 + c_{37} Q_1^2 S_{2a}^4 + c_{38} Q_1^3 S_3^3 \\
&+ c_{39} Q_1 S_{2a}^2 S_3^3 + c_{40} S_{2a}^6 + c_{41} S_3^6 + c_{42} Q_1^5 Q_3 + c_{43} Q_1^4 S_{2b}^2 \\
&+ c_{44} Q_1^3 Q_3 S_{2a}^2 + c_{45} Q_1^2 Q_3 S_3^3 + c_{46} Q_1^2 S_{2a}^2 S_{2b}^2 + c_{47} Q_1 Q_3 S_{2a}^4 \\
&+ c_{48} Q_1 S_{2b}^2 S_3^3 + c_{49} Q_3 S_{2a}^2 S_3^3 + c_{50} S_{2a}^4 S_{2b}^2
\end{aligned} \tag{21}$$

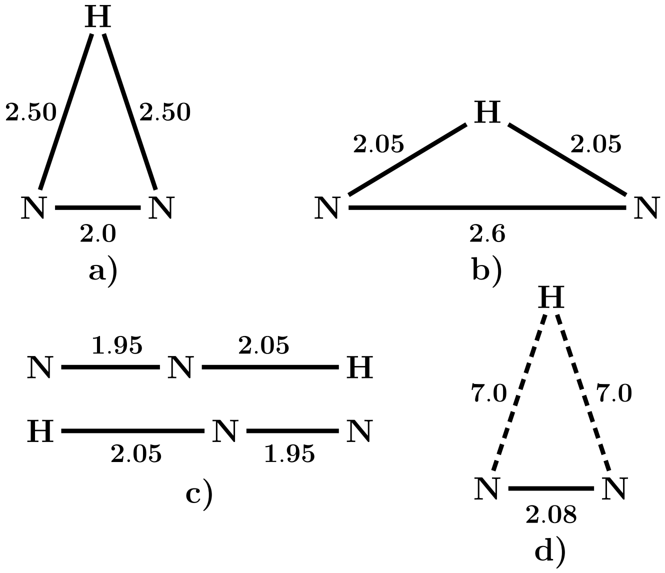

Figure 3. Reference geometries (with distances in atomic units, a.u.) for the three-body EHF portion of the potential energy surface. See text for details.

where $S_{2a}^2 = Q_2^2 + Q_3^2$, $S_{2b}^2 = Q_2^2 - Q_3^2$, and $S_3^3 = Q_3^3 - 3Q_2^2Q_3$, with Q_i $(i = 1 - 3)$ being symmetry coordinates that are defined, for the j-th polynomial, by

$$\begin{pmatrix} Q_1 \\ Q_2 \\ Q_3 \end{pmatrix} = \begin{pmatrix} \sqrt{\frac{1}{3}} & \sqrt{\frac{1}{3}} & \sqrt{\frac{1}{3}} \\ 0 & \sqrt{\frac{1}{2}} & -\sqrt{\frac{1}{2}} \\ \sqrt{\frac{2}{3}} & -\sqrt{\frac{1}{6}} & -\sqrt{\frac{1}{6}} \end{pmatrix} \begin{pmatrix} R_1 - R_1^{j,ref} \\ R_2 - R_2^{j,ref} \\ R_3 - R_3^{j,ref} \end{pmatrix} \tag{22}$$

Figure 3 displays the reference geometries that are used to define the displacement coordinates used to write the five EHF-type polynomials in Eq. (20). Note that the first and second polynomials (which refer to the first and second sets of coefficients in Table 3) are respectively centered in structures a) and b) of Figure 3. In turn, two other polynomials employ the same set of coefficients (third column of Table 3), which are centered in structure c) of Figure 3. The last polynomial, $P^{(5)}(Q_1, Q_2, Q_3)$, is centered at reference geometry d) in Figure 3, which lies close to the equilibrium structure of the weakly bound $H \cdots N_2$ van der Waals species. Note that this includes up to cubic terms only, because this proved to be sufficient for our fitting purposes. To obtain $R_i^{j,ref}$, we have first assumed their values to coincide with the bond distances of the associated stationary points,

Table 3. Numerical values of the extended Hartree-Fock energy [Eq. (20)].

Coefficients	$P^{(1)}$	$P^{(2)}$	$P^{(3)}, P^{(4)}$	$P^{(5)}$
c_1/a_0^0	−35.35722711	50.89357137	0.64204663	−0.00037787
c_2/a_0^{-1}	1.43122305	−8.20511664	−1.57901897	−0.00190090
c_3/a_0^{-1}	−9.87617675	−44.75381891	−0.94137581	−0.00261274
c_4/a_0^{-2}	−18.80416915	26.48543000	1.81933025	0.00029084
c_5/a_0^{-2}	−21.78867083	32.57491690	0.60735250	−0.00057451
c_6/a_0^{-2}	−11.07940674	−33.13037794	0.52335000	−0.00038871
c_7/a_0^{-2}	5.01128977	5.08772061	0.25855378	0.00055106
c_8/a_0^{-3}	0.96613480	−3.99536563	−1.18504903	–
c_9/a_0^{-3}	−0.77697807	10.11891334	−0.63735021	−0.00076654
c_{10}/a_0^{-3}	−0.92099871	4.10517993	0.12413155	–
c_{11}/a_0^{-3}	−6.01375589	−16.78809143	−0.38833222	−0.00104352
c_{12}/a_0^{-3}	0.90509055	−16.20351814	0.11928222	0.00074255
c_{13}/a_0^{-3}	−5.14061355	−17.17930402	−0.82128727	–
c_{14}/a_0^{-4}	−3.40765945	3.78922878	0.63973511	–
c_{15}/a_0^{-4}	−1.88077926	3.13322630	−0.26288962	–
c_{16}/a_0^{-4}	−2.68379376	5.69616150	0.17067403	–
c_{17}/a_0^{-4}	4.45588653	−5.81699928	−0.18560723	–
c_{18}/a_0^{-4}	−4.05543497	−7.84835242	0.12054093	–
c_{19}/a_0^{-4}	1.70217322	−11.08806364	−0.17812786	–
c_{20}/a_0^{-4}	−3.39696345	−5.64359911	0.34470547	–
c_{21}/a_0^{-4}	0.52809629	1.62229042	−0.24358630	–
c_{22}/a_0^{-4}	0.96757611	1.49907056	0.29036290	–
c_{23}/a_0^{-5}	0.07042292	−0.52463644	−0.18613603	–
c_{24}/a_0^{-5}	−1.13489314	2.85006561	0.39057365	–
c_{25}/a_0^{-5}	1.21500520	0.84486292	−0.10864732	–
c_{26}/a_0^{-5}	0.90416261	−3.39970612	−0.08699980	–
c_{27}/a_0^{-5}	−0.37424676	0.07267052	−0.09095443	–
c_{28}/a_0^{-5}	−1.41649184	−0.91682855	−0.10631151	–
c_{29}/a_0^{-5}	−0.04756769	−1.68254925	0.26417945	–
c_{30}/a_0^{-5}	0.61305975	−3.72605017	0.33025474	–
c_{31}/a_0^{-5}	1.84502268	3.16507583	0.00837542	–
c_{32}/a_0^{-5}	−0.58400452	−1.42401824	−0.07300291	–
c_{33}/a_0^{-5}	−0.13609210	−2.12175750	−0.21211357	–
c_{34}/a_0^{-5}	−0.05015587	1.04011399	0.23138290	–
c_{35}/a_0^{-6}	−0.12738976	0.02661556	0.03395371	–
c_{36}/a_0^{-6}	0.62237114	−0.02032757	−0.18379018	–

Table 3. Continue.

c_{37}/a_0^{-6}	0.10324812	0.78316160	0.05864884	–
c_{38}/a_0^{-6}	−0.42328134	−0.45490030	−0.05717854	–
c_{39}/a_0^{-6}	0.76664528	−0.77298638	0.03477564	–
c_{40}/a_0^{-6}	−0.21436778	0.45857204	0.00603242	–
c_{41}/a_0^{-6}	−0.03021494	0.16268811	−0.04950996	–
c_{42}/a_0^{-6}	−0.17424122	0.08238406	−0.03113967	–
c_{43}/a_0^{-6}	0.10050895	−0.35417930	0.04913502	–
c_{44}/a_0^{-6}	0.61827911	−1.07342606	−0.00694684	–
c_{45}/a_0^{-6}	0.42896861	1.11079450	0.04085605	–
c_{46}/a_0^{-6}	−0.37356092	−0.70735541	−0.27048435	–
c_{47}/a_0^{-6}	0.29520788	−1.15920924	−0.04881234	–
c_{48}/a_0^{-6}	−0.37797059	0.53374300	−0.18376155	–
c_{49}/a_0^{-6}	0.23373482	0.20831280	0.02121087	–
c_{50}/a_0^{-6}	0.16170869	−0.34419861	0.15943928	–
γ_1^j/a_0^{-1}	1.30	0.40	1.55	1.00
γ_2^j/a_0^{-1}	1.10	1.35	−0.55, 1.55	0.35
γ_3^j/a_0^{-1}	1.10	1.35	1.55, −0.55	0.35
$R_1^{j,ref}/a_0$	2.00	2.60	2.05	2.08
$R_2^{j,ref}/a_0$	2.50	2.05	1.95, 4.00	7.00
$R_3^{j,ref}/a_0$	2.50	2.05	4.00, 1.95	7.00

and, subsequently, relaxed this condition via a trial-and-error least-squares fitting procedure. The nonlinear range-determining parameters γ_i^j have been optimized in a similar way. Thus, the complete set of parameters totals 160 linear coefficients c_i, 15 nonlinear coefficients γ_i^j, and 15 reference geometries $R_i^{j,ref}$. Their optimal numerical values are collected in Table 3. A total of 913 points have been used for the calibration procedure, with the energies covering a range up to 500 kcal mol^{-1} above the $\mathrm{H} + \mathrm{N}_2$ asymptote.

Table 4 shows the stratified root-mean-squared deviation (rmsd) values of the final potential energy surface with respect to the fitted and nonfitted *ab initio* energies. This table shows that the final potential energy surface is able to fit the region of major chemical interest (308 *ab initio* points with energies up to 40 kcal mol^{-1}) with a high accuracy (rmsd = 0.256 kcal mol^{-1}). This regions includes the global minimum and the transition state for the H + N_2 dissociation process. The major deviations correspond to points close to the conical intersection (thus, they have not been included in the fitting procedure, to warrant a behavior of the final single-valued form that is as smooth as possible) and at high repulsive regions of the potential surface. Clearly, the DMBE potential energy surface obtained in this way accurately reproduces all fitted and nonfitted *ab initio* points, up to $500\,\mathrm{kcal\,mol^{-1}}$.

Figure 4 illustrates the quality of the final fitted form. The profiles correspond to minimum energy cuts for 10 distinct values of γ, whereas the displayed *ab initio* points form a small set of the total number of points used in the fitting procedure; they have been calculated by optimizing $R_{\mathrm{N_2}}$ at specified values of γ and $r_{\mathrm{H-N_2}}$. The two conical intersections that result for T-shape and linear configurations are clearly visible in Figure 4. We emphasize that the regions close to such topological features are smoothed out (*i.e.*, this resemble avoided intersections) in the single-valued representation used in the present work. Thus, the points close to the actual crossing seam (indicated in the plot as unfilled circles) have not been included in the fitting procedure such as to avoid spoiling its quality at the regions of more chemical interest.

4 Major features of potential energy surface

Figure 5 and Figure 6 illustrate the major topographical features of the present HN_2 DMBE potential energy surface that has been calculated in the present work. Specifically, Figure 5 shows energy contours for a H atom moving around a N_2 ground-state diatomic whose bond length is partially relaxed for each position of the H atom. The corresponding plot for a N atom moving around NH is presented in Figure 6. The salient features from these plots are some of the most relevant stationary points for the title system. A characterization of their attributes (geometry, energy, and vibrational frequencies) is reported in Table 5. Also included for comparison in this table are the results that have been obtained from other potential energy surfaces. Note that we have calculated a denser grid of energies in the vicinity of some stationary points which were then used to fit a local polynomial form to obtain an optimum prediction of the spectroscopic

Table 4. Stratified root-mean-square deviations (in kcal mol^{-1}).

Energy	number of points	maximum deviation	rmsd[a]
20	224	0.90	0.152
40	308	2.36	0.256
60	540	9.06	0.620
80	570	9.06	0.714
100	597	9.06	0.765
200	825	10.06	0.935
300	887	10.06	0.982
500	913	10.06	1.070

[a] Root-mean-saquare deviation

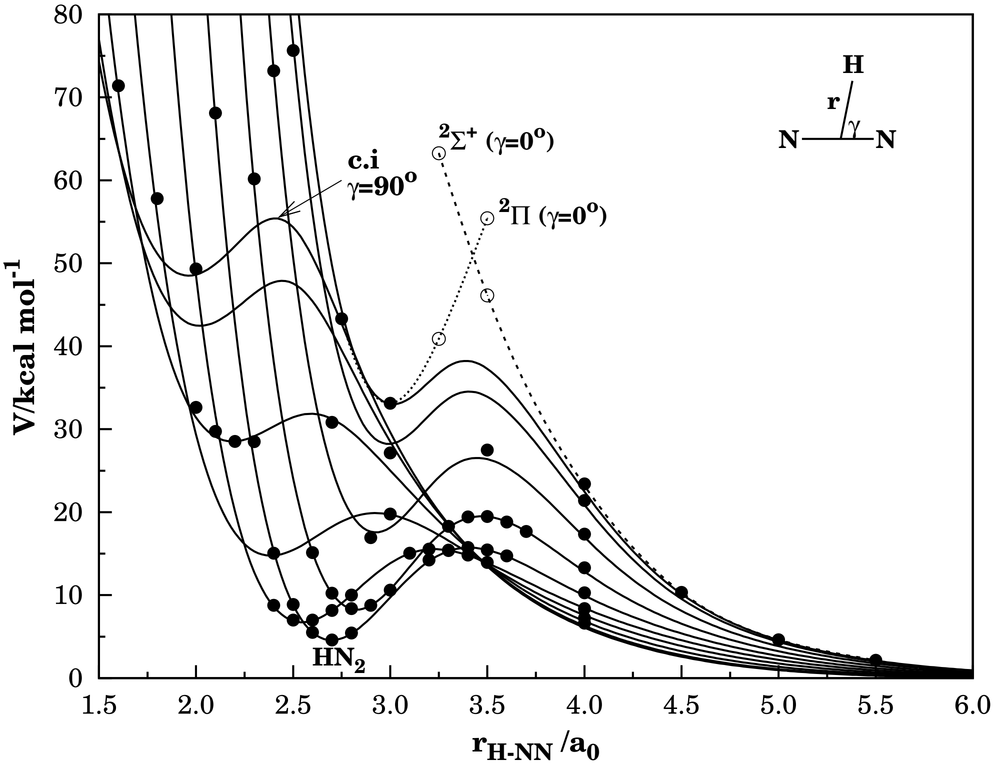

Figure 4. Selected cuts of the HN_2 potential energy surface. The figure shows 10 minimum energy cuts for fixed values of γ as a function of the distance $r_{\mathrm{H-N_2}}$. Note the avoided crossing for T-shape and linear configurations. Unfilled points correspond to geometries close to the conical intersection, which have not been included in the least-squares fitting procedure..

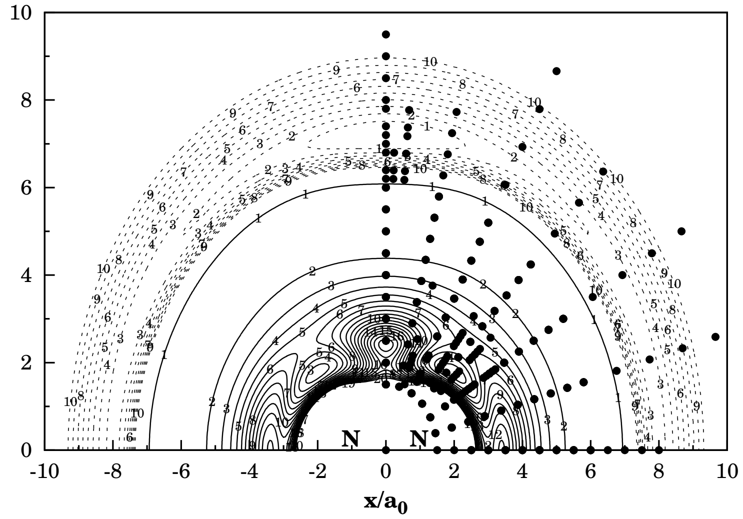

Figure 5. Isoenergy contour plot for a H atom moving around a partially relaxed N_2 diatomic ($1.8\,a_0 \leq R_{N_2} \leq 2.4\,a_0$), which lies along the x-axis with the center of the bond fixed at the origin. Contours are equally spaced by $0.005\,E_h$, starting at $-0.3640\,E_h$. Contours in dashed lines emphasize the van der Waals minimum; they are equally spaced by $0.000005\,E_h$, starting at $-0.36414\,E_h$. Also shown are the calculated *ab initio* points for the H atom moving around N_2 diatomic, whose bond distance varied between $1.6\,a_0$ to $2.8\,a_0$.

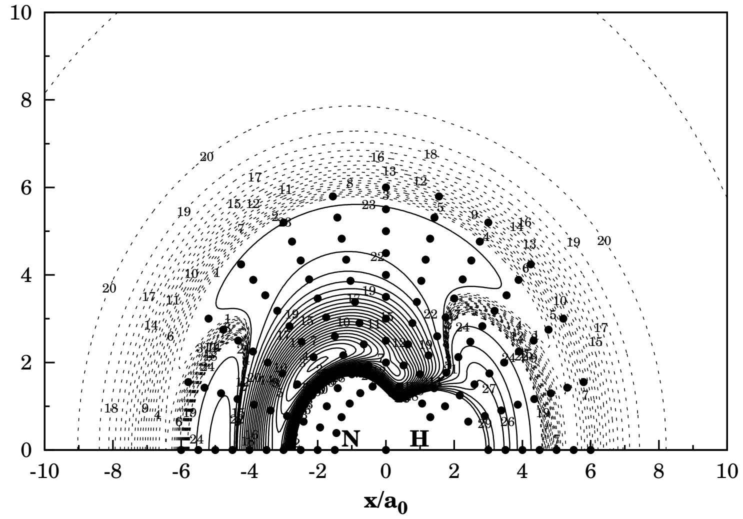

Figure 6. Isoenergy contour plot for a N atom moving around a partially relaxed NH diatomic ($1.8\,a_0 \leq R_{\mathrm{NH}} \leq 2.3\,a_0$), which lies along the x-axis with the center of the bond fixed at the origin. Contours are equally spaced by $0.01\,E_h$, starting at $-0.355\,E_h$. The contours in dashed are equally spaced by $0.0002\,E_h$, starting at $-0.1340\,E_h$. Also shown are the calculated *ab initio* points for the N atom around a NH diatomic, whose bond distance varied over a range from $1.5\,a_0$ to $2.4\,a_0$.

Table 5. Stationary points of DMBE potential energy surface, for various features.

Property	MRCI[a]	CASSCF/CCI[b]	PES[c]	DMBE[d]
		Global minimun		
R_1/a_0	2.227	2.253	2.250	2.226
R_2/a_0	3.586	3.556	3.599	3.595
R_3/a_0	1.981	2.017	1.966	1.983
V/E_h	−0.3568			−0.3568
$\Delta V^e\,(\mathrm{kcal\,mol^{-1}})$	4.52	4.31[f]	3.8	4.52
$\omega_1\,(\mathrm{N-H})\,/\mathrm{cm^{-1}}$	2916	2577	2607	2887
$\omega_2\,(\mathrm{N-N})\,/\mathrm{cm^{-1}}$	1818	1931	1809	1862
$\omega_3\,(\mathrm{bend})\,/\mathrm{cm^{-1}}$	1118	1106	1137	1086
		Saddle point for $\mathrm{H+N_2}$ reaction		
R_1/a_0	2.124	2.173	2.139	2.125
R_2/a_0	4.135	4.231	4.190	4.136
R_3/a_0	2.685	2.641	2.703	2.688
V/E_h	−0.3399			−0.3399
$\Delta V^g\,(\mathrm{kcal\,mol^{-1}})$	10.60	11.34[f]	11.4	10.60
$\omega_1\,(\mathrm{N-H})\,/\mathrm{cm^{-1}}$	$1619i$	$1387i$	$1658i$	$1640i$
$\omega_2\,(\mathrm{N-N})\,/\mathrm{cm^{-1}}$	2155	2027	1980	2102
$\omega_3\,(\mathrm{bend})\,/\mathrm{cm^{-1}}$	762	668	763	763
		Saddle point for $\mathrm{H-N_2}$ isomerization		
R_1/a_0	2.324	2.390		2.326
R_2/a_0	2.285	2.291		2.281
R_3/a_0	2.285	2.291		2.281
V/E_h	−0.2867			−0.2868
$\Delta V^g\,(\mathrm{kcal\,mol^{-1}})$	48.51	51.6		48.44
$\omega_1\,(\mathrm{N-H})\,/\mathrm{cm^{-1}}$	2676			2753
$\omega_2\,(\mathrm{N-N})\,/\mathrm{cm^{-1}}$	1660			1668
$\omega_3\,(\mathrm{bend})\,/\mathrm{cm^{-1}}$	$2278i$			$2295i$

[a] From this work, from a fit to a Taylor-series-type expansion around the stationary point; see text. [b] From ref. 8. [c] From ref. 6. [d] This work. [e] Relative to the $\mathrm{H+N_2}$ asymptote. [f] From ref. 10, value extrapolated to the complete basis set limit. [g] Relative to the global minimum.

properties at the correlated *ab initio* level. Table 6 summarizes the properties obtained for other relevant stationary points, including the shallow van der Waals minimum in Figure 5 for intermediate $H - N_2$ distances.

Clearly, the current HN_2 DMBE potential energy surface provides an accurate representation of the properties of the global minimum and the two most important transition states: one that is associated with the reaction $H + N_2 \rightarrow NH + N$, the other to the HN_2 isomerization process. Specifically, the barrier height for the process $HN_2 \rightarrow H + N_2$ is predicted to be $10.6\,\mathrm{kcal\,mol^{-1}}$ before inclusion of the zero-point energy correction. Thus, it lies slightly below the $11.3\,\mathrm{kcal\,mol^{-1}}$ extrapolation of Walch and Partridge,[10] while being very similar to the result reported by Gu *et al.*[13] These authors have used an aug-cc-pVQZ basis set and the CCSD(T) method, having predicted a barrier height of $10.7\,\mathrm{kcal\,mol^{-1}}$. As they also observed, experience suggests that such a barrier may be further reduced when larger basis sets and higher levels of theory are used.[8, 13] The fact that our prediction lies slightly below the best-available theoretical estimates may then provide an indication that the DMBE-SEC method can reliably be used to extrapolate the *ab initio* energies to the complete basis set/configuration interaction limit.

We now turn to the global minimum, which is predicted in the present work to be $4.5\,\mathrm{kcal\,mol^{-1}}$ above the $H + N_2$ asymptote. Thus, it lies close to the Walch and Partridge[10] extrapolation of $4.31\,\mathrm{kcal\,mol^{-1}}$ and only slightly above the Gu *et al.*[13] prediction of $3.8\,\mathrm{kcal\,mol^{-1}}$. This result may not be surprising as the literature shows that the estimated values for the barrier height have a tendency to show a more stable trend ($\sim 11\,\mathrm{kcal\,mol^{-1}}$) than the calculated exothermicity for the reaction $HN_2 \rightarrow H + N_2$. We may attribute such a behavior to the fact that the exothermicity is dependent on the level of *ab initio* theory and basis set used in a more subtle way[3, 8, 10, 13] (the best reported values cover the range $3.0 - 5.6\,\mathrm{kcal\,mol^{-1}}$). In fact, the calculated values reflect the difficulties that are usually encountered by the theoretical methods in describing both the short-range and long-range range interactions in a balanced way.

The saddle point for the HN_2 isomerization process is located at a T-shaped configuration prior to the conical intersection, lying $48.5\,\mathrm{kcal\,mol^{-1}}$ above the $H + N_2$ asymptote. Both such features are visible in Figure 5, being located along

Table 6. Geometries and energies of other important stationary points.

Property	van der Waals $H\cdots N_2$	linear TS $N-H\cdots N$	 $N\cdots H\cdots N$
R_1/a_0	2.076	6.379	4.740
R_2/a_0	7.231	1.943	2.370
R_3/a_0	7.231	4.436	2.370
V/E_h	−0.3642	−0.1338	−0.0933
$\Delta V/\mathrm{kcal\,mol^{-1}}$	-0.07^a	2.26^b	23.15^b
$\omega_1\,(\mathrm{N-H})\,/\mathrm{cm^{-1}}$	55	618	$2163i$
$\omega_1\,(\mathrm{N-N})\,/\mathrm{cm^{-1}}$	2335	4711	538
$\omega_1\,(\mathrm{bend})\,/\mathrm{cm^{-1}}$	14	$138i$	978

[a]Relative to the $H+N_2$ asymptote. [b]Relative to the $N+NH$ asymptote.

the y-axis at $\sim 2\,a_0$. Thus, our estimated barrier height is somewhat smaller than the value of 51.6 kcal mol^{-1} reported by Walch,[8] which may have implications on the lifetime of the HN_2 metastable species.

As shown in Figure 5, the present calculations predict a C_{2v} van der Waals minimum with a well depth of 0.07 kcal mol^{-1} relative to the $H+N_2$ asymptote. It is a very shallow minimum, which indicates an almost free rotation of the H atom around N_2. Thus, in reality, the correct location of the lowest energy that is associated with such a weakly bound structure can hardly be warranted to correspond to a C_{2v}-type structure, despite the care taken in performing the least-squares fit and the appreciable number (46 in total) of *ab initio* points that have been calculated for $r_{\mathrm{H-N_2}} \geq 6.5\,a_0$.

Table 5 and 6 show that the spectroscopic properties of all stationary points in the DMBE potential energy surface are similar to the frequencies obtained when a Taylor-series type expansion is instead used to fit a dense grid of energies in the vicinity of such points. Indeed, the average percentage errors in the calculated frequencies is 1.0 % for the global minimum, saddle point for the $H+N_2$ reaction, and saddle point for the HN_2 isomerization.

Figure 7 shows a contour plot for the linear $N-H-N$ stretching. The main

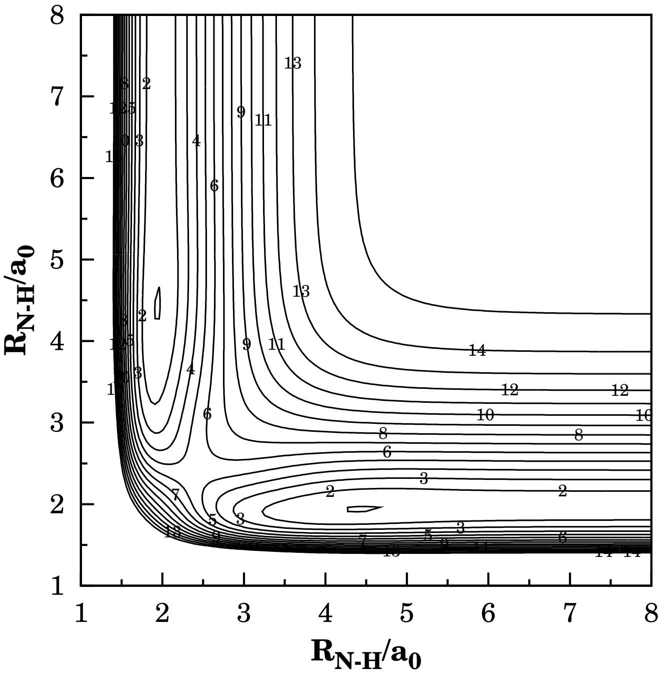

Figure 7. Isoenergy contour plot for the stretching of the two NH bonds in linear N − H − N. Contours are equally spaced by $0.009\,E_\mathrm{h}$ starting at $-0.1335\,E_\mathrm{h}$. The two equivalent structures NH · · · N and N · · · HN indicate linear transition states, which appear as hydrogen-bonded minima, with respect to the stretching coordinate (see text).

features are the two equivalent NH · · · N hydrogen-bond type structures, and the saddle point for the H-atom exchange process. Note that such structures are not true minima in three-dimensional configuration space, but rather are linear transition states as indicated by the dashed contours in Figure 6. Indeed, they have a positive curvature with respect to NH · · · N stretching but a negative one with respect to bending. Table 6 summarizes the geometries, energies, and vibrational frequencies of such stationary points.

Finally, in Figure 8, we show a contour plot for the C_{2v} insertion of a H atom into N_2. Although the dashed contours might suggest the resulting linear configuration to be a minimum, it is indeed a saddle point because it has a negative curvature with respect to the bending mode (H-atom insertion). In fact, such a "minimum" corresponds, in reality, to the saddle point that connects the two NH · · · N hydrogen-bond type structures that are observed in Figure 7. Also

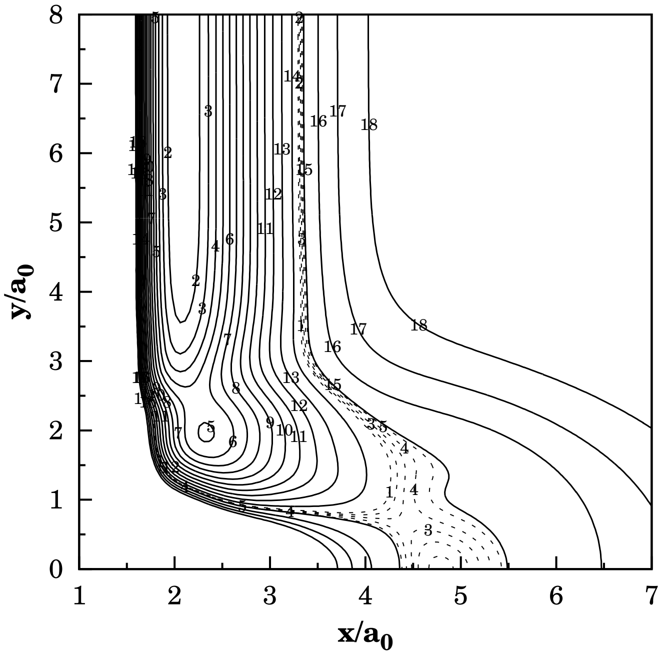

Figure 8. Isoenergy contour plot for the C_{2v} insertion of H atom into a N_2 diatomic. Contours are equally spaced by $0.02\,E_h$, starting at $-0.3641\,E_\mathrm{h}$. Contours in dashed lines are equally spaced by $0.002\,E_\mathrm{h}$, starting at $-0.0932\,E_h$.

visible from Figure 8 is a shallow "minimum" located at $r_{\mathrm{H-N_2}} \approx 2.0\,a_0$, which is related to the saddle point that connects the two equivalent metastable structures shown in Figure 5. Finally, for large atom-diatom separations, we observe the very shallow $\mathrm{H}\cdots\mathrm{N_2}$ van der Waals minimum that has been already discussed previously (see Figure 5 and Table 6).

5 Concluding remarks

We have reported a single-valued DMBE potential energy surface for ground-state HN_2 based on a realistic representation of the long-range forces and a fit to accurate *ab initio* calculations. The various topographical features of the new potential energy surface have been carefully examined, and compared with previous calculations for the title system, most importantly a potential energy surface previously reported by Walch and collaborators.[5, 6, 8, 9] The geometries and spectroscopy of the main stationary points for the HN_2 global minimum, transition state for dissociation and isomerization barrier height are reproduced very accurately when compared with the best available theoretical estimates. We emphasize that the predicted barrier height for dissociation lies below the best available estimates,[10, 13] suggesting that the DMBE-SEC method offers a reliable means to extrapolate accurate correlated energies to the basis set/CI limit. Thus, we speculate that dynamics calculations employing the new potential energy surface are likely to predict a lifetime for the HN_2 species even shorter than previously reported estimates. Since the global minimum is predicted to lie $4.5\,\mathrm{kcal\,mol^{-1}}$ above the $H + N_2$ asymptote (which is slightly above the best estimates reported in the literature), we further argue that the stability of such a structure is yet unresolved although it definitely appears to be a metastable one. To summarize, the DMBE potential energy surface reported in the present work is globally valid and fits accurately our *ab initio* calculations, thence being recommended for future dynamics studies of the $H + N_2 \rightarrow HN_2 \rightarrow HN + N$ reaction.

Acknowledgments

This work has the financial support of European Community, through Contract No. HPRN-CT-2002-00170, and Fundação para a Ciência e a Tecnologia, Portugal.

References and Notes

[1] Miller, J. A.; Branch, M. C.; Kee, R. J. *Combust. Flame* **1981**, *81*, 43.

[2] Miller, J. A.; Bowman, C. G. *Prog. Energy Combust. Sci.* **1989**, *15*, 287.

[3] see Ref. 5.; references therein.

[4] Glarbor, P. G.; Miller, J. A.; Kee, R. J. *Combust. Flame* **1986**, *177*, 65.

[5] Walch, S. P.; Duchovic, R. J.; Rohlfing, C. M. *J. Chem. Phys.* **1989**, *90*, 3230.

[6] Koizumi, H.; Schatz, G. C.; Walch, S. P. *J. Chem. Phys.* **1991**, *95*, 4130.

[7] Gou, Y.; Thompsom, D. L. *J. Chem. Phys.* **2002**, *116*, 3670.

[8] Walch, S. P. *J. Chem. Phys.* **1990**, *93*, 2384.

[9] Walch, S. P. *J. Chem. Phys.* **1991**, *95*, 4277.

[10] Walch, S. P.; Partridge, H. *Chem. Phys. Lett.* **1995**, *233*, 331.

[11] Dunning, T. H. *J. Chem. Phys.* **1989**, *90*, 1007.

[12] Kendall, R.; Dunning Jr., T.; Harrison, R. *J. Chem. Phys.* **1992**, *96*, 6769.

[13] Gu.; Xie.; Schaefer. *J. Chem. Phys.* **1998**, *108*, 8029.

[14] Varandas, A. J. C. *J. Mol. Struct. Theochem* **1985**, *120*, 401.

[15] Varandas, A. J. C. *Adv. Chem. Phys.* **1988**, *74*, 255.

[16] Varandas, A. J. C. *Chem. Phys. Lett.* **1992**, *194*, 333.

[17] Varandas, A. J. C. *Lecture Notes in Chemistry*; Laganá, A., Riganelli, A., Eds.; Springer: Berlin, 2000; Vol. 75 of *Lecture Notes in Chemistry*, p 33.

[18] Varandas, A. J. C. *J. Chem. Phys.* **1989**, *90*, 4379.

[19] Werner, H.-J.; Knowles, P. J. *J. Chem. Phys.* **1988**, *89*, 5803.

[20] Knowles, P. J.; Werner, H.-J. *Chem. Phys. Lett.* **1985**, *115*, 259.

[21] Werner, H.-J.; Knowles, P. J., MOLPRO is a package of *ab initio* programs written by H.-J. Werner, P. J. Knowles, with contributions from J. Almlöf, R. D. Amos, M. J. O. Deegan, S. T. Elbert, C. Hampel, W. Meyer, K. A. Peterson, R. Pitzer, A. J. Stone, P. R. Taylor, R. Lindh, (1998).

[22] Varandas, A. J. C.; Silva, J. D. *J. Chem. Soc. Faraday Trans.* **1992**, *88*, 941.

[23] Varandas, A. J. C. *Mol. Phys.* **1987**, *60*, 527.

[24] Le Roy, R. J. *Spec. Period. Rep. Chem. Soc. Mol. Spectrosc.* **1973**, *1*, 113.

[25] Edwards, S.; Roncin, J. Y.; Launay, F.; Rostas, F. *J. Mol. Spectrosc.* **1993**, *162*, 257.

[26] Varandas, A. J. C.; Rodrigues, S. P. J. *J. Chem. Phys.* **1997**, *106*, 9647.

[27] Stallcop, J. R.; Jr., C. H. B.; Partridge, H.; Langhoff, S. R.; Levin, E. *J. Chem. Phys.* **1992**, *97*, 5578.

[28] Varandas, A. J. C. *J. Chem. Phys.* **1996**, *105*, 3524.

[29] Varandas, A. J. C.; Rodrigues, S. P. J. *Chem. Phys. Lett.* **1995**, *245*, 66.

[30] Matías, M. A.; Varandas, A. J. C. *Mol. Phys.* **1990**, *70*, 623.

[31] Martínez-Nuñez, E.; Varandas, A. J. C. *J. Phys. Chem.* **2000**, *000*, 0.

J. Phys. Chem. A (in press)

Recalibrated double many-body expansion potential energy surface and dynamics calculations for HN_2

P.J.S.B. Caridade, L.A. Poveda, S.P.J. Rodrigues and A.J.C. Varandas

Departamento de Química, Universidade de Coimbra
3004-535 Coimbra, Portugal

(in press)

Abstract

A single-sheeted double many body expansion potential energy surface is reported for the lowest doublet state of HN_2 by fitting additional multireference configuration interaction energies in the $N \cdots NH$ channel. A stratified analysis of the root-mean squared error indicates an accuracy superior to that achieved for the previously reported form. Detailed dynamical tests are also performed for the $N + NH$ reaction using both the quasi-classical trajectory method and capture theory, and the results compared with available empirical data. The vibrational resonances of the HN_2 metastable radical are also calculated and compared with previous theoretical predictions.

1 Introduction

Interest in N_xH_y systems has been increasing in recent years due to their key role in the nitrogen chemistry, both in gas phase and gas-solid interface.[1] Specifically, HN_2 is a well known intermediary in the NO pollutant combustion reduction[2–6] and in the non-catalytic radical mechanism that leads to ammonia formation.[7] In a recent publication, Dickinson *et al.*[8] stressed the importance of transport coefficients in $H - N_2$ binary mixtures to model hydrogen-air flames.

Although the HN_2 radical is recognized as a metastable species, it has apparently never been explicitly detected by spectroscopic methods. In fact, only Selgren *et al.*[9] reported results based on neutralization ion beam studies in which they observed radiative transitions (wavelength range $2700 - 4500\,\text{Å}$) between $n = 3$ Rydberg state of $^2A'$ and $^2A''(\pi)$ using potassium targets. As claimed by the authors,[9] this may constitute the first spectroscopic detection of the radical, although no other studies confirmed their analysis. An intriguing aspect of the HN_2 radical is the long-standing discussion concerning its lifetime. Several theoretical results[10–16] have predicted hydrodinitrogen to be short-lived (10^{-8}–10^{-9} s), while kinetic models of the thermal selective non-catalytic reduction of NO by ammonia require it to have a long lifetime in order to rationalize the experimental results.[2, 17, 18] Quoting Gu *et al.*,[14] "harmony between kinetic modeling studies and experiment can be achieved by postulating a lifetime of 10^{-4} s for the HN_2 species", thus 4 orders of magnitude or so larger than the theoretical predictions. However, an *ad-hoc* manipulation of the HN_2 lifetime may not be the proper solution as other groups[19] alerted for missing reactions and chemical equilibria in the considered kinetic models, *e.g.*, the fast dissociation/recombination process $HN_2 \rightleftharpoons H + N_2$.[3, 5, 20, 21] Moreover, Selgren *et al.*[9] concluded that the HN_2 lifetime should be less than $0.5\,\mu$s.

To study this and other aspects related to the HN_2 radical, we have recently reported[15] a global single-sheeted DMBE (double many-body expansion) potential energy surface for the ground electronic doublet state of the title system ($^2A'$), hereafter denoted as DMBE I. This function has been calibrated from accurate multi-reference configuration interaction[22] (MRCI) energies using the aug-cc-pVQZ (AVQZ) basis set of Dunning,[23, 24] which have been subsequently corrected semi-empirically by using the DMBE-scaled external correlation (DMBE-SEC) method[25] to extrapolate to the complete basis set/complete configuration interaction limit. As for applications, the DMBE I potential energy surface has been employed[16] both in classical and quantum studies of various unimolecular and bimolecular reactions, as well as to calculate $H-N_2$ transport and diffusion coefficients.[8] Although the accuracy of DMBE I is estimated to be $1.0\,\mathrm{kcal\,mol^{-1}}$, a spurious barrier of $0.5\,\mathrm{K}$ has been detected after publication in its long-range component, a finding also reported by Dickinson *et al.*[8] Although this feature is unlikely to have any practical implications in reaction dynamics at temperatures of relevance in most physical and chemical processes, this may not be the case for low and ultra-low temperature regimes. This prompted us to carry out further high level *ab initio* calculations for the $N+NH$ channel with a view to improve the reliability of the fitted potential energy surface. Such a work will be described in section 2.

Experimentally, the rate constant of the $N+NH$ exothermic reaction has been the subject of a single direct measurement by Hack *et al.*[26] It has also been studied[20, 21, 27–29] indirectly based on assumptions that may have introduced some arbitrariness on its temperature dependence, and even on its value at room temperature. In a previous publication, we have presented a quasi-classical trajectory/statistical mechanics study of the $N+NH \rightleftharpoons N_2+H$ reactive system using the DMBE I potential energy surface. Although a fortuitous coincidence has led to good agreement with the reported experimental data and even with the suggested $T^{0.5}$ temperature-dependence of the rate constant proposed by several authors, such a result has later been found to have been due to an improper sampling of the translational energy in Ref. 16. The present recalibration of the DMBE potential energy surface (DMBE II) then gave us the possibility of correcting such an error when studying the bimolecular reactions in section 3. Finally, the spectroscopy of the metastable HN_2 species on DMBE II is reported in section 4. For convenience, several energy units have been used: $1\,E_\mathrm{h} = 219474.63\,\mathrm{cm^{-1}} = 627.509552\,\mathrm{kcal\,mol^{-1}}$, and $1\,a_0 = 0.529177249\,\text{Å}$.

2 Potential energy surface

According to DMBE method,[30] the single-valued potential energy surface assumes the form of a cluster expansion, where

$$V^{(n)} = V^{(n)}_{\mathrm{EHF}} + V^{(n)}_{\mathrm{dc}} \tag{1}$$

and $V^{(n)}_{\mathrm{EHF}}$ and $V^{(n)}_{\mathrm{dc}}$ are the n-body extended Hartree-Fock and dynamical correlation energies, respectively. Due to the modularity of DMBE, the recalibration procedure affects only the three-body EHF energy term, and hence we need to consider only this term in the present work (the reader is addressed to Ref. 15 for other details). Note that, due to a misprint in Eq. (16) of Ref. 15, there should be a negative sign in the three-body correlation energy term.

The three-body extended Hartree-Fock energy contribution assumes the distributed polynomial[31] form

$$V^{(3)}_{\mathrm{EHF}} = \sum_{j=1}^{7} P^{(j)}\left(Q_1, Q_2, Q_3\right) \prod_{i=1}^{3} \{1 - \tanh[\gamma_i^{(j)} \left(R_i - R_i^{j,ref}\right)]\} \tag{2}$$

where $P^{(j)}$ is the j-th polynomial written in terms of Q-coordinates, as defined in Eq. (22) of Ref. 15. In this work, we have used two polynomials of sixth-order and one of second-order centered in different C_{2v} geometries, and two other of six-order plus two of second-order centered at collinear geometries. The least-squares fit has been done as previously,[15] but employing now 1074 MRCI/aug-cc-pVQZ energies suitably scaled by the DMBE-SEC method.[25] Extra care has been put on medium and long-range regions of the $\mathrm{N} - \mathrm{NH}$ channel, as it plays a critical role in the calculation of the rate constant. Table 1 gathers the numerical values of the coefficients in Eq. (2) for the $\mathrm{HN_2}$ $(^2A')$ DMBE II potential energy surface.

The quality of the recalibrated function can be assessed from the stratified root-mean-square deviation (rmsd) reported in Table 2. Although chemical accuracy (rmsd $\leq 1.0\,\mathrm{kcal\,mol^{-1}}$) is attained up to $2400\,\mathrm{kcal\,mol^{-1}}$ above the absolute minimum, one should claim only qualitative agreement at high energies due to the many electronic states that may involved at such regimes and which cannot be accounted by the single-sheeted function in Eq. (1). For regions of interest in the $\mathrm{HN_2}$ unimolecular process (up to $40\,\mathrm{kcal\,mol^{-1}}$) the rmsd is smaller

Table 1. Numerical values of the extended Hartree-Fock energy [Eq. (2)] for DMBE II.

Coefficients	$P^{(1)}$	$P^{(2)}$	$P^{(3)}, P^{(4)}$	$P^{(5)}, P^{(6)}$	$P^{(7)}$
c_1/a_0^0	−2.90158828	−1.09895154	0.43148722	−0.01393543	0.61624970
c_2/a_0^{-1}	0.39854688	−1.69106240	−0.95862589	−0.00024907	−0.02188633
c_3/a_0^{-1}	2.94933842	3.36317027	−0.58841950	0.00242847	0.20525174
c_4/a_0^{-2}	−0.78513361	0.10992062	1.29460955	−0.00434843	0.02877663
c_5/a_0^{-2}	−1.80500677	−2.33894400	0.96554945	−0.00221630	−0.01318154
c_6/a_0^{-2}	1.97749883	1.50276065	1.11369917	0.00532874	0.07051309
c_7/a_0^{-2}	−0.27097707	0.63566828	0.14998792	−0.00245328	−0.07077306
c_8/a_0^{-3}	0.57672213	−1.12637632	−0.80000327	–	–
c_9/a_0^{-3}	0.55527103	−1.49242602	−1.07619112	–	–
c_{10}/a_0^{-3}	−0.42551937	−0.55456205	0.26787584	–	–
c_{11}/a_0^{-3}	2.38311147	2.25672572	−0.82818877	–	–
c_{12}/a_0^{-3}	−0.00353209	1.29534898	−0.14270347	–	–
c_{13}/a_0^{-3}	0.20356871	1.74408593	−0.26975878	–	–
c_{14}/a_0^{-4}	−0.11362941	−0.03375161	0.56955400	–	–
c_{15}/a_0^{-4}	−1.07422542	−0.68556436	0.21002786	–	–
c_{16}/a_0^{-4}	−0.82883383	−0.12020553	0.50601702	–	–
c_{17}/a_0^{-4}	0.24120702	0.98954397	−0.04587553	–	–
c_{18}/a_0^{-4}	0.43799969	0.66171509	0.69059305	–	–
c_{19}/a_0^{-4}	0.48111176	1.15964005	−0.09833499	–	–
c_{20}/a_0^{-4}	−1.55264396	0.95992522	0.32456237	–	–
c_{21}/a_0^{-4}	0.27216868	0.35208058	0.22641765	–	–
c_{22}/a_0^{-4}	0.40173631	−0.06031124	0.18601286	–	–
c_{23}/a_0^{-5}	0.03482064	−0.17962009	−0.17925566	–	–
c_{24}/a_0^{-5}	−0.40095342	−0.40538698	0.00220662	–	–
c_{25}/a_0^{-5}	0.15075947	0.45669342	−0.20627251	–	–
c_{26}/a_0^{-5}	−0.34618938	0.42740386	−0.30410104	–	–
c_{27}/a_0^{-5}	−0.18318810	−0.22534593	−0.08384832	–	–
c_{28}/a_0^{-5}	0.30507092	0.69189675	−0.26672995	–	–
c_{29}/a_0^{-5}	0.18675391	0.57350723	0.30028707	–	–
c_{30}/a_0^{-5}	−1.00100158	0.34435255	−0.41344558	–	–
c_{31}/a_0^{-5}	−0.65963394	−0.58579651	−0.30281359	–	–
c_{32}/a_0^{-5}	0.10598629	−0.18417302	0.17856970	–	–
c_{33}/a_0^{-5}	0.62854741	−0.61234370	0.01915613	–	–
c_{34}/a_0^{-5}	0.16916360	−0.03171154	0.00567697	–	–
c_{35}/a_0^{-6}	0.01037597	0.01504439	0.04748843	–	–
c_{36}/a_0^{-6}	−0.00111739	−0.10727743	−0.02430580	–	–
c_{37}/a_0^{-6}	0.01033702	0.12956587	0.12168874	–	–
c_{38}/a_0^{-6}	−0.12249987	0.09328784	0.10491031	–	–

Table 1. Continue.

c_{39}/a_0^{-6}	0.37473174	−0.02091609	0.12687845	–	–
c_{40}/a_0^{-6}	−0.19645700	0.16339023	0.12780671	–	–
c_{41}/a_0^{-6}	−0.01456897	−0.00861288	−0.03862858	–	–
c_{42}/a_0^{-6}	0.17422860	0.01503896	0.11260976	–	–
c_{43}/a_0^{-6}	0.04993295	0.10767799	−0.12218007	–	–
c_{44}/a_0^{-6}	−0.23819751	0.21241282	0.11121738	–	–
c_{45}/a_0^{-6}	0.07810318	−0.04887950	0.11388144	–	–
c_{46}/a_0^{-6}	−0.11316908	0.03710686	−0.19009228	–	–
c_{47}/a_0^{-6}	0.12781642	−0.47284812	0.11996366	–	–
c_{48}/a_0^{-6}	−0.08263450	−0.01902151	−0.03046820	–	–
c_{49}/a_0^{-6}	0.01158495	0.06946968	0.18556616	–	–
c_{50}/a_0^{-6}	0.12600504	−0.15261714	0.23484907	–	–
$\gamma_1^{(j)}/a_0^{-1}$	1.58	0.10	1.60	0.29	0.69
$\gamma_2^{(j)}/a_0^{-1}$	1.16	1.33	$-0.39, 1.33$	$1.27, 1.02$	0.54
$\gamma_3^{(j)}/a_0^{-1}$	1.16	1.33	$1.33, -0.39$	$1.02, 1.27$	0.54
$R_1^{(j),ref}/a_0$	1.85	2.55	1.90	7.461	4.80
$R_2^{(j),ref}/a_0$	2.75	2.15	$2.20, 4.10$	$1.961, 5.50$	2.40
$R_3^{(j),ref}/a_0$	2.75	2.15	$4.10, 2.20$	$5.50, 1.961$	2.40

Table 2. Stratified maximum and root-mean-square deviations (in $\mathrm{kcal\,mol^{-1}}$).

Energy	Number of points	DMBE I[a]	DMBE II[b]
20	229	0.152	0.046
40	335	0.337	0.366
60	541	0.654	0.414
80	570	0.753	0.509
100	596	0.815	0.608
120	667	0.905	0.641
140	689	1.005	0.667
160	824	1.049	0.644
200	966	1.151	0.726
500	1046	1.325	0.773
1200	1071	4.087	0.785

[a] Ref. 15. [b] This work.

than 0.4 kcal mol^{-1} while for those relevant to study the N + NH reaction (up to 146 kcal mol^{-1}) it is still only 0.7 kcal mol^{-1}. A significant improvement has then been achieved with respect to DMBE I, with the data being probably fitted within the accuracy of the *ab initio* energies themselves.

A stationary-point analysis has been performed on the DMBE II potential energy surface, being the results compared with those obtained from other *ab initio* methods,[12–15] as well as DMBE I,[15] in Tables 3 and 4. For the most important topographical characteristics, the DMBE I[15] and DMBE II functions are seen to be hardly distinguishable, even through the reported normal mode analysis (the maximum deviation in the calculated vibrational frequencies is 20 cm^{-1}). Such an agreement shows that the distributed-polynomial technique allows a refinement of the previously reported function without severely modifying regions that were considered as properly described by DMBE I. As for the HN_2 decomposition process, the classical barrier is located at 10.6 kcal mol^{-1} above the HN_2 minimum. Although this is slightly lower than the early *ab initio* value of Walch *et al.*[11] and the extrapolated result of Walch and Partridge,[13] the agreement with the proposed estimate of Gu *et al*[14] (10.0 ± 1.0 kcal mol^{-1}) is very good. The calculated exothermicity for this process is 4.6 kcal mol^{-1}, in excellent agreement with MRCI calculations[15] and with the Walch and Partridge[13] extrapolated value of 4.3 kcal mol^{-1}. Our result is also only 0.7 kcal mol^{-1} higher than the value reported by Gu *et al*[14] using CCSD(T). An interesting feature of the work of Gu *et al.*[14] is the wrong exothermicity that B3LYP calculations predict. Using the same basis set as CCSD(T), the HN_2 is predicted to be stable by 3.3 kcal mol^{-1} in relation to the $H + N_2$ asymptote, although the barrier height towards dissociation is close to the predicted value from the present work. As shown in Table 4, the recalibrated DMBE surface predicts also a new $NH \cdots N$ van der Waals minimum lying 0.2 kcal mol^{-1} below the N + NH asymptote. For completeness, we reported also the $H \cdots N_2$ van der Waals minimum and the linear transition state structures in Table 4.

Due to similarities between the two DMBE potential energy surfaces except for the N − NH interaction channel, we restrict the discussion to this region. Shown as a contour plot in Figure 1 is a cut of the DMBE II potential energy surface for the N − NH interaction, with the diatomic molecule being partially

Table 3. Major stationary points of the DMBE II potential energy surface, compared with the most recent available data.

Feature	Property	KSW[a]	CASSCF/ICCI[b]	CCSD(T)[c]	MRCI[d]	DMBE I[e]	DMBE II[f]
Global minimun	R_1/a_0	2.250	2.25	2.223	2.227	2.226	2.226
	R_2/a_0	3.600	3.814	3.588	3.586	3.595	3.595
	R_3/a_0	1.966	2.097	1.985	1.981	1.983	1.983
	$\Delta V^g/\mathrm{kcal\,mol}^{-1}$	3.8	4.31[h]	3.8	4.5	4.5	4.5
	ω_1(N–H)/cm^{-1}	2653			2916	2887	2875
	ω_2(N–N)/cm^{-1}	1826			1818	1862	1842
	ω_3(bend)/cm^{-1}	1047			1118	1086	1096
Saddle point for $H + N_2$ reaction	R_1/a_0	2.139	2.17	2.121	2.124	2.125	2.125
	R_2/a_0	4.190	4.149	4.145	4.135	4.136	4.137
	R_3/a_0	2.703	2.754	2.688	2.685	2.688	2.688
	$\Delta V^i/\mathrm{kcal\,mol}^{-1}$	11.4	11.34	10.7	10.6	10.6	10.6
	ω_1(N–H)/cm^{-1}	1667i			1619i	1640i	1624i
	ω_2(N–N)/cm^{-1}	1990			2155	2102	2104
	ω_3(bend)/cm^{-1}	749			762	763	778
Saddle point for $H - N_2$ isomerization	R_1/a_0				2.324	2.326	2.326
	R_2/a_0				2.285	2.281	2.281
	R_3/a_0				2.285	2.281	2.281
	$\Delta V^i/\mathrm{kcal\,mol}^{-1}$				48.5	48.4	48.4
	ω_1(N–H)/cm^{-1}				2676	2753	2753
	ω_2(N–N)/cm^{-1}				1660	1668	1671
	ω_3(bend)/cm^{-1}				2278i	2295i	2275i

[a]Ref. 12. [b]Ref. 13. [c]Ref. 14, considering the aug-cc-pVQZ basis set. [d]Ref. 15, fitting a polynomial to a dense grid around each stationary point. [e]Ref. 15. [f]this work. [g]Relative to the $H + N_2$ asymptote. [h]Extrapolated to the basis set limit, see Ref. 13. [i]Relative to the global minimum.

Table 4. Geometries and energies of other important stationary points.

	van der Waals			linear TS
	min.	min.	TS	
Property	$H\cdots N_2$	$N-H\cdots N$	$N\cdots N-H$	$N-H-N$
R_1/a_0	2.075	7.467	6.846	4.758
R_2/a_0	7.112	1.961	1.965	2.379
R_3/a_0	7.112	5.506	8.811	2.379
E/E_h	−0.3642	−0.1305	−0.1304	−0.0937
$\Delta V/\mathrm{kcal\,mol}^{-1}$	-0.1^a	-0.2^b	-0.1^b	22.9^b
ω_1(N–H)/cm^{-1}	69	3198	4451	2828i
ω_2(N–N)/cm^{-1}	2337	45	119	567
ω_3(bend)/cm^{-1}	18	16	56i	907

[a] Relative to the H + N_2 asymptote (in kcal mol^{-1}). [b] Relative to the N + NH asymptote (in kcal mol^{-1}).

relaxed. The salient feature is the smaller attractive nature of the entrance region that leads to the HN_2 minimum (cf. Figure 6 of Ref. 15). Also visible are a collinear $NH\cdots N$ van der Waals minimum and two collinear stationary points: one is the saddle point for NH − N bending leading to isomerization, the other refers to the $N\cdots HN$ van der Waals minimum which lies bellow the N + NH asymptote by 0.1 kcal mol^{-1} (see also Table 4). A more quantitative assessment of the fit is shown in the two panels of Figure 2, which display one-dimensional cuts ($a-h$) (these are indicated by the dashed lines in Figure 1) for different NH distances and Jacobi angles together with the newly calculated *ab initio* data. As Figure 2 shows, the new DMBE form describes within a few cm^{-1} the DMBE-SEC corrected MRCI energies. Also relevant is the absence of the spurious collinear barrier that appeared in DMBE I.[15]

3 The reaction N + NH → N_2 + H and its reverse

The N + NH → N_2 + H reaction and its reverse are important steps in the combustion of ammonia[32, 33] and hydrazine.[21, 34] Although being a simple triatomic reaction, only one direct experimental measurement of the rate constant has been

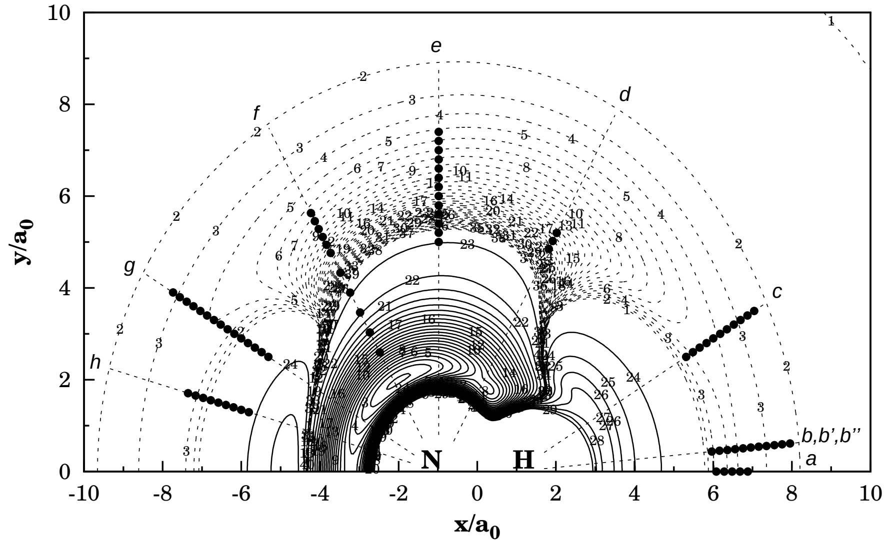

Figure 1. Isoenergy contour plot for the N around a partial relaxed NH molecule $1.8 \le R_{\rm NH}/a_0 \le 2.3$. Solid contours start at $-0.355\,E_h$ and equally spaced by $0.01\,E_h$, while the dashed ones start at $-0.134\,E_h$ [N + NH(R_e) energy] with increments of $0.0001\,E_h$. Shown in solid dots are the newly calculated MRCI *ab initio* geometries.

reported[26] by using a quasi-static flash photolysis cell (for room temperature). Indirectly, Whyte and Phillips[28] have studied the NH decomposition produced by $N + NH_2$ by laser-induced fluorescence, having concluded that the total removal rate constant through reaction with atomic nitrogen is $7.28 \pm 0.42\,{\rm cm}^3\,{\rm mol}^{-1}\,{\rm s}^{-1}$. This value has been subsequently used by Zhan *et al.*[29] to study the production of NF (b) and IF (B) in the $NH_3 - F - F_2 - CF_3I$ reaction system. Since Whyte and Phillips[28] reports the total removal rate constant, Zhan *et al.*[29] have used half of this value, giving the same probability to the NH (X) and NH (A) channels. Other crude indirect estimates were reported in the literature[21, 27, 35] based on simple formalisms. Unfortunately, our previous dynamics calculations[16] were themselves affected by an error in the collision energy sampling, favoring high energy values. Since DMBE II should be more accurate than DMBE I, only dynamics calculations on the former will be reported.

Following previous work,[16] we have used the QCT method[36] assuming a thermalized ro-vibrational distribution for the NH reactant molecule (see Ref. 37 for details), with the internal energies (E_{vj}) being determined by solving numeri-

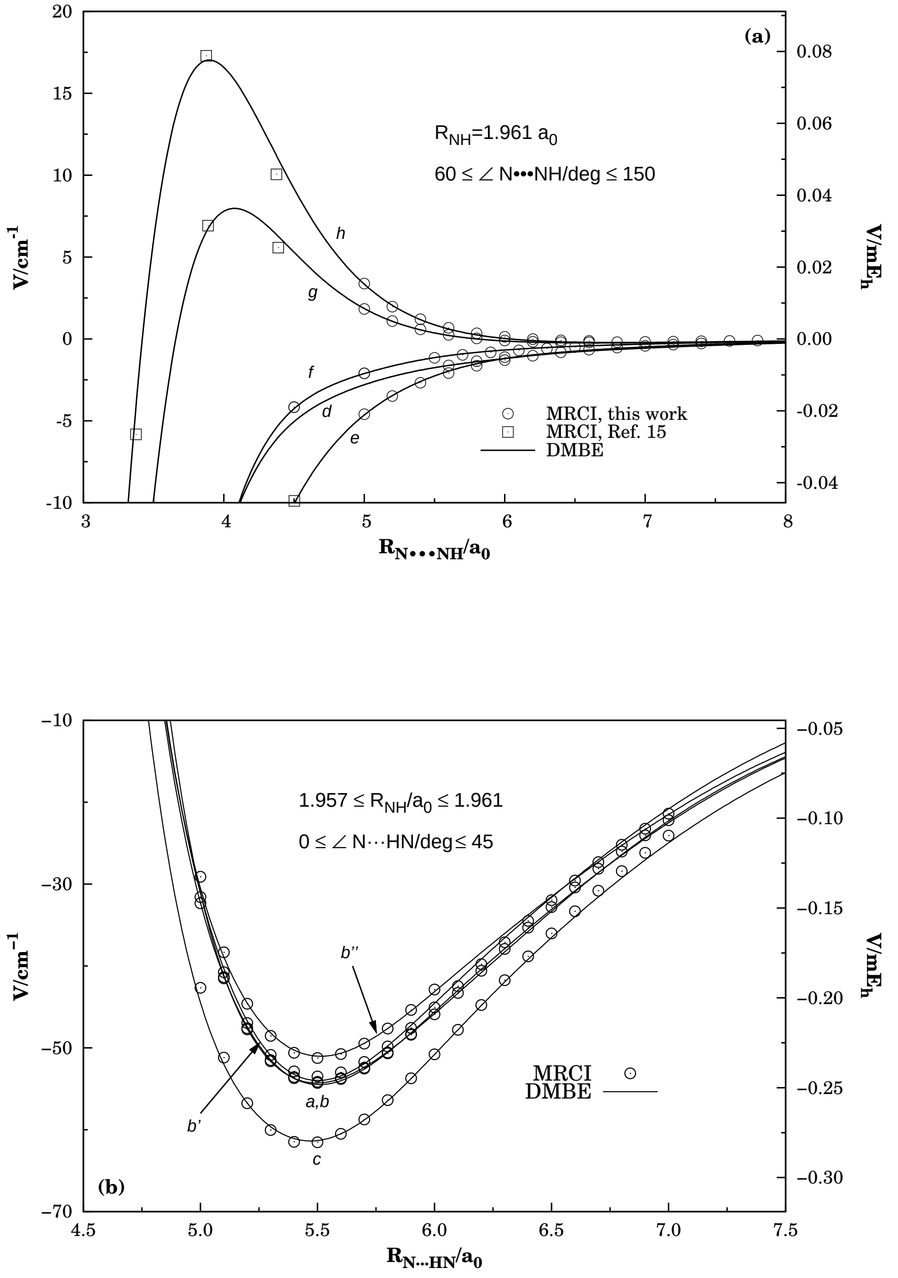

Figure 2. One-dimensional cuts for the long range interaction showing *ab initio* points calculated in the present work (open dots) and previously calculated (open squares): (a) NH · · · N and (b) N · · · NH. The key letters refer to the dotted lines shown in Figure 1.

cally[38] the time-independent Schrödinger equation and the realistic NH diatomic curve[39] used in modeling both DMBE I and DMBE II. Translational energy sampling employed a Maxwell-Boltzmann distribution for temperatures over the range $100-10000\,\mathrm{K}$, with 5000 trajectories being integrated for each batch using the VENUS96[40] code. Table 5 gathers the calculated rate constants for $\mathrm{H}+\mathrm{N}_2$ formation using DMBE II as obtained from:

$$k\left(T\right)=g_e\left(\frac{8k_BT}{\pi\mu_{\mathrm{N+NH}}}\right)^{1/2}\pi b_{max}^2\frac{N_r}{N} \tag{3}$$

where $g_e=1/6$ is the electronic degeneracy factor, μ the reduced mass of the colliding species and k_B the Boltzmann constant. Assuming 68% confidence, the associated error is $\Delta k\left(T\right)=k\left(T\right)\left[\left(N-N_r\right)/NN_r\right]^{1/2}$.

Figure 3 shows the calculated rate constant for N_2 formation as a function of temperature. For convenience, the results were fitted to a three-parameter Arrhenius form,

$$k\left(T\right)=AT^m\exp\left(-B/T\right) \tag{4}$$

leading to the optimum least-squares parameters $A=4.88\times10^{13}\,\mathrm{K^{-m}\,cm^3\,mol^{-1}s^{-1}}$, $m=-0.094$, and $B=-0.025\,\mathrm{K}$. The shape of the calculated curve shows a typical capture-type regime for low temperatures, which can be rationalized by the barrierless behavior of the N+NH interaction. Due to this, we may apply capture theory (Ref. 41, and references therein) to highlight the low-temperature trend of the QCT results.

Consider the spherically averaged long-range interaction for each ro-vibrational combination of $\mathrm{N}+\mathrm{NH}\left(v,j\right)$ to be described by

$$V_{lr}^{vj}\left(r\right)=-\langle C_n^{vj}\rangle r^{-n_{vj}} \tag{5}$$

where $\langle C_n^{vj}\rangle$ is the effective long-range coefficient of power n_{vj}, and r the atom-diatom separation. The parameters in Eq. (5) can then be approximated by a least-squares fit to the long-range spherically-averaged potential assuming the NH distance fixed at the quantum mechanical expectation value of the (v,j) state. The state-specific rate constant assumes the form[42]

$$k_{cap}^{vj}\left(T\right)=g_e\left(T\right)\frac{2^{(3n_{vj}-4)/2n_{vj}}n_{vj}\pi^{1/2}}{\left(n_{vj}-2\right)^{(n_{vj}-2)/n_{vj}}\mu^{1/2}}\Gamma\left(\frac{2n_{vj}-2}{n_{vj}}\right)\left(k_BT\right)^{(n_{vj}-4)/2n_{vj}}\langle C_n^{vj}\rangle^{2/n_{vj}} \tag{6}$$

Table 5. Summary of the QCT results for the $N + NH$ reaction.

		$N_2 + H$		$N + N + H$		$NH + N$	
T/K	b_{max}/Å	N_r	$10^{13}\,k_1/\mathrm{cm^3\,mol^{-1}\,s^{-1}}$	N_r	$10^{13}\,k_d/\mathrm{cm^3\,mol^{-1}\,s^{-1}}$	N_r	$10^{13}\,k_i/\mathrm{cm^3\,mol^{-1}\,s^{-1}}$
100	8.0	1816	3.96±0.07	–	–	–	–
300	6.9	1567	4.4±0.1	–	–	–	–
500	6.3	1527	4.6±0.1	–	–	–	–
1000	5.7	1434	5.0±0.1	–	–	–	–
2000	5.2	1304	5.4±0.1	–	–	–	–
3000	4.9	1276	5.7±0.1	–	–	10	0.04±0.01
4000	4.7	1280	6.1±0.2	–	–	26	0.12±0.02
5000	4.6	1271	6.5±0.2	8	0.04±0.01	56	0.29±0.04
6000	4.6	1214	6.8±0.2	24	0.13±0.03	75	0.42±0.05
7000	4.6	1183	7.1±0.2	73	0.44±0.05	99	0.60±0.06
10000	4.6	1024	7.4±0.2	209	1.5±0.1	166	1.20±0.09

with Γ being the Gamma function. The total rate coefficient can then be obtained by the usual averaging procedure leading to

$$k_{cap}\left(T\right)=Q_{\mathrm{vr}}^{-1}\left(T\right)\sum_{vj}^{\mathrm{NH}}\left(2j+1\right)k_{cap}^{vj}\left(T\right)\exp\left(-\frac{E_{vj}}{k_BT}\right) \tag{7}$$

where Q_{vr} is the reactants NH ro-vibrational partition function. Figure 3 compares the rate constant predicted by capture theory with our QCT results. Clearly, the reaction obeys a capture-type regime at low temperatures. Due to the high exothermicity, the recrossing value is expected to be small, especially for temperatures up to 300 K or so, and hence will be ignored. Note that for temperatures higher than 3000 K, the capture theory results are only given for qualitative analysis, as the method should no longer be reliable. Note further that for high translational and internal energies resulting from the sampling procedure, the diatomic molecule cannot re-orient to find the most favorable attacking geometry, and hence the rate constant becomes nearly temperature-independent. This behavior has been predicted by Miller *et al.*,[18] with $k\,(1100 \leq T/\mathrm{K} \leq 1400) = 3\times10^{13}\,\mathrm{cm^3\,s^{-1}\,mol^{-1}}$, being our value about 2.6 times larger. Note that other channels may open at high temperatures, namely, isomerization and total fragmentation; for completeness, these rate constants are also reported in Table 5. Note further that the $T^{0.5}$-dependence proposed by Westley[27] and used recently by Konnov and De Ruyck[20, 21] is not verified by the present results.

Also shown in Figure 3 is the experimental data of Hack *et al.*,[26] $k = 1.5\times10^{13}\,\mathrm{cm^3\,s^{-1}\,mol^{-1}}$, which has been obtained for room temperature. Their result is nearly 3 times lower than our QCT value and the capture-theory result. Even including a crude 20 % estimate of possible error,[26] the difference remains substantial. In turn, the agreement with the experimental estimate of Whyte and Phillips[28, 29] is satisfactory. Note, however, that the partition of the total rate of NH removal may not be equal for both electronic states as proposed by Zhan *et al.*[29] Thus, the observed discrepancies between the calculated and measured rate constants for the title system may be attributed both to experimental difficulties and to the non-inclusion of non-adiabatic effects in the theory as complicated electronic crossings[43, 44] are not taken into account by the single-sheeted DMBE II form. Of course, the use of classical mechanics cannot also be excluded

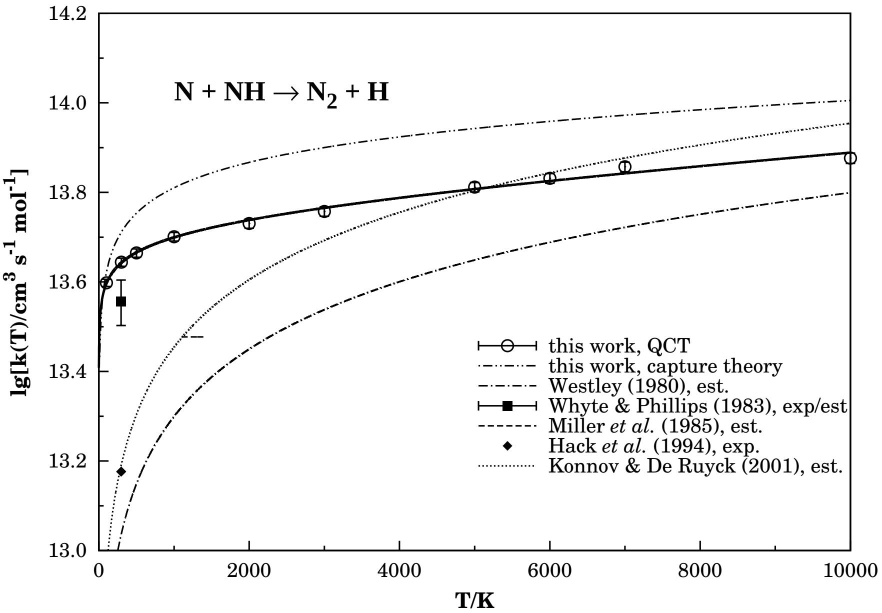

Figure 3. Rate coefficient for the N_2 + H formation as a function of temperature. The open symbols denote the QCT calculations using DMBE II, while the solid line indicates the Arrhenius fit. Also shown are the classical capture calculations. For comparison we plot estimates from various sources,[21, 27, 29, 35] and the experimental value of Hack *et al.*[26]

as a source of error. However, we emphasize the high quality of the *ab initio* data and DMBE II fit, and the fact that classical mechanical methods work extremely well for rate constant calculations even for the extreme case of three hydrogen atoms.[45] In summary, we can hardly assign the source of discrepancy between the experimental and theoretical results without going beyond the adiabatic picture and/or performing more accurate measurements.

For the $H + N_2$ endothermic reaction, we have used micro-reversibility as in previous work.[16] Thus, the $H + N_2$ formation rate constant assumes the form:

$$K(T) = \frac{k_1(T)}{k_{-1}(T)} \tag{8}$$

where k_1 and k_{-1} are the N_2 and NH formation rate constants, respectively. Using the Arrhenius parameters reported[16] for the equilibrium constant, $k_{-1}(T)$ can be expressed by the corresponding coefficients: $A = 1.40 \times 10^{15}\,\mathrm{K^{-m}\,cm^3\,mol^{-1}\,s^{-1}}$, $m = -0.10$, and $B = -74450\,\mathrm{K}$. To our knowledge, the only estimate available for comparison is from the GRI-Mech 3.0[46] which is based on statistical thermodynamical data for the equilibrium constant and the reported $k_1\,(T = 298\,\mathrm{K})$ value of Hack *et al.*[26] The agreement is seen to be fairly good, although the temperature dependence, also based on Eq. (8), has been obtained using a single value of the rate constant. We should note, that although rate constants for $\mathrm{NH} + \mathrm{N}$ formation are reported for temperatures down to room temperature, their estimates may suffer from considerable error below 2000 K. Quantitatively, we predict the $\mathrm{NH} + \mathrm{N}$ rate constant formation to be 4.35 (4.43) $\times\, 10^{-2}$, 7.27 (6.80) $\times\, 10^{1}$ and 10.2 (9.1) $\times\, 10^{3}\,\mathrm{cm}^3\,\mathrm{s}^{-1}\,\mathrm{mol}^{-1}$ for $T = 2000$, 2500 and 3000 K, respectively, being the values in brackets from GRI-Mech.[46]

4 The reaction $\mathbf{HN_2 \longrightarrow N_2 + H}$ and its reverse

The study of the radical lifetime and $\mathrm{HN_2} \rightarrow \mathrm{N_2} + \mathrm{H}$ dissociative process using the DMBE II potential energy surface has been carried out as in Ref. 16 using the complex method.[47, 48] Assuming an isolated resonance, the lifetime (τ_n) can be estimated by the associated width (Γ_n) according to the expression $\tau_n = \hbar/\Gamma_n$, while the unimolecular decay of the state is given by $k_n = \Gamma_n/\hbar$. The key elements for the unimolecular decay rate constant and lifetime calculation are the resonance width and the separation between resonances. Our results were obtained using the DVRD3D[49] code and Jacobi coordinates: r the $\mathrm{N_2}$ internuclear distance, R the atom-diatom separation and θ the orientation angle between the vectors $\boldsymbol{R}$ and $\boldsymbol{r}$. The primitive DVR basis employed $n_r = 40$, $n_R = 65$ and $n_\theta = 80$, with the parameters of the Morse-like functions being $r_e = 2.3\,\mathrm{a}_0$, $D_{e,r} = 0.8\,E_\mathrm{h}$ and $\omega_{e,r} = 0.02\,E_\mathrm{h}$ for the coordinate r, and $R_e = 4.3\,a_0$, $D_{e,R} = 0.8\,E_\mathrm{h}$ and $\omega_{e,R} = 0.01\,E_\mathrm{h}$ for R. The overall process utilized a truncation/diagonalization procedure, resulting in a 3000 dimensional secular problem. The lowest 1000 states have been retained for the complex calculations with the parameters of the negative imaginary potential being varied over the ranges $5.4 \leq R_{min}/a_0 \leq 5.8$ and $0.004 \leq \lambda/E_\mathrm{h} \leq 0.2$.

Table 6 gathers the energies and widths of the resonances calculated for the DMBE II potential energy surface, together with those previously reported[16] for DMBE I. Also shown for comparison are the results of Li and Guo[50] using double Chebyshev autocorrelation functions based on the KSW potential energy surface.

Table 6. Resonance parameters for the HN_2 radical.

	Li and Guo[a]		DMBE I[b]		DMBE II[c]	
state	E/cm^{-1}	Γ/cm^{-1}	E/cm^{-1}	Γ/cm^{-1}	E/cm^{-1}	Γ/cm^{-1}
(000)	4045.17	0.0019	4416.3	0.013	4409.1	0.010
(010)	5115.80	0.034	5500.7	0.16	5491.0	0.13
(001)	5766.90	2.09	6187.6	10.6	6172.9	9.1
(020)	6220.55	1.50	6573.0	9.6	6555.4	7.7
(100)	6386.4	55.8	6712	137	6702	134
(011)	6789.8	8.18	7242	35	7224	29
(030)	7289.4	13.5	7627	41	7609	34
(002)	7483.0	56.7	7962	39	7938	37
(021)	7879.6	34.6	8294	73	8273	73
(040)	8312.9	42.3	8655	127	8643	69
(012)	8559.2	79.6	9001	63	8981	60
(003)	9174.4	94.6	9695	96	9680	64

[a]Potential energy surface from Ref. 12. [b]Potential energy surface from Ref. 15. [c]This work.

For levels up to $7627\,\mathrm{cm}^{-1}$, the differences with DMBE I are less than $15\,\mathrm{cm}^{-1}$ which shows the similarities between the two surfaces in the region of the HN_2 minimum. We observe as before[16] that our calculated energies are systematically higher than the values reported by Li and Guo,[50] and that level splittings due to tunneling are negligible. Such differences can be attributed to small topographical differences between the two surfaces due to the distinct *ab initio* methods and electronic basis sets employed. Comparing the lifetime for the six leading states of HN_2 reported in Table 6, we conclude that all theoretical predictions are in reasonably good agreement with each other. As anticipated by the structural similarities between the different potential energy surfaces, the HN_2 lifetime is predicted to range from $10^{-9}\,$s to $10^{-13}\,$s, in contradiction with the postulated value of $10^{-4}\,$s suggested by kinetic modelers.

For completeness, we have calculated the unimolecular rate constant, $k\,(T)$

by assuming the high-pressure limit:

$$k\left(T\right)=\frac{1}{Q_{\mathrm{HN}_2}}\sum_k k_n \exp\left(-\frac{\Delta E_n}{k_B T}\right) \tag{9}$$

where Q_{HN_2} is the HN_2 partition function and $k_n = 1/\tau_n$. The results turn out to be almost indistinguishable from those reported elsewhere,[16] and hence will be omitted.

5 Concluding remarks

A novel (DMBE II) single-sheeted DMBE potential energy surface has been reported for the lowest doublet state of HN_2 by fitting accurate *ab initio* MRCI energies. As in previous work, such energies have first been corrected semiempirically to account for the basis set/configuration interaction finite sizes by using the DMBE-SEC method. The new fit shows a root-mean-squared deviation much smaller than DMBE I, which is possibly within the accuracy of the fitted *ab initio* points.

To test the DMBE II potential energy surface, a QCT study of the N + NH exothermic reaction has also been performed. Although being a simple atom-diatom elementary reaction studied on an accurate potential energy surface, a comparison with the experimental data reported in the literature shows at best fair agreement. Also the postulated temperature-dependence of $T^{0.5}$ used in previous theoretical models for this reaction could not be confirmed. To investigate the origin of the predicted temperature-dependence at low temperatures, calculations have been performed using classical capture theory and shown to be in good agreement with the QCT ones. Finally, the resonance states for the metastable HN_2 minima have been found to be in good agreement with those calculated using DMBE I. Further experimental and theoretical work is clearly necessary to clarify the pending issues.

Acknowledgments

This work has the financial support of the European Community (contract HPRN-CT-2002-00170) and Fundação para a Ciência e a Tecnologia, Portugal (contracts

POCI/QUI/60501/2004, POCI/AMB/60261/2004, and REEQ/128/QUI/2005).

References and Notes

[1] Hellman, A.; Baerends, E. J.; Biczysko, M.; Bligard, T.; Christensen, C. H.; Clary, D. C.; Dahl, S.; v.-Harrevelt, R.; Honkala, K.; Jonsson, H.; Kroes, G. J.; Luppi, M.; Manthe, U.; Norskov, J. K.; Olsen, R. A.; Rossmeisl, J.; Sklason, E.; Tautermann, C. S.; Varandas, A. J. C.; Vincent, J. K. *J. Phys. Chem. A* (in press).

[2] Miller, J. A.; Bowman, C. G. *Prog. Energy Combust. Sci.* **1989**, *15*, 287.

[3] Bozzelli, J. W.; Dean, A. M. *Int. J. Chem. Kinetics* **1995**, *27*, 1097.

[4] Hayhurst, A. N.; Hutchinson, E. M. *Combust. Flame* **1998**, *114*, 274.

[5] Hugues, K. J.; Tomlin, A. S.; Hampartsoumian, E.; Zsly, I. G.; Uj vri, M.; Turnyi, T.; Clague, A. R.; Pilling, M. J. *Combust. Flame* **2001**, *124*, 573.

[6] Tomeczek, J.; Gradoń, B. *Combust. Flame* **1998**, *133*, 311.

[7] Hwang, D.; Mebel, A. M. *J. Phys. Chem. A* **2003**, *107*, 2865.

[8] Dickinson, A. S.; Ern, A.; Vesovic, V. *Mol. Phys.* **2005**, *103*, 1895.

[9] Selgren, S. F.; McLaughlin, P. W.; Gellene, G. I. *J. Chem. Phys.* **1989**, *90*, 1624.

[10] Walch, S. P.; Duchovic, R. J.; Rohlfing, C. M. *J. Chem. Phys.* **1989**, *90*, 3230.

[11] Walch, S. P. *J. Chem. Phys.* **1990**, *93*, 2384.

[12] Koizumi, H.; Schatz, G. C.; Walch, S. P. *J. Chem. Phys.* **1991**, *95*, 4130.

[13] Walch, S. P.; Partridge, H. *Chem. Phys. Lett.* **1995**, *233*, 331.

[14] Gu, J.; Xie, Y.; Schaefer III, H. F. *J. Chem. Phys.* **1998**, *108*, 8029.

[15] Poveda, L. A.; Varandas, A. J. C. *J. Phys. Chem.* **2003**, *107*, 7923.

[16] Caridade, P. J. S. B.; Rodrigues, S. P. J.; Sousa, F.; Varandas, A. J. C. *J. Phys. Chem. A* **2005**, *109*, 2356.

[17] Miller, J. A.; Branch, M. C.; Kee, R. J. *Combust. Flame* **1981**, *81*, 43.

[18] Miller, J. A.; Glarborg, P. *Int. J. Chem. Kinetics* **1999**, *31*, 757.

[19] Dean, A. M. *Proceedings of the International Conference on the Foundations of Molecular Modeling and Simulation (FOMMS).* AIChE Symposium Series, vol. 97, 2001; p 84.

[20] Konnov, A. A.; De Ruyck, J. *Combust. Sci. Tech.* **2001**, *168*, 1.

[21] Konnov, A. A.; De Ruyck, J. *Combust. Flame* **2001**, *124*, 106.

[22] Werner, H.-J.; Knowles, P. J. *J. Chem. Phys.* **1988**, *89*, 5803.

[23] Dunning, T. H. *J. Chem. Phys.* **1989**, *90*, 1007.

[24] Kendall, R.; Dunning Jr., T.; Harrison, R. *J. Chem. Phys.* **1992**, *96*, 6769.

[25] Varandas, A. J. C. *J. Chem. Phys.* **1989**, *90*, 4379.

[26] Hack, W.; Wagner, H. G.; Zaspypkin, A. *Ber. Bunsenges. Phys. Chem.* **1994**, *98*, 156.

[27] Westley, F. *Table of recommended rate constants for chemical reactions occuring in combustion;* NBS: Washington, DC, NSRDS-NBS 67, 1980.

[28] Whyte, A. R.; Phillips, L. F. *Chem. Phys. Lett.* **1983**, *102*, 451.

[29] Zhang, J.; Huang, R.; Zhuang, Q.; Zhang, C. *Chem. Phys. Lett.* **1990**, *174*, 568.

[30] Varandas, A. J. C.; World Scientific Publishing, 2004; chapter 5, p 91; Advanced Series in Physical Chemistry.

[31] Martínez-Núñez, E.; Varandas, A. J. C. *J. Phys. Chem. A* **2001**, *105*, 5923.

[32] Kaskan, W. E.; Hughes, D. E. *Combust. Flame* **1973**, *20*, 381.

[33] Skreiberg, O.; Kilpinen, P.; Glarborg, P. *Combust. Flame* **2004**, *136*, 501.

[34] Catoire, L.; Luche, J.; Dupr, G.; Paillard, C. *Shock Waves* **2001**, *11*, 97.

[35] Miller, J. A.; Branch, M. C.; McLean, W. J.; Chandler, D. W.; Smooke, M. D.; Klee, R. J. *Proceedings of the Combustion Institute, vol. 20*, Pittsburgh; The Combustion Institute, 1985; p 673.

[36] Peslherbe, G. H.; Wang, H.; Hase, W. L. *Adv. Chem. Phys.* **1999**, *105*, 171.

[37] Rodrigues, S. P. J.; Varandas, A. J. C. *J. Phys. Chem. A* **2003**, *107*, 5369.

[38] R. J. Leroy, LEVEL 7.5, *A Computer Program For Solving The Radial Schrödinger Equation For Bound And Quasi-Bound Levels*, University Of Waterloo Chemical Physics Research Report CP-655 (2002).

[39] Varandas, A. J. C.; Silva, J. D. *J. Chem. Soc. Faraday Trans.* **1992**, *88*, 941.

[40] Hase, W. L.; Duchovic, R. J.; Hu, X.; Komornicki, A.; Lim, K. F.; Lu, D.; Peslherbe, G. H.; Swamy, K. N.; Linde, S. R. V.; Varandas, A. J. C.; Wang, H.; Wolf, R. J. *QCPE Bull.* **1996**, *16*, 43.

[41] Varandas, A. J. C. *Conferencias Plenarias de la XXIII Reunión Bienal de Química*; Feliciano, A. S., Grande, M., Casado, J., Eds.; Universidad de Salamanca: Salamanca, 1991; p 321.

[42] Varandas, A. J. C. *Faraday Discuss. Chem. Soc.* **1987**, *84*, 353.

[43] Walch, S. P. *J. Chem. Phys.* **1991**, *95*, 4277.

[44] Mota, V. C.; Varandas, A. J. C. (to be published).

[45] Zhao, M.; Truhlar, D. G.; Blais, N. C.; Schwenke, D. W.; Kouri, D. J. *J. Phys. Chem.* **1990**, *94*, 6696.

[46] Smith, G. P.; Golden, D. M.; Frenklach, M.; Moriarty, N. W.; Eiteneer, B.; Goldenberg, M.; Bowman, C. T.; Hanson, R. K.; Song, S.; Gardiner, Jr., W. C.; Lissianski, V. V.; Qin, Z., `http://www.me.berkeley.edu/gri_mech` (October, 2006).

[47] Jolicard, G.; Austin, E. J. *Chem. Phys.* **1986**, *103*, 295.

[48] Jolicard, G.; Leforestier, C.; Austin, E. J. *J. Chem. Phys.* **1988**, *95*, 1026.

[49] Tennyson, J.; Henderson, J. R.; Fulton, N. G. *Comput. Phys. Commun.* **1995**, *86*, 175.

[50] Li, G.; Guo, H. *Chem. Phys. Lett.* **2001**, *347*, 443.

Chapter 5

DMBE-PES for doublet and quartet states of NH_2

Theor. Chem. Acc. **116**, 404–419 (2006).

Accurate DMBE potential energy surface for the N $\left({}^2D\right)$+H$_2$ $\left({}^1\Sigma_g^+\right)$ reaction using an improved switching function formalism

A.J.C. Varandas and L.A. Poveda

Departamento de Química, Universidade de Coimbra
3004-535 Coimbra Codex, Portugal.

(Received: November 4, 2004; In final form: March 8, 2005)

Abstract

A single-sheeted double many-body expansion (DMBE) potential energy surface is reported for the $1\,{}^2A''$ state of NH$_2$. To approximate its true multi-sheeted nature, a novel switching function that imposes the correct behavior at the H$_2$ $\left(X^1\Sigma_g^+\right)$ + N $\left({}^2D\right)$ and NH $\left(X^3\Sigma^-\right)$ + H $\left({}^2S\right)$ dissociation limits has been suggested. The new DMBE form is shown to fit with high accuracy an extensive set of new *ab initio* points (calculated at the multi-reference configuration interaction level using the full valence complete active space as reference and aug-cc-pVQZ and aug-cc-pV5Z basis sets) that have been semiempirically corrected at the valence regions by scaling the n-body dynamical correlation terms such as to account for the finite basis set size and truncated configuration interaction expansion. A detailed study of the N $\left({}^2D\right)\cdots$H$_2$ $\left(X^1\Sigma_g^+\right)$ van der Waals region has also been carried out. These calculations predict a nearly free rigid-rotor with two shallow van der Waals wells of C_{2v} and $C_{\infty v}$ symmetries. Such a result contrasts with previous cc-pVTZ calculations which predict a single T-shaped van der Waals structure. Except in the vicinity of the crossing seam, which is replaced by an avoided intersection, the fit shows the correct physical behavior over the entire configurational space. The topographical features of the new DMBE potential energy surface are examined in detail and compared with those of other potential functions available in the literature. Amongst such features, we highlight the barrier for linearization ($11802\,\mathrm{cm}^{-1}$) which is found to overestimate the most recent empirical spectroscopic estimate by only $28\,\mathrm{cm}^{-1}$. Additionally, the T-shaped N $\left({}^2D\right)\cdots$H$_2$ van der Waals minimum is predicted to have a well depth of $90\,\mathrm{cm}^{-1}$, being $11\,\mathrm{cm}^{-1}$ deeper than the $C_{\infty v}$ minimum. The title DMBE form is therefore recommendable for dynamics studies of both non-reactive and reactive N $\left({}^2D\right)$ + H$_2$ collisions.

1 Introduction

The N $({}^4S, {}^2D, {}^2P) + H_2$ reaction has been the subject of considerable theoretical and experimental work due to the fundamental importance of nitrogen reactivity in atmospheric chemistry and combustion processes. Since the ground state nitrogen atoms, N $({}^4S)$, are often not very reactive, a major interest has been focused on reactions involving their lowest N $({}^2D)$ excited state.

During the past decade, the N $({}^2D) + H_2\left(X^1\Sigma_g^+\right) \rightarrow$ NH $(X^3\Sigma^-)$ + H $({}^2S)$ reaction has been studied using a LEPS (London-Eyring-Polanyi-Sato) potential energy surface proposed by Suzuki *et al.* [1], and a more realistic form obtained by fitting *ab initio* data to a Sorbie-Murrell type function [2]. Both theoretical studies concluded that the collinear (abstraction) path is dominant in the N $({}^2D) + H_2\left({}^1\Sigma_g^+\right)$ reaction, in agreement with a previous experimental result which provides evidence that it proceeds via a direct hydrogen atom abstraction mechanism [3]. However, more recent experimental results based on induced fluorescence [4, 5] and crossed molecular beam studies [6] suggest an insertion mechanism for the title reaction. Such a controversy has recently been clarified by using a global potential energy surface for the $1\,{}^2A''$ state of NH_2 reported by Ho *et al.* [7]. This surface, obtained by using the reproducing Kernel Hilbert Space (RKHS) interpolation method [8–10], represents an improved version of a previous RKHS surface [11] modeled from a fit to high quality *ab initio* data. Both these potential energy surfaces predict the N $({}^2D) + H_2\left({}^1\Sigma_g^+\right) \rightarrow$ NH $(X^3\Sigma^-)$ + H $({}^2S)$ reaction to proceed via a perpendicular approach of the nitrogen atom to H_2. In fact, quasiclassical trajectory (QCT) calculations based on such potential energy surfaces show excellent agreement with the more recent experimental measurements. There have been other *ab initio* potential energy surfaces for the title system. Of these, we mention the surfaces of Buenker *et al.* [12] and Gabriel *et al.* [13] for both the $\tilde{X}$ and $\tilde{A}$ states of the bent-bent Renner-Teller NH_2 system. In fact, additionally to the *ab initio* data, Gabriel *et al.* [13] carried out fits to their own data with a view to analyze the $\tilde{A}\,{}^2A_1 - \tilde{X}^2B_1$ spectrum, having achieved a high accuracy. They report a barrier height of $11914\,\mathrm{cm}^{-1}$ for the linearization of $NH_2(\tilde{X}\,{}^2B_1)$, although a more recent estimate [14] based on an empirically calibrated stretch-bender model points to a slightly lower value of $11774\,\mathrm{cm}^{-1}$.

In this work, we report a realistic global potential energy surface for $NH_2\,(1\,^2A'')$ based on DMBE [15–17] theory. Corresponding to a possible fragment of larger N_xH_y species such as those of relevance in studying the synthesis of ammonia, it may therefore play a key role in the construction of global DMBE forms for such polyatomic systems. Indeed, this has been a primary motivation for modeling an accurate single-sheeted DMBE potential energy surface for the title system.

To warrant that the potential energy surface dissociates to the correct asymptotes, we make use of an improved switching function approach [18]. In turn, the calibration employed 1498 *ab initio* points calculated at the multi-reference configuration interaction (MRCI) level using the full valence complete active space (FVCAS) as the reference function and the augmented polarized quadruple zeta (aug-cc-pVQZ or AVQZ) basis set of Dunning [19, 20]. To extrapolate the *ab initio* energies to the complete basis set/complete CI limit, they have been corrected semiempirically by using the double many-body expansion-scaled external correlation [21] (DMBE-SEC) method. As usual in DMBE [15–17] theory, the potential energy surface so obtained shows the correct long-range behavior at the dissociation channels while providing a realistic representation at all interatomic separations. For further realism, additional calculations of the long range $N\,(^2D) + H_2\,\left(^1\Sigma_g^+\right)$ interaction have been carried using a computationally more demanding aug-cc-pV5Z (AV5Z) basis set [19, 20], which were too corrected semiempirically by using the DMBE-SEC method.

The paper is organized as follows. Section 2 describes the *ab initio* calculations carried out in the present work, while section 3 focuses on their modeling using DMBE theory. Specifically, section 3.1 focuses on the two-body energy terms, and section 3.2 in the three-body ones. The major topographical features of the DMBE potential energy surface are examined in section 4. Section 5 gathers the concluding remarks.

2 *Ab initio* calculations

The *ab initio* calculations have been carried out at the MRCI [22] level using the FVCAS [23] wave function as reference. This involves seven correlated electrons in six active orbitals $(5a' + 1a'')$, amounting to a total of 50 configuration state functions. The AVQZ atomic basis set of Dunning [19, 20] has been employed, and the calculations carried out using the MOLPRO [24] package. To map the potential energy surface, a total of 1532 points have been calculated (34 estimated from nearby points through interpolation) over $\mathrm{N-H_2}$ regions defined by $1 \leq R_{\mathrm{H_2}}/a_0 \leq 3.5$, $1 \leq r_{\mathrm{N-H_2}}/a_0 \leq 11$, and $0° \leq \gamma \leq 90°$ while, for $\mathrm{H-NH}$, they cover geometries defined by $1.5 \leq R_{\mathrm{NH}}/a_0 \leq 3.5$, $1 \leq r_{\mathrm{H-NH}}/a_0 \leq 10$, and $0° \leq \gamma \leq 180°$; R, r, and γ are the atom-diatom Jacobi coordinates. For improved accuracy, 44 of the above *ab initio* points have been calculated using the AV5Z basis set [19, 20] for geometries encompassing the $\mathrm{N-H_2}$ van der Waals minimum: $R_{\mathrm{H_2}} = 1.2, 1.401, 1.6\, a_0$, $5.5 \leq r_{\mathrm{N-H_2}}/a_0 \leq 8.0$, and $\gamma = 4°, 8°, 15°, 30°, 45°, 60°, 75°$.

To account for electronic excitations beyond singles and doubles and, most importantly, for the incompleteness of the basis set, the calculated *ab initio* energies have been semiempirically corrected using the DMBE-SEC [25] method. Accordingly, the total DMBE-SEC interaction energy is written as

$$V(\mathbf{R}) = V_{\mathrm{FVCAS}}(\mathbf{R}) + V_{\mathrm{SEC}}(\mathbf{R}) \tag{1}$$

where

$$V_{\mathrm{FVCAS}}(\mathbf{R}) = \sum_{\mathrm{AB}} V^{(2)}_{\mathrm{AB,FVCAS}}(R_{\mathrm{AB}}) + V^{(3)}_{\mathrm{ABC,FVCAS}}(R_{\mathrm{AB}}, R_{\mathrm{BC}}, R_{\mathrm{AC}}) \tag{2}$$

$$V_{\mathrm{SEC}}(\mathbf{R}) = \sum_{\mathrm{AB}} V^{(2)}_{\mathrm{AB,SEC}}(R_{\mathrm{AB}}) + V^{(3)}_{\mathrm{ABC,SEC}}(R_{\mathrm{AB}}, R_{\mathrm{BC}}, R_{\mathrm{AC}}) \tag{3}$$

and $\mathbf{R} = \{R_{\mathrm{AB}}, R_{\mathrm{BC}}, R_{\mathrm{AC}}\}$ is a collective variable of all internuclear distances (these are equivalently denoted as $\{R_i\}$, with $i = 1-3$). Explicitly, the first two terms of the DMBE-SEC series expansion assume the form:

$$V^{(2)}_{\mathrm{AB,SEC}}(R_{\mathrm{AB}}) = \frac{V^{(2)}_{\mathrm{AB,FVCAS-CISD}}(R_{\mathrm{AB}}) - V^{(2)}_{\mathrm{AB,FVCAS}}(R_{\mathrm{AB}})}{F^{(2)}_{\mathrm{AB}}} \tag{4}$$

$$V^{(3)}_{\mathrm{ABC,SEC}}(\mathbf{R}) = \frac{V^{(3)}_{\mathrm{ABC,FVCAS-CISD}}(\mathbf{R}) - V^{(3)}_{\mathrm{ABC,SEC}}(\mathbf{R})}{F^{(3)}_{\mathrm{ABC}}} \tag{5}$$

Following previous work [25], the $F^{(2)}_{\mathrm{AB}}$ parameter in Eq. (4) has been chosen to reproduce the bond dissociation energy of the corresponding AB diatomic. Rather than choosing $F^{(3)}_{\mathrm{ABC}}$ to mimic the empirical well depth of $\mathrm{NH_2}(\tilde{X}\,^2B_1)$ which is somewhat uncertain ($124.5 \pm 0.2\,\mathrm{kcal\,mol^{-1}}$; the error bar has been taken from the reported heat of formation [26]), we have instead fixed $F^{(3)}_{\mathrm{ABC}}$ at the average of the three two-body F-factors. For the AVQZ basis set, such a procedure leads to $F^{(2)}_{\mathrm{HH}} = 0.9773$, $F^{(2)}_{\mathrm{NH}} = 0.9479$, and $F^{(3)}_{\mathrm{NHH}} = 0.9577$. In turn, for the AV5Z basis set, the scaling factors are $F^{(2)}_{\mathrm{HH}} = 0.9904$, $F^{(2)}_{\mathrm{NH}} = 0.9786$, and $F^{(3)}_{\mathrm{NHH}} = 0.9825$. Since our MRCI energies have been extrapolated to the complete basis set/configuration interaction limit, we judged unnecessary to correct the results for the basis set superposition error [27].

3 Single-sheeted potential energy surface

An approximate representation of a multi-sheeted potential energy surface by a single-sheeted form involves necessarily the use of switching functions. Such a procedure has first been proposed by Murrell and Carter [18], who applied it in the construction of an approximate potential energy surface for the ground-state of H_2O. In their paper, they have employed the switching function

$$f\,(\mathbf{R}) = \frac{1}{2}\{1 - \tanh\left[(3\rho_3 - \rho_1 - \rho_2)\,(\alpha/2)\right]\} \tag{6}$$

where $\rho_i = R_i - R_i^0$ are the displacements from a reference geometry (R_3 is the $\mathrm{H-H}$ distance, R_1 and R_2 the $\mathrm{O-H}$ ones), and α is a range-determining parameter. Such a function allows the $\mathrm{O}\,(^1D)$ state to appear in the $\mathrm{O}\,(^1D) + \mathrm{H_2}\left(^1\Sigma_g^+\right)$ channel (*i.e.*, for $\rho_1, \rho_2 \rightarrow \infty$) while being absent in the $\mathrm{OH}\,(^2\Pi) + \mathrm{H}\,(^2S)$ channel ($\rho_3 \rightarrow \infty$). A similar situation holds for the title system, where the following dissociation scheme applies:

$$\mathrm{NH_2}\left(1\,^2A''\right) \rightarrow \mathrm{H_2}\left(X^1\Sigma_g^+\right) + \mathrm{N}\left(^2D\right) \tag{7}$$

$$\rightarrow \mathrm{NH}\left(X^3\Sigma^-\right) + \mathrm{H}\left(^2S\right) \tag{8}$$

Since $\mathrm{NH}\,(^3\Sigma^-)$ dissociates to ground-state atoms, it is necessary to introduce a function that removes the $\mathrm{N}\,(^2D)$ state from this channel. However, as noted in Ref. 18, the function (6) cannot reach a unique value at the three-atom limit. Such an inconsistency prompted us to develop a more realistic switching function.

We suggest the form

$$h\left(R_1\right)=\frac{1}{4}\sum_{i=1}^{2}\{1-\tanh\left[\alpha_i\left(R_1-R_1^{i0}\right)+\beta_i\left(R_1-R_1^{i1}\right)^3\right]\} \tag{9}$$

where R_1 represents the $\mathrm{H-H}$ distance, and α_i and β_i $(i=1,2)$ are parameters to be calibrated from a least-squares fit to an extra set of 15 AVQZ points that control the $\mathrm{N}\left({}^2D\right)$ to $\mathrm{N}\left({}^4S\right)$ decay as the $\mathrm{H-H}$ distance increases for $\mathrm{N}+\mathrm{H}_2$ configurations (see the left-hand-side panel of Figure 1). As a check to the fit, we observe that at $R_1=1.401\,a_0$ the switching function differs by less than 10^{-6} from unit, thus warranting the correct energetics at the $\mathrm{N}\left({}^2D\right)+\mathrm{H}_2\left(X^1\Sigma_g^+\right)$ asymptote. To get a smooth three-body energy term, we further suggest to multiply Eq. (9) by an amplitude function that annihilates Eq. (9) at short-range regions (short $\mathrm{N-H}_2$ distances):

$$g\left(r_1\right)=\frac{1}{2}\{1+\tanh[\alpha\left(r_1-r_1^0\right)]\} \tag{10}$$

where r_1 is the distance of the N atom to the center of mass of H_2. A word is necessary at this point to clarify the notation. If the indexes (i,j,k) number the atoms (say, 1 for N, and 2 and 3 for H), r_i represents the Jacobi coordinate separating atom i from the center of mass of diatom jk whose bond distance is itself denoted by R_i. The final switching function assumes then the form

$$f\left(\mathbf{R}\right)=g\left(r_1\right)h\left(R_1\right) \tag{11}$$

with the parameters of $g\left(r_1\right)$ being chosen such as to warrant that its main effect occurs for $\mathrm{N-H}_2$ distances larger than $8\,a_0$ or so (see the right-hand-side panel of Figure 1). The numerical values of all parameters in Eq. (11) are collected in Table 1.

Within the framework of DMBE theory, the single-sheeted potential energy surface is written as

$$V\left(\mathbf{R}\right)=V^{(1)}_{\mathrm{N}(^2D)}f\left(\mathbf{R}\right)+\sum_{i=1}^{3}\left[V^{(2)}_{\mathrm{EHF}}\left(R_i\right)+V^{(2)}_{\mathrm{dc}}\left(R_i\right)\right]+\left[V^{(3)}_{\mathrm{EHF}}\left(\mathbf{R}\right)+V^{(3)}_{\mathrm{dc}}\left(\mathbf{R}\right)\right] \tag{12}$$

where $V_{\mathrm{N}}\left({}^2D\right)^{(1)}$ represents the difference in energy (at the scaled AVQZ level) between the ${}^2D$ and ${}^4S$ states of atomic nitrogen: $V_{\mathrm{N}}\left({}^2D\right)^{(1)}=0.09014\,E_{\mathrm{h}}$. For simplicity, we denote the resulting DMBE potential energy surface by $V\left(\mathbf{R}\right)$,

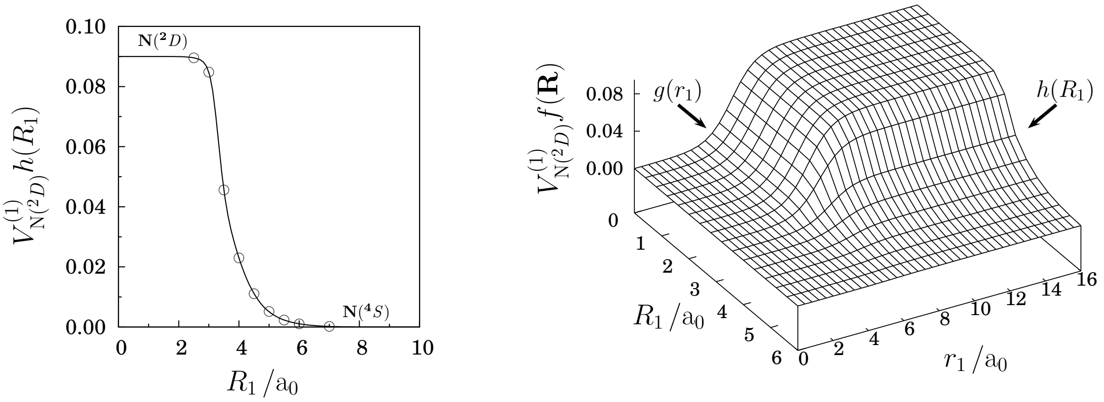

a) **b)**

Figure 1. Switching function used to model the single-sheeted NH_2 double many-body expansion (DMBE) potential energy surface. Shown in the *left panel* is the fit of the $h\,(R_1)$ switching form to the *ab initio* points calculated for $N + H_2$ configurations as a function of the H-H distance (R_1). Shown in the *right-hand side panel* is a perspective view of the global switching function in Eq. (11).

Table 1. Parameters in the switching function of Eq. (11).

Parameter	Numerical value
α_1	0.718244
α_2	0.719351
β_1	0.493967
β_2	0.066742
R_1^{10}	2.417270
R_1^{11}	4.355230
R_1^{20}	3.435560
R_1^{21}	5.520390
α	0.75
r_1^0	5.5

although this should not be confused with the scaled *ab initio* energies calculated in Eq. (1) which are used to calibrate Eq. (12). The following sections give the details of the analytical forms employed to represent the various energy terms in the latter.

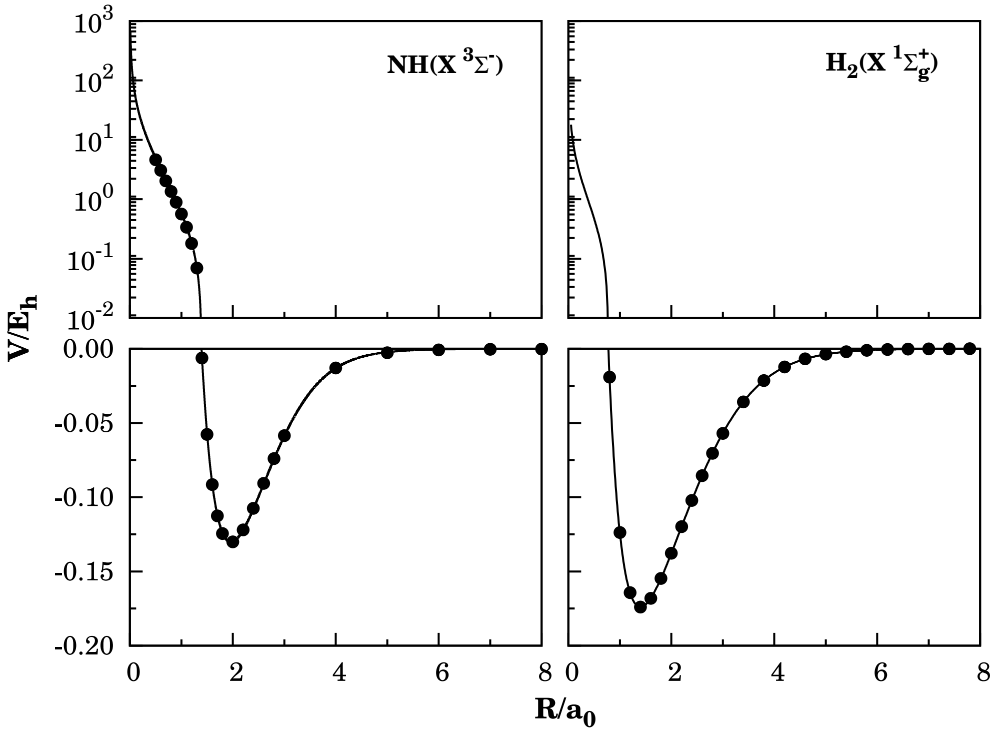

Figure 2. EHFACE2U potential energy curves for NH $(X^3\Sigma^-)$ and H$_2$ $\left(X^1\Sigma_g^+\right)$. The *solid dots* indicate the multi-reference configuration interaction (MRCI) points calculated in the present work.

3.1 Two-body energy terms

The potential energy curves for the two-body fragments are based on the extended Hartree-Fock approximate correlation energy method for diatomic molecules including the united atom limit [28] (EHFACE2U) which show the correct behavior at both the asymptotic limits $R \to 0$ and $R \to \infty$. They are given by the sum of two terms: (a) the extended-Hartree-Fock energy:

$$V_{\mathrm{EHF}}(R) = -\frac{D}{R}\left(1+\sum_{i=1}^{n} a_i r^i\right)\exp(-\gamma r) \tag{13}$$

where r (without any subscript) denotes the displacement coordinate relative to the equilibrium geometry of the diatomic, $r = R - R_e$; (b) the dynamical correlation energy:

$$V_{\mathrm{dc}}(R) = -\sum_{n=6,8,10} C_n \chi_n(R) R^{-n} \tag{14}$$

Table 2. Parameters of two-body potential energy curves in Eq. (13)-(16).

	NH $(X^3\Sigma^-)$	H$_2$ $\left(X^1\Sigma_g^+\right)$
R_e/a_0	1.9650	1.401
D/E_h	0.229 034 01	0.229 794 39
a_1/a_0^{-1}	2.146 641 73	1.820 274 80
a_2/a_0^{-2}	0.844 712 52	0.524 377 67
a_3/a_0^{-3}	0.525 908 29	0.369 996 10
γ_0/a_0^{-1}	1.563 792	1.094 670
γ_1/a_0^{-1}	0.661 116	1.009 737
γ_2/a_0^{-1}	0.282 985	0.235 856
$\widetilde{A}/E_\mathrm{h}a_0^{-\tilde{\alpha}}$		−0.8205
$\tilde{a}_1/a_0^{-1}$		0
$\tilde{\alpha}$		2.5
$\tilde{\gamma}/a_0^{-1}$		2.0
R_0/a_0	6.6570	6.9282
$C_6/E_\mathrm{h}a_0^{-6}$	12.27	6.499
$C_8/E_\mathrm{h}a_0^{-8}$	232.6	124.4
$C_{10}/E_\mathrm{h}a_0^{-10}$	5775	3286.0
$C_{11}/E_\mathrm{h}a_0^{-11}$		−3475
$C_{12}/E_\mathrm{h}a_0^{-12}$		121 500
$C_{13}/E_\mathrm{h}a_0^{-13}$		−291 400
$C_{14}/E_\mathrm{h}a_0^{-14}$		6 061 000
$C_{15}/E_\mathrm{h}a_0^{-15}$		−23 050 000
$C_{16}/E_\mathrm{h}a_0^{-16}$		393 800 000

where

$$\gamma = \gamma_0 \left[1 + \gamma_1 \tanh\left(\gamma_2 r\right)\right] \tag{15}$$

and

$$\chi_n\left(R\right) = \left[1 - \exp\left(-A_n \frac{R}{\rho} - B_n \frac{R^2}{\rho^2}\right)\right]^n \tag{16}$$

is a charge-overlap damping function for the long-range dispersion energy (as well as the electrostatic and induction energies, in case these must be considered). In turn, $A_n = \alpha_0 n^{-\alpha_1}$ and $B_n = \beta_0 \exp\left(-\beta_1 n\right)$ are auxiliary functions [15, 29]; $\alpha_0 = 16.36606$, $\alpha_1 = 0.70172$, $\beta_0 = 17.19338$, and $\beta_1 = 0.09574$. Moreover, $\rho = 5.5 + 1.25R_0$ is a scaling parameter, $R_0 = 2\left(\langle r_\mathrm{A}^2\rangle^{\frac{1}{2}} + \langle r_\mathrm{B}^2\rangle^{\frac{1}{2}}\right)$ is the LeRoy [30] parameter for the onset of the undamped R^{-n} expansion, and $\langle r_{\mathrm{X}}^2 \rangle$ is the expectation value of the squared radius for the outermost electrons of atom X (X $= A, B$). Finally, D and $a_i\,(i = 1, \ldots, n)$ in Eq. (13) are adjustable parameters to be obtained as described elsewhere [15, 28]. Here, we employ the accurate EHFACE2U potential energy curve of ground-state $\mathrm{H}_2\left(X^1\Sigma_g^+\right)$ reported in Ref. 31, and the curve of ground-state imidogen, $\mathrm{NH}\,(X^3\Sigma^-)$, modeled [32] from MRCI+Q *ab initio* points [33]. As shown in Figure 2, both potential curves mimic accurately the *ab initio* energies calculated in the present work, being for completeness numerically defined in Table 2.

3.2 Three-body energy terms

3.2.1 Three-body dynamical correlation energy

This three-body energy term assumes the following semiempirical form [31]:

$$V_{\mathrm{dc}}^{(3)} = -\sum_i \sum_n f_i\,(\mathbf{R})\, C_n^{(i)}\,(R_i, \theta_i)\, \chi_n\,(r_i)\, r_i^{-n} \tag{17}$$

where r_i, θ_i amd R_i are the Jacobi coordinates corresponding to a specific geometry of the triatomic (see Figure 1 of Ref. 25), and $f_i = \frac{1}{2}\left\{1 - \tanh\left[\xi\left(\eta R_i - R_j - R_k\right)\right]\right\}$ is a convenient switching function; corresponding expressions apply to R_j, R_k, f_j, and f_k. Following recent work on HCN [34], we have fixed $\eta = 6$ and $\xi = 1.0\,a_0^{-1}$. Regarding, the damping function $\chi_n\,(r_i)$, we still adopt [31] Eq. (16) but replace R by the center-of-mass separation for the relevant atom-diatom channel. In addition, the value of ρ has been optimized by a trial and error procedure to mimic the asymptotic long-range behavior of the dynamical correlation energy, leading to $\rho = 16.125\,a_0$.

The atom-diatom dispersion coefficients in Eq. (17) assume their usual form

$$C_n^{(i)}\,(R_i) = \sum_L C_n^L\,(R)\, P_L\,(\cos\theta_i) \tag{18}$$

where $P_L\,(\cos\theta_i)$ denotes the L-th Legendre polynomial. The expansion in Eq. (18) has been truncated by considering only the coefficients C_6^0, C_6^2, C_8^0, C_8^2, C_8^4, and C_{10}^0; all other coefficients have been assumed to make a negligible contribution, and hence neglected. To estimate the dispersion coefficients we have utilized the

Table 3. Numerical values of the parameters in Eq. (19).

	$C_6^0\,(R)$	$C_6^2\,(R)$	$C_8^0\,(R)$	$C_8^2\,(R)$	$C_8^4\,(R)$	$C_{10}^0\,(R)$
			$N-H_2$			
R_M/a_0	3.4158	3.2065	3.1636	3.0873	3.0865	2.9727
D_M/E_h	5.9304	3.7795	270.9628	368.8294	28.4794	12092.994
a_1/a_0^{-1}	1.206 805 20	0.488 983 03	0.665 912 20	0.760 284 18	0.834 397 44	0.484 011 10
a_2/a_0^{-2}	0.377 739 24	0.019 482 20	0.119 813 57	0.167 131 92	0.213 721 45	0.108 384 66
a_3/a_0^{-3}	0.047 339 74	−0.010 289 89	0.050 137 67	0.007 868 82	0.014 822 01	0.068 509 18
b_2/a_0^{-2}	0.208 288 95	0.238 894 66	0.234 668 06	0.246 662 19	0.505 971 19	0.254 421 28
b_3/a_0^{-3}	2.7×10^{-9}	2.4×10^{-9}	5.4×10^{-10}	1.2×10^{-8}	6.9×10^{-9}	7.9×10^{-9}
			$H-NH$			
R_M/a_0	3.4400	3.2341	3.5037	3.2923	3.2491	3.5428
D_M/E_h	3.3090	3.0188	57.5906	183.9318	14.6299	1311.7401
a_1/a_0^{-1}	1.633 054 47	0.574 693 34	1.805 549 07	1.068 206 52	1.234 965 92	0.839 070 20
a_2/a_0^{-2}	0.752 234 77	0.030 861 75	0.799 316 30	0.325 331 77	0.342 108 54	−1.100 099 19
a_3/a_0^{-3}	0.118 455 16	0.042 745 67	0.132 854 42	0.029 613 79	−0.023 019 09	−0.248 070 00
b_2/a_0^{-2}	0.334 438 28	0.404 972 90	0.598 195 06	0.347 250 53	0.757 397 97	0.596 107 95
b_3/a_0^{-3}	2.2×10^{-9}	6.7×10^{-9}	0.052 923 95	1.3×10^{-8}	5.7×10^{-9}	0.105 297 09

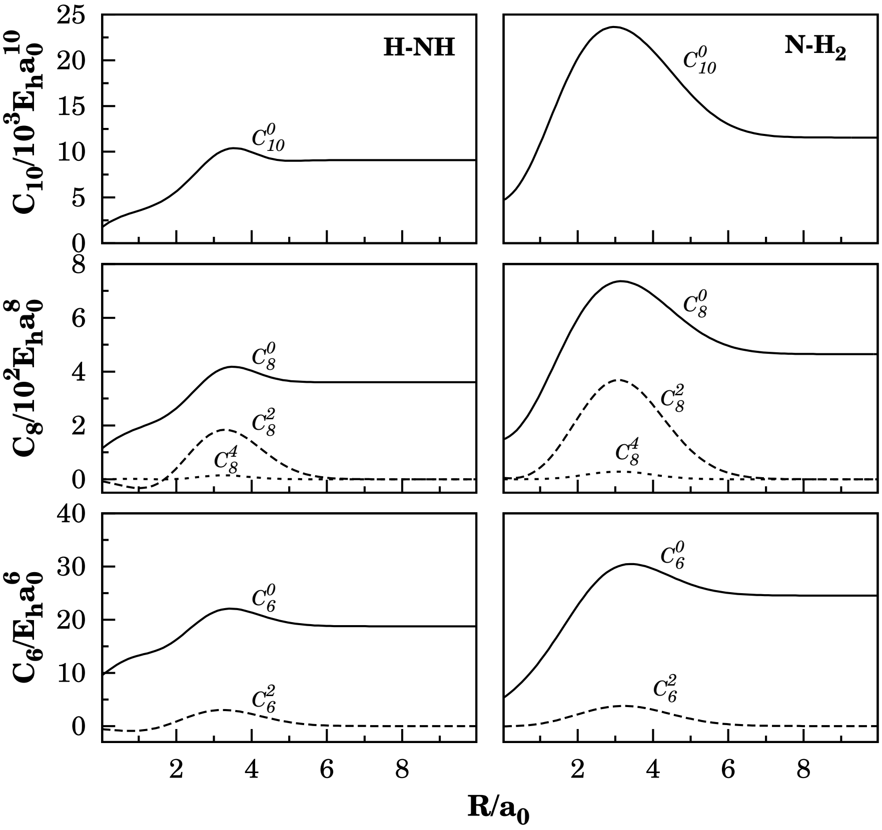

Figure 3. Dispersion coefficients for the atom-diatom asymptotic channels of NH_2 as a function of the corresponding diatomic internuclear distance.

generalized Slater-Kirkwood approximation [35] and dipolar polarizabilities calculated in the present work at the MRCI/AVQZ level. As usual, the atom-diatom dispersion coefficients so calculated for a set of internuclear distances have then been fitted to the form

$$C_n^{L,\mathrm{A-BC}}(R) = C_n^{L,\mathrm{AB}} + C_n^{L,\mathrm{AC}} + D_\mathrm{M}\left(1+\sum_{i=1}^{3} a_i r^i\right)\exp\left(-\sum_{i=1}^{3} b_i r^i\right) \tag{19}$$

where $C_n^{L,\mathrm{AB}}$, for $L=0$, are the corresponding atom-atom dispersion coefficients (see Table 2; for $L \neq 0$, $C_n^{L,\mathrm{AB}} = 0$), and $b_1 = a_1$. The least squares parameters that result from such fits are collected in Table 3, while their internuclear dependencies are displayed in Figure 3. Note that, for $R=0$, the isotropic component of the dispersion coefficient is fixed at the corresponding value in the $\mathrm{A-X}$ pair, where X represents the united atom of BC at the limit of a vanishingly small internuclear separation.

As noted elsewhere [31], Eq. (17) causes an overestimation of the dynamical correlation energy at the atom-diatom dissociation channels. To correct such a behavior, we have multiplied the two-body dynamical correlation energy for the i-th pair by $\prod_{j\neq i}(1-f_j)$ (correspondingly for channels j and k). This ensures [31, 34] that the only two-body contribution at the i-th channel is that of JK.

3.2.2 Three-body extended Hartree-Fock energy

By removing, for a given triatomic geometry, the sum of the one-body and two-body energy terms from the corresponding DMBE-SEC interaction energies in Eq. (1) which were defined with respect to the infinitely separated ground-state atoms, one obtains the total three-body energy. By then subtracting from this the three-body dynamical correlation contribution of Eq. (17), one gets the three-body extended Hartree-Fock energy. This has been modeled via a three-body distributed-polynomial [36] form

$$V_{\mathrm{EHF}}^{(3)} = \sum_{j=1}^{5} P^{(j)}\left(Q_1, Q_2, Q_3\right) \prod_{i=1}^{3} \{1 - \tanh[\gamma_i^j \left(R_i - R_i^{j,ref}\right)]\} \tag{20}$$

where all the polynomials $P^{(j)}(Q_1, Q_2, Q_3)$ are written in terms of symmetry coordinates (for definition of the latter, see, e.g., Ref. 36). Note that all polynomials are of sixth order, except the fifth one which is of fourth order. Figure 4 displays the reference geometries that have been used to define the displacement coordinates involved in Eq. (20). To obtain $R_i^{(j),ref}$, we have first assumed their values to coincide with the bond distances of the associated stationary points. Such a restriction has subsequently been relaxed, with the optimum geometry being obtained via a trial-and-error procedure such as to reduce the root-mean-square-deviation (rmsd) of the final least squares fit. A similar procedure has been employed to set the nonlinear range-determining parameters $\gamma_i^{(j)}$. The complete set amounts to a total of 222 linear coefficients c_i, 15 nonlinear ones $\gamma_i^{(j)}$, and 15 reference geometries $R_i^{(j),ref}$. A total of 1532 points (including those referring to the $\mathrm{N}-\mathrm{H}_2\left({}^1\Sigma_g^+\right)$ van der Waals regions, and some interpolated ones) covering an energy range of over $2400\,\mathrm{kcal\,mol^{-1}}$ above the $\mathrm{NH_2}$ global minimum has been used. Note that special weights have been attributed during the cali-

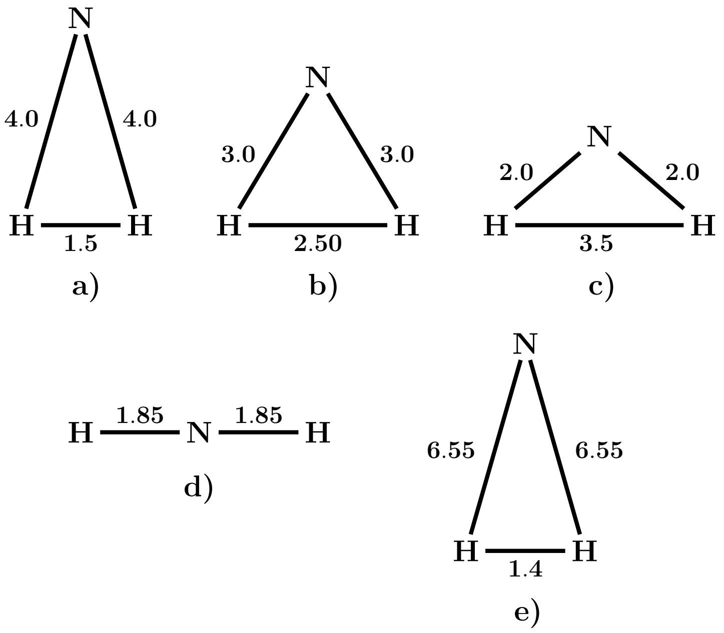

Figure 4. Reference geometries used to define the three-body EHF part of the potential energy surface (distances in atomic units).

Table 4. Numerical values of the extended Hartree-Fock energy [Eq. (20)].

Coefficients	$P^{(1)}$	$P^{(2)}$	$P^{(3)}$	$P^{(4)}$	$P^{(5)}$
c_1/a_0^0	0.28972574	−2.23883819	−4.82026636	−10.34547901	0.00336417
c_2/a_0^{-1}	−0.55810849	1.34798852	−13.32989155	6.82146451	0.00402458
c_3/a_0^{-1}	0.35597867	2.51479201	5.20391403	−16.51164712	0.00771292
c_4/a_0^{-2}	0.03011379	0.04660040	−6.98310018	4.19257033	0.01268136
c_5/a_0^{-2}	0.25264641	0.32033747	−1.76174899	−3.15318437	0.01274666
c_6/a_0^{-2}	0.07150504	0.07961873	13.14913342	−16.43761499	0.03631929
c_7/a_0^{-2}	−0.00252553	−0.21360102	2.40680438	−3.61361568	−0.01501876
c_8/a_0^{-3}	−0.21020530	0.33599947	−2.51660228	2.56964682	0.00517592
c_9/a_0^{-3}	−0.01034405	−0.02985039	−2.18746772	−3.09554468	0.02417986
c_{10}/a_0^{-3}	−0.00563727	−0.15730581	−0.58279739	1.17297483	0.00682636
c_{11}/a_0^{-3}	−0.40826443	0.23927521	3.14929292	−1.27957617	0.02804054
c_{12}/a_0^{-3}	0.00437155	0.33805178	−1.50882772	4.26944653	−0.02483353
c_{13}/a_0^{-3}	0.24320295	0.52130976	−0.82580774	−0.49508061	0.02143404
c_{14}/a_0^{-4}	0.00581370	0.10163321	−0.71370355	0.89781794	−0.00164759
c_{15}/a_0^{-4}	0.05288872	0.14376423	−2.89543978	1.03355863	−0.00195096
c_{16}/a_0^{-4}	0.07532079	0.01518369	−0.16687247	0.32623867	0.00319575
c_{17}/a_0^{-4}	−0.03234647	0.02334543	0.17918664	−1.06417943	0.00349031

Table 4. Continue

c_{18}/a_0^{-4}	−0.01099316	−0.21441955	3.47245330	−2.63944411	−0.00604896
c_{19}/a_0^{-4}	0.03642900	0.03273485	1.73645519	−1.18691152	0.00062813
c_{20}/a_0^{-4}	0.15570612	−0.05901273	2.18616814	−4.71082073	0.00668133
c_{21}/a_0^{-4}	−0.03994482	−0.02320849	−0.18076633	1.00046730	0.00318550
c_{22}/a_0^{-4}	−0.05956185	0.07340589	0.14178975	−0.67036214	−0.00255943
c_{23}/a_0^{-5}	−0.00621797	−0.00084108	−0.06377893	0.14299508	–
c_{24}/a_0^{-5}	−0.02764205	−0.05366966	0.53031223	−0.99916190	–
c_{25}/a_0^{-5}	0.01514678	−0.02402850	0.43331974	−0.82278451	–
c_{26}/a_0^{-5}	−0.02854379	−0.01843950	−0.36266437	0.22691603	–
c_{27}/a_0^{-5}	−0.01063750	−0.00336688	−0.16888422	0.40056270	–
c_{28}/a_0^{-5}	−0.02862361	0.02767599	−0.27565869	0.75973486	–
c_{29}/a_0^{-5}	0.02458300	−0.00764734	−0.33960193	0.95557878	–
c_{30}/a_0^{-5}	−0.02140507	0.08481649	−0.99355561	1.23475350	–
c_{31}/a_0^{-5}	−0.05777760	−0.01127916	0.37535466	−0.18269793	–
c_{32}/a_0^{-5}	−0.01665148	0.05385674	−0.57480428	0.97068822	–
c_{33}/a_0^{-5}	0.02122847	0.01730448	−0.33531560	0.49320770	–
c_{34}/a_0^{-5}	0.01914194	−0.01763677	0.06028977	−0.22657901	–
c_{35}/a_0^{-6}	0.00247218	0.00528895	−0.02671849	0.01997170	–
c_{36}/a_0^{-6}	−0.01211048	0.00385499	−0.14913457	0.03988751	–
c_{37}/a_0^{-6}	−0.00711497	−0.00795683	−0.18350113	0.19528166	–
c_{38}/a_0^{-6}	−0.01872577	−0.00071293	0.16239653	−0.07885454	–
c_{39}/a_0^{-6}	−0.01205357	−0.00401599	0.12562857	−0.09168383	–
c_{40}/a_0^{-6}	0.00413216	−0.00077721	−0.02558218	0.02345618	–
c_{41}/a_0^{-6}	−0.00414042	−0.00042295	−0.01396550	0.02710977	–
c_{42}/a_0^{-6}	0.00126063	−0.01642519	0.17919501	−0.03676125	–
c_{43}/a_0^{-6}	0.01332372	−0.00906645	0.21487615	−0.00597842	–
c_{44}/a_0^{-6}	−0.03787771	0.00117807	0.31174108	−0.28878921	–
c_{45}/a_0^{-6}	−0.02600113	0.00820752	−0.19069192	0.07088748	–
c_{46}/a_0^{-6}	0.01181454	0.00821036	0.15454689	−0.24948561	–
c_{47}/a_0^{-6}	0.00951985	0.01190600	0.15238190	−0.23974016	–
c_{48}/a_0^{-6}	0.01278203	0.00159730	−0.06594640	0.01599530	–
c_{49}/a_0^{-6}	−0.00486393	0.00644670	−0.08568753	0.10016699	–
c_{50}/a_0^{-6}	−0.00142419	−0.00027149	0.01609771	−0.02005957	–
$\gamma_1^{(j)}/a_0^{-1}$	1.45	0.40	0.35	0.75	3.95
$\gamma_2^{(j)}/a_0^{-1}$	0.50	0.80	0.85	0.75	0.65
$\gamma_3^{(j)}/a_0^{-1}$	0.50	0.80	0.85	0.75	0.65
$R_1^{(j),ref}/a_0$	1.50	2.50	3.50	3.70	1.40
$R_2^{(j),ref}/a_0$	4.00	3.00	2.00	1.85	6.55
$R_3^{(j),ref}/a_0$	4.00	3.00	2.00	1.85	6.55

Table 5. Stratified maximum and root-mean-square deviations (in $\mathrm{kcal\,mol^{-1}}$) of double many-body expansion (DMBE) potential energy surface.

Energy	N^a	max. dev.^{b}	rmsd	$N^c_{>\mathrm{rmsd}}$
10	127	0.187	0.031	13
20	141	0.205	0.045	17
30	159	2.160	0.189	8
40	184	2.160	0.251	15
50	197	2.160	0.255	20
60	218	2.160	0.283	30
70	236	2.160	0.289	37
80	259	2.160	0.296	45
90	292	2.160	0.311	55
100	404	2.160	0.286	71
120	600	2.515	0.341	88
140	922	2.855	0.359	143
160	1197	2.855	0.378	193
180	1372	3.304	0.409	222
200	1421	3.806	0.428	224
250	1442	3.806	0.442	227
500	1475	3.806	0.457	238
1000	1493	3.806	0.474	237
2000	1497	3.806	0.474	239
2400	1498	3.806	0.474	240

[a] Number of calculated multi-reference configuration interaction/aug-cc-pVQZ (MRCI/AVQZ) and aug-cc-pV5Z (AV5Z) points up to the indicated energy range. [b] Maximum deviation up to the indicated energy range. [c] Number of calculated MRCI/AVQZ and AV5Z points with an energy deviation larger than the rmsd.

bration procedure to the points close to stationary points; the complete list of *ab initio* energies and least-squares weights actually employed for the final fit may be obtained from the authors upon request. Table 4 gathers the values of the least-squares parameters.

The stratified rmsd of the final potential energy surface with respect to all fitted *ab initio* energies are reported in Table 5. As shown, the final potential energy surface fits the regions up to the linear and C_{2v} barriers ($\sim$130 kcal mol^{-1} above the global minimum) with a rmsd of < 0.4 kcal mol^{-1} and a maximum deviation of < 2.8 kcal mol^{-1}. Not surprisingly, the major (yet small) deviations occur at highly repulsive regions of the potential energy surface. Despite this, the DMBE form is seen to fit the *ab initio* data with chemical accuracy, with a stratified rmsd $\ll 1\,\%$ of the energy for the given stratum. Note that only a small percent of the points ($< 16\,\%$, this being for the whole range of energies) have a deviation larger than the calculated rmsd. Thus, although the fit might be improved by adding other polynomials, no attempt was deemed to be justified due to the unavoidable errors at regions close to the crossing seam.

4 Features of the potential energy surface

Table 6 compares the attributes of the stationary points of the DMBE potential energy surface with those of other theoretical potentials for ground state NH_2, especially the most recent work of Ho *et al.* [7] (see also this reference for further comparisons). As expected, the DMBE surface predicts a lower barrier for the perpendicular insertion of the nitrogen atom into H_2. The predicted geometry and well depth of the global minimum are seen to be basically coincident with those reported by Ho *et al.* [7] who have based their function on MRCI calculations using an AVTZ basis set (heretofore denoted by MRCI/AVTZ, and correspondingly for other basis sets). Note that the scaling of the dynamical correlation leads to a MRCI/AVQZ well depth for $NH_2(\tilde{X}\,^2B_1)$ of 126.4 kcal mol^{-1} which is identical to the one obtained from the MRCI/AVTZ calculations after correcting for the triple and quadruple excitations using the Davidson correction [11] (except where mentioned otherwise, we will keep the notation MRCI/AVTZ to denote the corrected calculations at this level). Note further that the uncorrected MRCI/AVTZ calculations [11] lead to a well depth of 125.5 kcal mol^{-1}, which compares with the value of 125.9 kcal mol^{-1} obtained in the present work at the corresponding MRCI/AVQZ level. Thus, for the AVTZ calculations, the Davidson correction leads to a further increase of 0.4 kcal mol^{-1} in the well depth of $NH_2(\tilde{X}\,^2B_1)$ when compared with the MRCI/AVQZ results from the present work after correction by the DMBE-SEC method. Table 6 also shows that the harmonic frequencies

Table 6. Stationary points at the valence region of $NH_2\,(1\,^2A'')$ potential energy surface.

Feature	property	*ab initio*[a]	*ab initio*[b]	RKHS[b,c]	DMBE-SEC[d]	DMBE[c,d]
Global minimun	R_1/a_0		3.04	3.04	3.0288	3.0291
	R_2/a_0		1.9445	1.94	1.9406	1.9405
	$r_1^{e)}/a_0$		1.21	1.20	1.2135	1.2131
	$\angle\mathrm{HNH}^f$		102.7°	102.7°	102.6°	102.6°
	V/E_h				-0.2858	-0.2858
	ΔV^g		-126.4	-126.4	-126.4	-126.4
	$\omega_1\,(\mathrm{N-H})_{sym}\,/\mathrm{cm}^{-1}$		3340	3350	3377	3383
	$\omega_2\,(\mathrm{N-H})_{asym}\,/\mathrm{cm}^{-1}$		3435	3436	3443	3457
	$\omega_3\,(\mathrm{bend})\,/\mathrm{cm}^{-1}$		1542	1559	1523	1541
C_{2v} barrier $\mathrm{N}\,(^2D)-\mathrm{H}_2$	R_1/a_0	1.42	1.42	1.42	1.4203	1.4198
	R_2/a_0	3.96	4.05	4.05	3.9561	3.9349
	r_1/a_0	3.90	3.99	3.99	3.8918	3.8703
	$\angle\mathrm{HNH}$	20.7°	20.2°	20.2°	20.7°	20.8°
	V/E_h				-0.0809	-0.0809
	$\Delta V^{g)}$	2.31	1.8	1.8	2.16	2.16
	$\omega_1\,(\mathrm{H-H})\,/\mathrm{cm}^{-1}$		4239	4240	4223	4209
	$\omega_2\,(\mathrm{N\cdots H_2})\,/\mathrm{cm}^{-1}$		$501i$	$499i$	$547i$	$499i$
	$\omega_3\,(\mathrm{H_2\,rot.})\,/\mathrm{cm}^{-1}$		324	325	385	282
$C_{\infty v}$ barrier $\mathrm{N-H-H}$	R_1/a_0	1.52	1.539	1.54		1.5121
	R_2/a_0	2.94	2.913	2.93		2.9010
	r_1/a_0	3.70	3.68	3.70		3.6570
	V/E_h					-0.0763
	ΔV^g	4.61	4.8	4.8		5.1
	$\omega_1\,(\mathrm{H-H})\,/\mathrm{cm}^{-1}$		3031	2616		2671
	$\omega_2\,(\mathrm{N-H})\,/\mathrm{cm}^{-1}$		$1031i$	$1032i$		$1455i$
	$\omega_3\,(\mathrm{bend})\,/\mathrm{cm}^{-1}$		$818i$	$764i$		$844i$

[a] Ref. 37. [b] Ref. 7. [c] Fit. [d] This work. [e] The experimental value reported in Ref. 11 is $1.21\,a_0$. [f] The experimental value reported in Ref. 11 is 103.0°. [g] Relative to the $\mathrm{N}\left(^2D\right)+\mathrm{H}_2$ asymptote (in $\mathrm{kcal\,mol^{-1}}$). At this limit, the FVCAS and MRCI/aug-cc-pVQZ energies are $-55.45066862\,E_\mathrm{h}$ and $-55.60375691\,E_\mathrm{h}$, respectively.

are very similar for the MRCI/AVTZ and DMBE-SEC surfaces, with the differences being smaller than about $50\,\mathrm{cm}^{-1}$. The same observation extends to the DMBE surface. We emphasize that a dense grid of points has been calculated in the vicinity of the global minimum, with the rmsd of the DMBE least-squares fit to such points being of $\sim 0.3\,\mathrm{cm}^{-1}$ ($\sim 0.08\,\mathrm{cm}^{-1}$ for the direct fit of a cubic polynomial in valence coordinates to the DMBE-SEC data).

For the C_{2v} barrier, the DMBE potential energy surface predicts a barrier height which is 0.36 kcal mol^{-1} higher than that predicted by the Ho *et al.* [7] form (0.23 kcal mol^{-1} higher than their previous *ab initio* estimate [11]) but 0.15 kcal mol^{-1} below the MRCI calculations reported by Takayanagi *et al.* [37] using a somewhat less flexible cc-pVTZ basis set. Note that those potential energy surfaces [7, 11, 37] employ *ab initio* diatomic curves calculated at the corresponding level of *ab initio* theory, whereas in our case they have been corrected by scaling the dynamical correlation such that the full curve mimics the best available estimate for the well depth (see section 2). Recall now that the three-body scaling factor used in the DMBE-SEC method is obtained as the average of the two-body ones. Thus, the attributes of the triatomic potential are true predictions of the method. For example, the calculated bond length and dissociation energy for H_2 (including the one-body term referring to the energy difference between the ^4S and ^2D electronic states of atomic nitrogen) at the MRCI/AVTZ level are $R_e = 1.404\,a_0$ and $D_e = -0.082762\,E_\mathrm{h}$ while the corresponding attributes of the EHFACE2U (or SEC) curve are $R_e = 1.401\,a_0$ and $D_e = -0.084336\,E_\mathrm{h}$. As shown in Figure 5, the H_2 asymptote in the DMBE potential energy surface lies therefore 0.987 kcal mol^{-1} below the MRCI/AVTZ curve obtained by interpolation using the RKHS method [7]. Similarly, a fit to the dense grid of unscaled MRCI/AVQZ points close to the C_{2v} saddle point calculated in the present work leads to a barrier height relative to the unscaled MRCI/AVQZ curve for H_2 of 2.19 kcal mol^{-1}, *i.e.*, the scaling of the dynamical correlation is predicted to yield a stabilization of only 0.03 kcal mol^{-1} relatively to the unscaled calculations. Assuming that the Davidson correction would lead to an extra lowering similar to the value encountered for the equilibrium geometry, one would predict a barrier height for the C_{2v} insertion of N (^2D) into H_2 of $2.19-0.4-0.03=1.76$ kcal mol^{-1}, in surprisingly good agreement with the value of 1.8 kcal mol^{-1} reported for the MRCI/AVTZ calculations [7, 11]. Instead, if we use their estimated [7, 11] AVTZ Davidson correction (0.36 kcal mol^{-1}) at the C_{2v} saddle point one gets $2.19 - 0.39 = 1.8$ kcal mol^{-1}, which yields an AVQZ barrier height identical to the AVTZ one. This by no means implies that the inclusion of the Davidson correction leads to a more reliable barrier height than the DMBE-SEC method. In fact, this method has by construction the advantage of mimicking the exact atom+diatomic asymptote at the equilibrium geometry

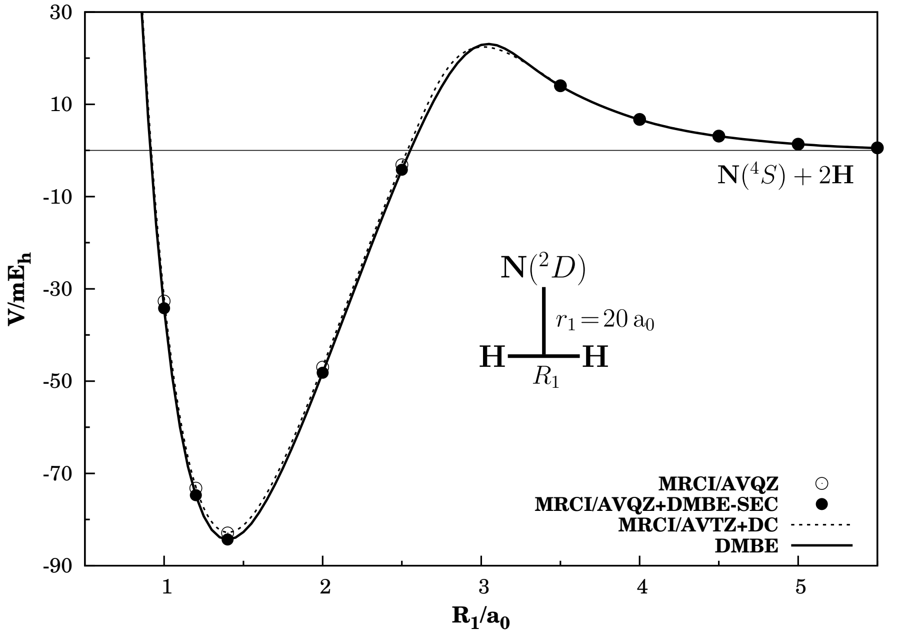

Figure 5. A comparison of the H_2 potential energy curves including the one-body term referring to the N (^2D) − N (^4S) excitation energy. The dashed line shows the MRCI/AVTZ curve obtained by interpolation using the reproducing Kernel-Hilbert space (RKHS) method [7], while the curve associated to the present DMBE potential energy surface is indicated by the solid line. Also shown are the MRCI/AVQZ (*open dots*) and MRCI/AVQZ+DMBE-SEC (*solid dots*) energies calculated at $r = 20\,a_0$. The reference energy refers to N (^4S) + H + H.

of the diatomic molecule. Thus, further *ab initio* work and possibly dynamical calculations are necessary to ascertain which of the above estimates (1.8 vs $2.1\,\mathrm{kcal\,mol^{-1}}$) is the most realistic one. Finally, Table 6 shows that there is a fairly good agreement between the DMBE and RKHS [7] potential energy surfaces as far the calculated vibrational frequencies are concerned, with the largest absolute deviations not generally exceeding $60\,\mathrm{cm^{-1}}$. Such deviations remain small when comparing the results obtained by fitting a local polynomial with those obtained from the DMBE potential energy surface, which corroborates the high quality of the present global fit.

The linear barrier has only been modeled via the final DMBE fit, and hence its attributes may not have been so definitely characterized. It is seen that the barrier height slightly overestimates previous theoretical values. Perhaps not

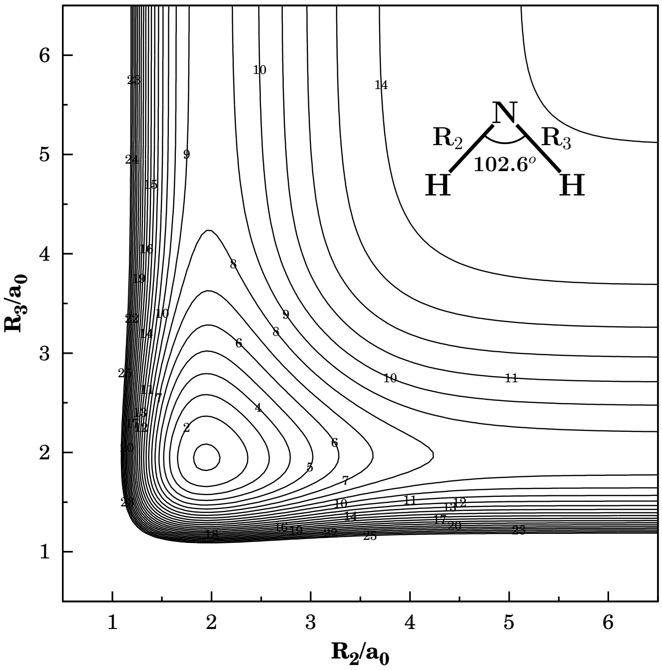

Figure 6. Contour plot for bond stretching in N − H − H, keeping the included angle fixed at 102.6°. Contours are equally spaced by $0.02\,E_\mathrm{h}$, starting at $-0.282\,E_\mathrm{h}$.

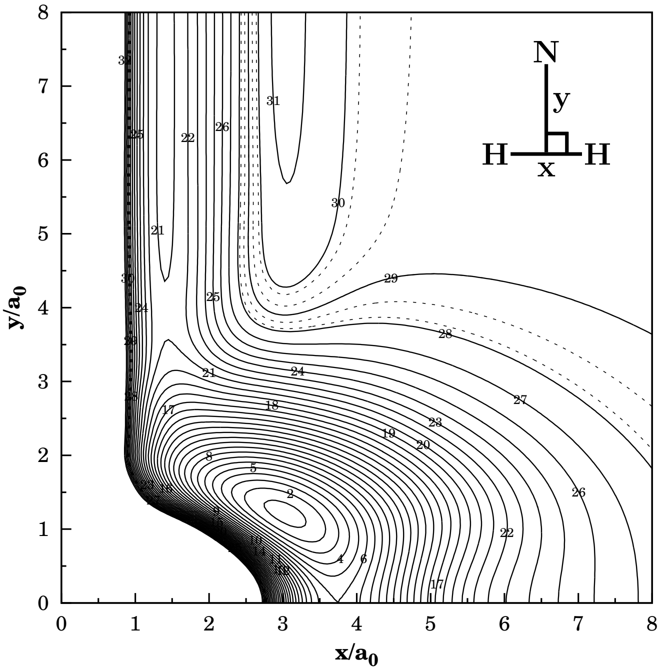

Figure 7. Contour plot for the C_{2v} insertion of the N atom into H_2. Contours are equally spaced by $0.01\,E_\mathrm{h}$, starting at $-0.282\,E_\mathrm{h}$. Shown in dashed are contours equally spaced by $0.004\,E_\mathrm{h}$, starting at $-0.01\,E_\mathrm{h}$.

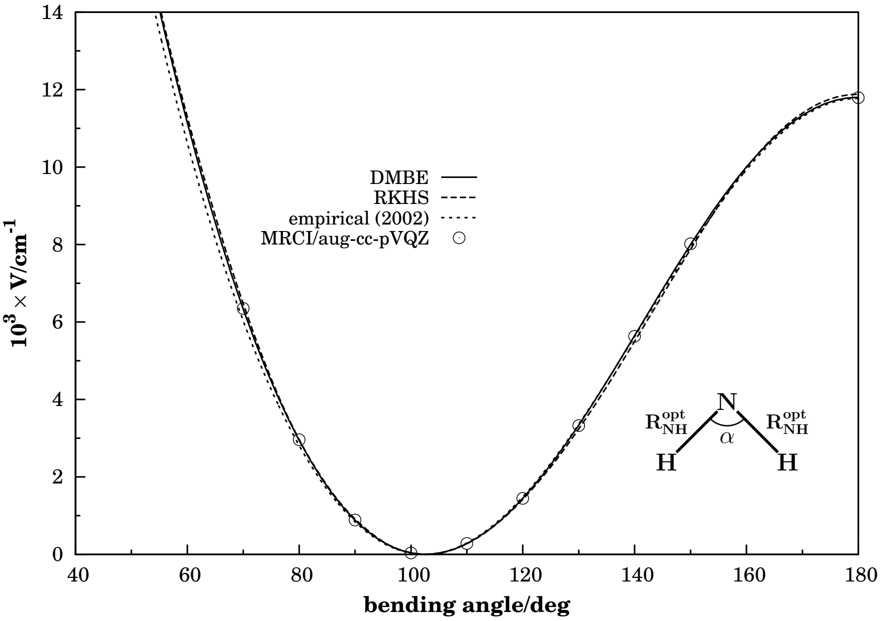

Figure 8. Optimized C_{2v} bending curve: *dashed line*, RKHS [7]; *dotted line*, empirical [14], *continuous line* DMBE (this work).

surprisingly, somewhat larger differences are also observed for the corresponding harmonic frequencies. Despite this, we may judge our results as providing an accurate representation of the true potential energy surface at the chosen level of theory.

Figures 6, 7, 8, 9, 10 and 11 illustrate the major topographical features of the $NH_2(\tilde{X}^2B_1)$ DMBE potential energy surface. Clearly, it has a smooth and correct behavior over the whole configuration space. Also visible are its major stationary points: C_{2v} and linear barriers, and the global minimum. Moreover, we observe from Figure 7 the $D_{\infty h}$ saddle point associated to the linear $^2\Pi$ structure where the $\tilde{X}$ and $\tilde{A}$ Renner-Teller states of NH_2 become degenerate. This stationary point has been properly characterized, and found to lie $1802\,\mathrm{cm}^{-1}$ above the minimum of the NH_2 potential energy surface at a $D_{\infty h}$ geometry with characteristic bond length of $R_2 = R_3 = 1.8695\,a_0$ and frequencies of $\omega_1\,(\mathrm{N-H})_{symm} = 3676\,\mathrm{cm}^{-1}$, $\omega_2\,(\mathrm{N-H})_{asym} = 6979\,\mathrm{cm}^{-1}$, and $\omega_3\,(\mathrm{bend}) = 1544\,\mathrm{cm}^{-1}$. Such a point corresponds to the maximum at 180° in the optimized bending plot of Figure 8, and corresponds in the RKHS function to a bending barrier of $11879\,\mathrm{cm}^{-1}$. A notable feature from this plot is the fairly good agreement between our optimized bending

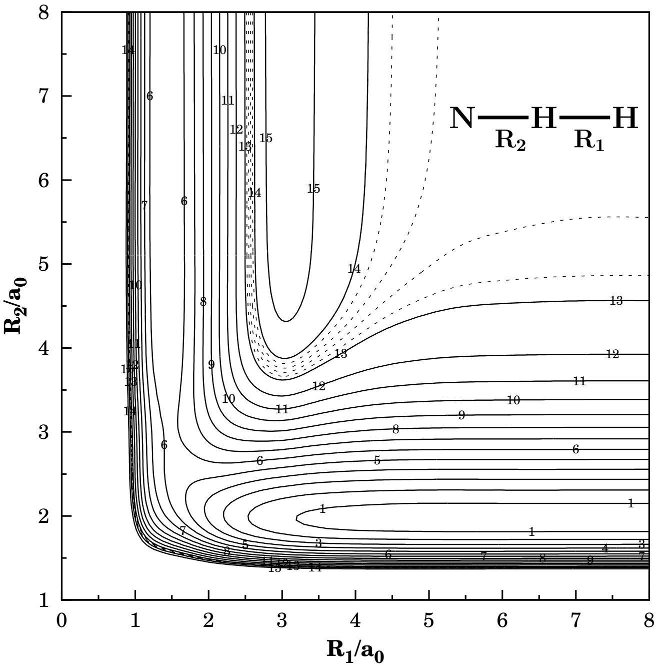

Figure 9. Contour plot for bond stretching in linear N − H − H configurations. Contours are equally spaced by $0.01\,E_\mathrm{h}$, starting at $-0.125\,E_\mathrm{h}$. Shown in dash are contours equally spaced by $0.002\,E_\mathrm{h}$, starting at $-0.003\,E_\mathrm{h}$.

curve and the one that we have obtained from the RKHS [7] potential energy surface, which exceeds the most recent empirical estimate [14] for the bending barrier height by $105\,\mathrm{cm}^{-1}$. Interestingly, such a barrier for linearization is predicted by the DMBE potential energy surface to be only $28\,\mathrm{cm}^{-1}$ larger than the empirical result obtained from the effective one-dimensional bending potential model of Duxbury and Alijah [14]. Indeed, the agreement with the latter is excellent over the whole range of angles shown in Figure 8, particularly for values larger than equilibrium where the optimized DMBE curve is almost indistinguishable from the empirical curve [14] within the scale of the Figure. This is a remarkable result since our fitted *ab initio* MRCI data points correspond to energies computed for an optimized characteristic bond length at each value of the valence angle (∠HNH). We should also emphasize that the *ab initio* points of the dense grid encompassing the $^2\Pi$ structure have been highly weighted in the least-squares fitting procedure such as to warrant an accurate description of the topographical features of potential energy surface at those regions of configuration space. Thus, we corroborate the recent trend to diminish the barrier for linearization when comparing with earlier theoretical [12] and empirical [38] estimates.

Figures 10 and 11 illustrate also the long range part of the potential energy surface which was fitted such as to provide a reliable description of the van der Waals minimum for the $\mathrm{N}-\mathrm{H}_2$ interaction: the rmsd of all fitted points (with $\mathrm{N}-\mathrm{H}_2$ distances larger than $5\,a_0$) in the energy range between the van der Waals minimum and the dissociation limit, in a total of 44 points, is $6.4\,\mathrm{cm}^{-1}$. Note that it shows a flat van der Waals valley, with two minima: one at a C_{2v} geometry, the other at a $C_{\infty v}$ one. Of these, the deepest minimum refers to the T-shaped structure, although its well depth is only $0.032\,\mathrm{kcal\,mol}^{-1}$ ($11.2\,\mathrm{cm}^{-1}$) larger than that of the collinear one; see Table 7 for other attributes. It should be pointed out that the van der Waals energies have been carefully fitted by attributing large weights to the corresponding points. Note that these energies correspond for $\mathrm{N}\cdots\mathrm{H}_2$ to AV5Z calculations, which are computationally demanding and hence have been carried out only for a small number of geometries. To avoid oscillations in the final DMBE form, a number of other points have been obtained by interpolation using reliable local procedures. For example, along the atom-diatom coordinate (R), we have used an extended-Rydberg form $V=-D\left(1+\sum_{i=1}^{N}a_is^i\right)\exp\left(-a_1s\right)$ to interpolate between the calculated points; $s=R-R_m$ is the displacement coordinate from the minimum associated to the chosen angle, and D and a_i are least-squares parameters. Such a procedure has also been employed to generate points at the intermediate distances between the last calculated point and the asymptote where the dynamical correlation energy by far dominates. Instead, to generate a few points at C_{2v} geometries where their convergence proved unsatisfactory, we have chosen a parabolic angular dependence centered at 90°. As shown in the one-dimensional plots of Figures 12 and 13, the final DMBE form reproduces quite satisfactorily all fitted data. It should be emphasized that the topography of the AV5Z potential energy surface at the $\mathrm{N}\cdots\mathrm{H}_2$ van der Waals region differs drastically from the one calculated at the MRCI/AVTZ level, while the MRCI/AVQZ one is intermediate and confirms the tendency to the AV5Z results. This is illustrated in Figure 14, which shows the MRCI minimum energy paths for the above three correlated consistent basis sets as a function of the Jacobi angle (the points are approximate, and have been ob-

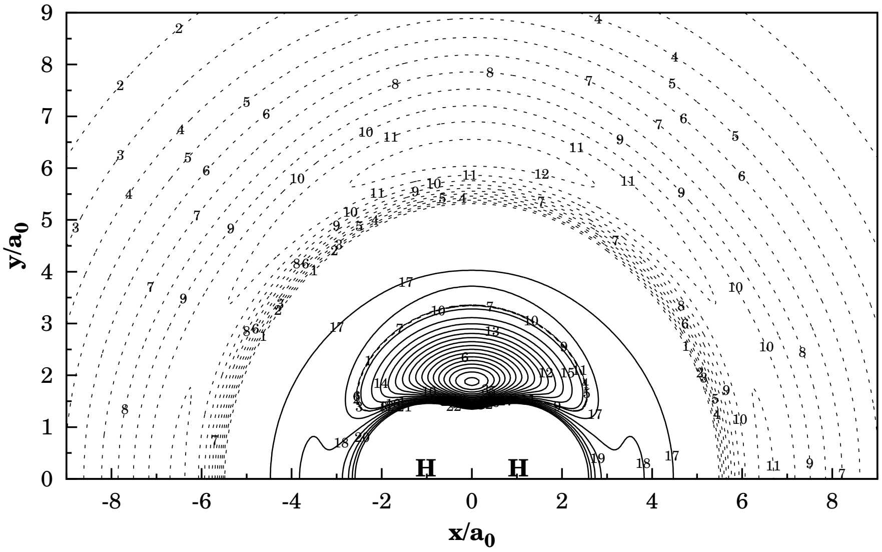

Figure 10. Contour plot for a N atom moving around a H_2 molecule fixed at the equilibrium geometry $R_1 = 1.401\,a_0$ and lying along the X axis with the center of the bond fixed at the origin. Contours are equally spaced by $0.005\,E_\mathrm{h}$, starting at $-0.161\,E_\mathrm{h}$. Shown in dash are contours equally spaced by $-0.000035\,E_\mathrm{h}$, starting at $-0.084336\,E_\mathrm{h}$.

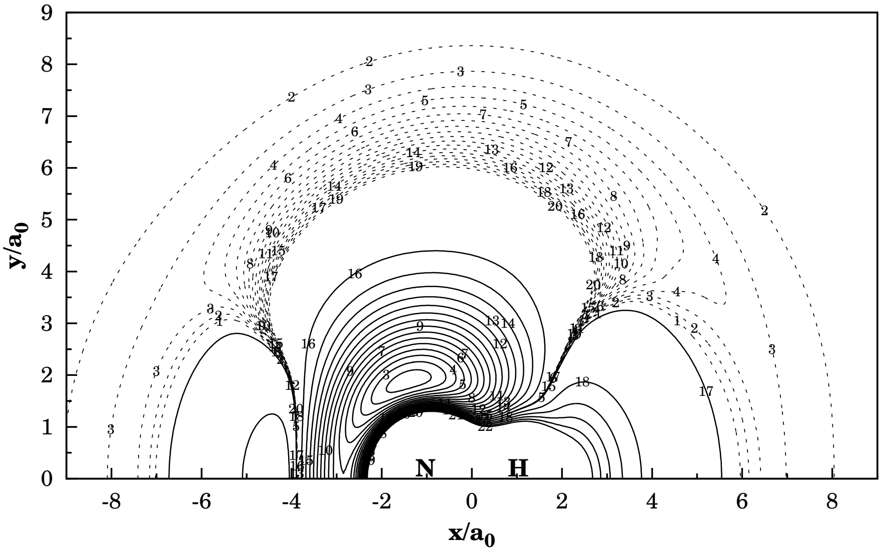

Figure 11. Contour plot for a H atom moving around a NH diatomic fixed at the equilibrium geometry, $R_\mathrm{NH} = 1.965\,a_0$, which lies along the X axis with the center of the bond fixed at the origin. Contours are equally spaced by $0.01\,E_\mathrm{h}$, starting at $-0.29\,E_\mathrm{h}$. Shown in dash are contours equally spaced by $-0.00005\,E_\mathrm{h}$, starting at $-0.130208\,E_\mathrm{h}$.

Table 7. Attributes of N $(^2D) - \mathrm{H}_2$ van der Waals minima.

Feature	RKHS[a]	DMBE[b]		
		C_{2v} min.[c]	$C_{\infty v}$ min.[c]	C_s s.p.[d]
$R_{\mathrm{H-H}}/a_0$	1.405	1.3995	1.3994	1.3990
$R_{\mathrm{N-H}}/a_0$	5.5571	6.2996	5.8191	5.7847
∠NHH	180°	90°	180°	153°
$\Delta V/\mathrm{kcal\,mol^{-1}}$	−0.2761	−0.2510[e]	−0.2228[e]	−0.2197[e]
ω_1^f (intra) $/\mathrm{cm}^{-1}$	4392	4428	4394	4405
ω_2^g (inter) $/\mathrm{cm}^{-1}$	231	79	63	73
ω_3^h (bend) $/\mathrm{cm}^{-1}$	81	57	58	$64i$

[a] Ref. [7]. [b] This work. [c] van der Waals minimum. [d] Saddle point connecting the two van der Waals minima. [e] Relative to the N $(^2D) + \mathrm{H}_2$ asymptote which is $-55.45143412\,E_\mathrm{h}$ and $-55.60727004\,E_\mathrm{h}$ at the FVCAS and MRCI/aug-cc-pV5Z levels, respectively. [f] Associated to the intramolecular diatomic stretching frequency. [g] Associated to the intermolecular atom-diatom stretching frequency. [h] Associated to the bending (nearly free-rotor) motion.

tained by interpolation of the three calculated energies closest to the minimum for a given Jacobi angle by using a quadratic form). Also indicated for comparison is the curve associated to the DMBE potential energy surface. Clearly, the agreement with the MRCI/AV5Z results is rather satisfactory, especially recalling the discrepancy amongst the *ab initio* results themselves. Of course, an improvement could be obtained either by increasing the order of the polynomial centered at the T-shaped van der Waals minimum or adding an extra polynomial centered at the linear van der Waals structure. For the reasons given in section 3 and given the coarse grid of calculated MRCI/AV5Z points, such an approach did not seem justified. In turn, the H$\cdots$NH channel is purely attractive, and hence no such calculations have been judged to be necessary there.

The isotropic and leading anisotropic potentials are two important quantities for the study of $\mathrm{N} - \mathrm{H}_2$ scattering processes [39], being shown in panels (a) to (c) of Figure 15 and Table 8. Specifically, the isotropic average potential V_0 determines how close on average the atom and molecule can approach each other, while the magnitude of V_2 indicates whether or not the molecule prefers to orient

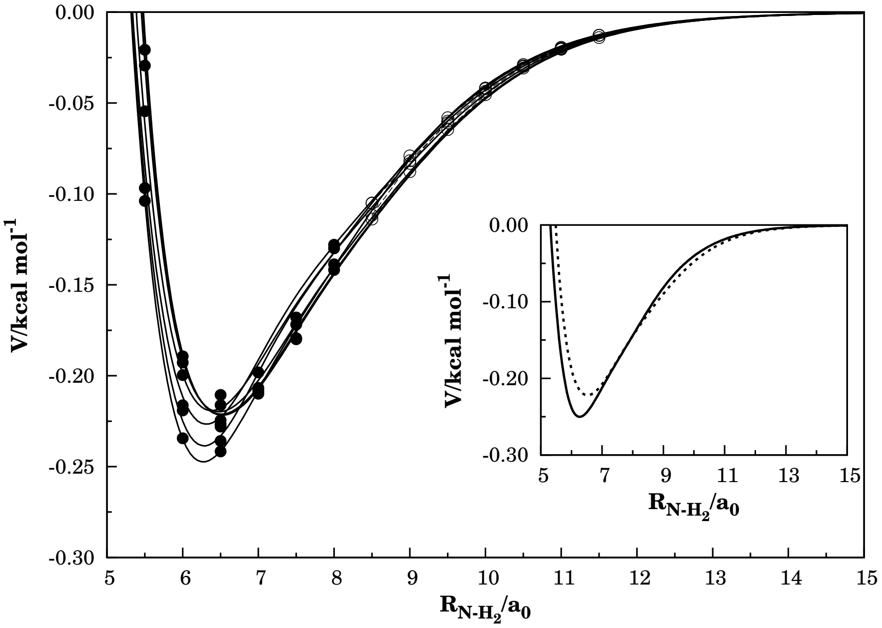

Figure 12. Cut of DMBE potential energy surface along the atom-diatom radial coordinate for a fixed diatomic bond distance of $R_1 = 1.401\,a_0$. The *solid points* indicate the actually calculated MRCI/AV5Z energies, while the *open circles* have been estimated by using an extended-Rydberg form (see the text). Shown in the insert are the curves for 0° and 90°, which cross each other at about $r_1 = 8.5\,a_0$.

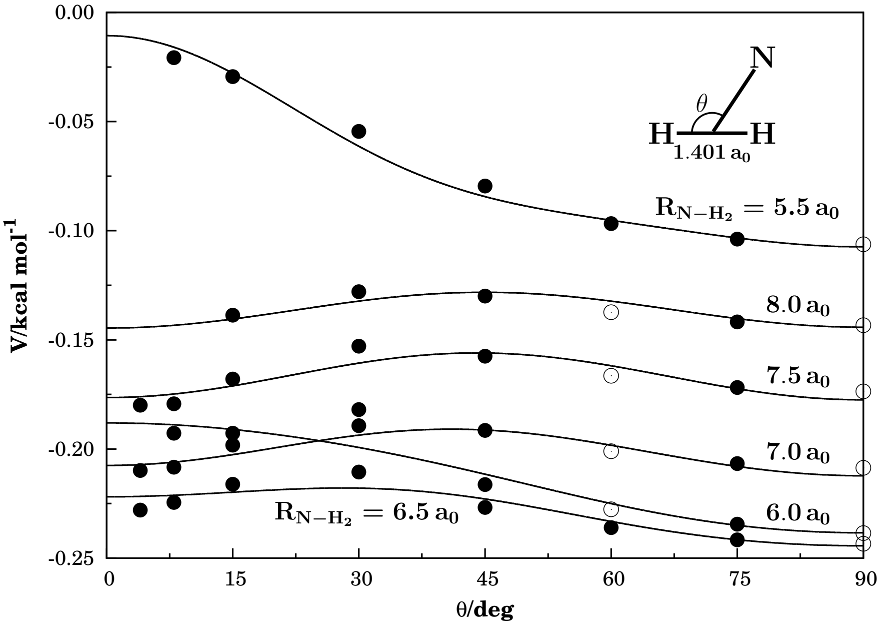

Figure 13. Cut of DMBE potential energy surface along the Jacobi angle for a fixed diatomic bond distance of $R_1 = 1.401\,a_0$. Symbols as in Figure 12.

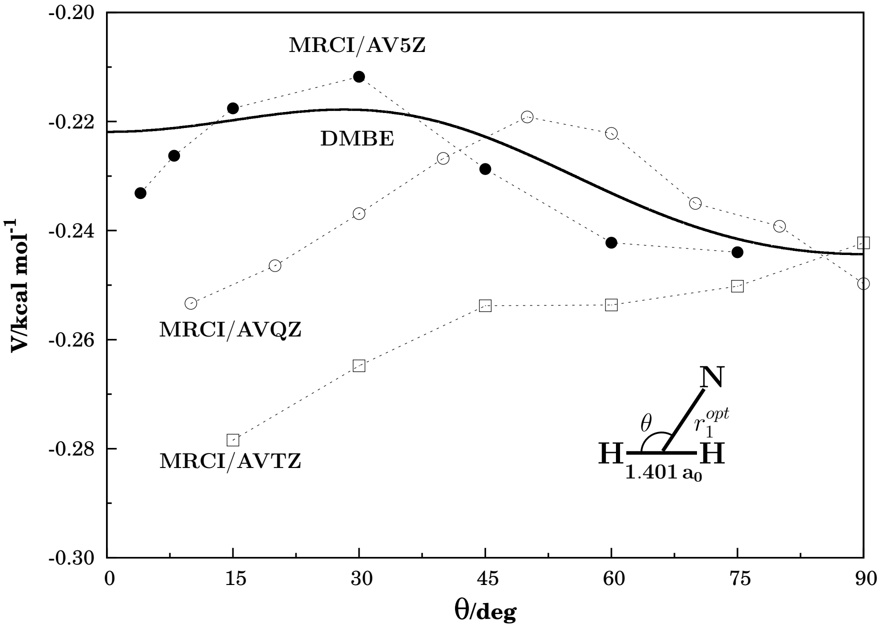

Figure 14. A comparison of the *ab initio* minimum energy paths for isomerization between the collinear and T-shaped van der Waals structures. Also indicated is the corresponding path for the DMBE potential energy surface. For each Jacobi angle, the *ab initio* results have been obtained via a quadratic interpolation. The diatomic bond distance has been fixed at $R_1 = 1.401\,a_0$.

its axis along the direction of the incoming atom: a negative value favors the collinear approach while a positive value favors the approach through an isosceles triangular geometry. The barrier in V_0 located near $3.5\,a_0$ [see panel (a) of Figure 15] corresponds to the C_{2v} transition state, as corroborated by the positive value of V_2 at such a distance. In turn, the negative sign of V_2 at distances larger than $8.5\,a_0$, indicates that the van der Waals interaction energy is larger for such collinear geometries [see panel (b) of Figure 15] as one would expect from the larger polarizability of the hydrogen molecule along the internuclear axis. Note, however, that the anisotropy is positive at the region of the van der Waals minimum in the isotropic potential (V_0). This is due to the deepest well associated to the T-shaped van der Waals structure. This contrasts with the the RKHS surface, which predicts the van der Waals minimum to occur at a collinear geometry. Recall that the MRCI calculations carried out using AVTZ, AVQZ, and AV5Z basis sets corroborate the tendency to a shallow van der Waals valley (see

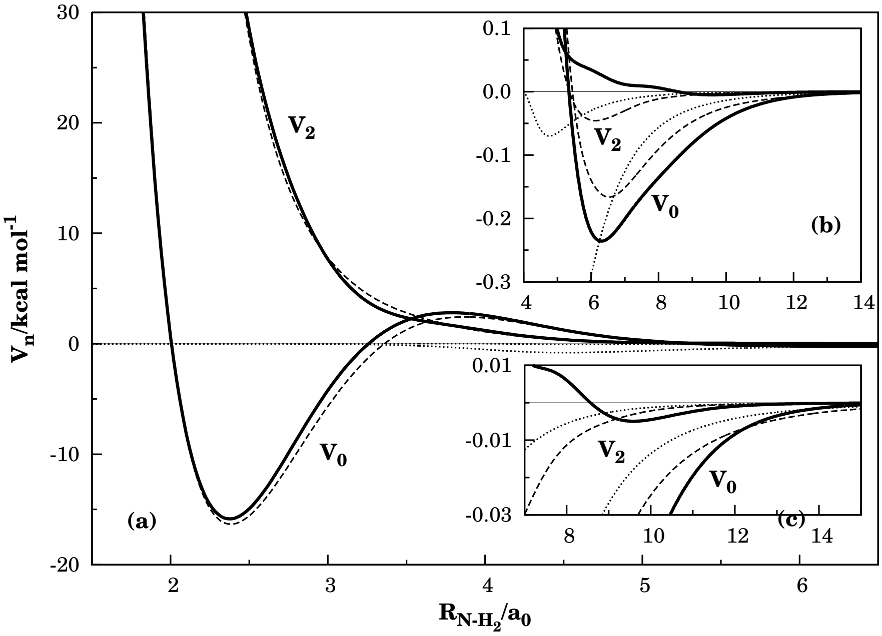

Figure 15. Isotropic (V_0) and leading anisotropic (V_2) components of the $N-H_2$ interaction potential, with the diatomic molecule fixed at the equilibrium geometry. *continuous line*, DMBE; *dashed line*, RKHS; *dotted line*, three-body dynamical correlation term (leading to asymptotic atom-diatom dispersion interaction at large distances) in Eq. (17). The axes in all panels have the same units. Note that in all *panels* the *dotted line* lying closest to the $r_1 = R_{N-H_2}$ axis at the reference energy refers to V_2.

Table 8. Attributes of leading terms in Legendre expansion of $N\,(^2D) - H_2$ van der Waals potentials.

Feature	RKHS[a]	DMBE[b]
Spherically averaged potential, V_0		
R_m^c/a_0	6.30	6.31
ϵ^d/kcal mol^{-1}	0.160	0.236
Leading anisotropic term, V_2		
R_m^c/a_0	6.10	9.59
ϵ^d/kcal mol^{-1}	0.052	0.005

[a] Ref. 7. [b] This work. [c] Geometry of van der Waals minimum. [d] Well depth of van der Waals minimum.

Figure 13), with minima being located both at T-shaped and collinear structures. The small bump in V_2 between 6.5 and 7.5 a_0 may be attributed to the fact that the T-shaped minimum occurs at a slightly smaller atom-diatom bond distance than the collinear van der Waals structure. Since the N (^2D) + H$_2$ reaction has been shown to display a preference to occur via an insertion mechanism, it is possible that this subtle detail may have practical implications for the scattering especially at low collision energies. We further observe that the spherically averaged component of the RKHS [7] surface has a slightly shallower van der Waals minimum in comparison with the DMBE one but is somewhat more attractive at large distances (see Table 8 for the numerical attributes of V_0 and V_2). Moreover, the DMBE potential energy surface has a significantly smaller anisotropy (the well depth of V_2 is only 1.6 cm^{-1}) than the RKHS [7] surface in accordance with the trends predicted from the MRCI calculations; see the insert of Figure 12, and Figure 14. Finally, we emphasize (see panel (c) of Figure 15) that the current potential energy surface reproduces the assumed long range interactions described in section 3.2.1 both at the N (^2D)+H$_2$ and H $\cdots$ NH asymptotes, a major general asset of DMBE theory.

5 Concluding remarks

We have suggested an improved switching function formalism that allows an accurate description of the ground state potential energy surface of NH$_2$ by a single-sheeted DMBE form. This has been calibrated from newly calculated MRCI energies distributed over all geometries of chemical relevance. Given the high level of the calculated *ab initio* energies, the resulting DMBE potential energy surface is possibly the most accurate function reported thus far for the title system, although it lies close to that obtained via a RKHS interpolation [7]. Clearly, a more definite assessment of the accuracy of the DMBE potential energy surface[1] cannot be made prior to use in dynamics calculations. Its simplicity and quality suggest though that it should be recommendable for both reactive and non-reactive studies of N (^2D) + H$_2$ collisions.

---

[1] For the computer code, the reader should contact the authors.

Acknowledgment

This work has the support of Fundação para a Ciência e Tecnologia, Portugal, under programmes POCTI and FEDER. The partial support of the European Community's Human Potential Programme under contract HPRN-CT-2002-00170 is also appreciated.

References

[1] Suzuki T, Shihira Y, Sato T, Umemoto H, Tsunashima S (1993) J Chem Soc Faraday Trans 89:995

[2] Kobayashi H, Takayanagi T, Yokoyama K, Sato T, Tsunashima S (1995) J Chem Soc Faraday Trans 91:3771

[3] Dodd JA, Lipson SJ, Flanagan DJ, Blumberg WAM, Pearson JC, Green BD (1991) J Chem Phys 94:4301

[4] Umemoto H, Matsumoto K (1996) J Chem Phys 104:640

[5] Umemoto H, Asai T, Kimura Y (1997) J Chem Phys 106:4985

[6] Alagia M, Balucani N, Cartechini L, Cachavecchia P, Volpi GG, Pederson LA, Schatz GC, Lendvay G, Harding LB, Hollebeek T, Ho T-S, Rabitz H (1999) J Chem Phys 110:8857

[7] Ho T-S, Rabitz H, Aoiz FJ, Baares L, Vzquez SA, Harding LB (2003) J Chem Phys 119:3063

[8] Aronszajn N (1950) Trans Am Math Soc 68:337

[9] de Boor C, Lynch R (1966) J Math Mech 15:953

[10] Davis PJ (1975) Interpolation and approximation, Dover, New York

[11] Pederson LA, Schatz GC, Ho T-S, Hollebeek T, Rabitz H, Harding LB (1999) J Chem Phys 110:9091

[12] Buenker RJ, Perić M, Peyerimhoff SD, Marian R (1981) Mol Phys 43:987

[13] Gabriel G, Chambaud G, Rosmus P, Carter S, Handy N (1994) Mol Phys 6:1445

[14] Duxbury G, Alijah A (2002) J Mol Spectrosc 211:31

[15] Varandas AJC (1988) Adv Chem Phys 74:255

[16] Varandas AJC (2000) Lecture notes in chemistry. In: Laganá A, Riganelli A, (eds) Vol. 75 Springer, Berlin Heidelberg New York p 33

[17] Varandas AJC (2004) Conical intersections: electronic structure, dynamics and spectroscopy. In: Yarkony D, Köppel H, Domcke W, (eds) Champ. 5. World Scientific Publishing: Singapore p 205.

[18] Murrell JN, Carter S (1984) J Phys Chem 88:4887

[19] Dunning TH (1989) J Chem Phys 90:1007

[20] Kendall R, Dunning Jr. T, Harrison R (1992) J Chem Phys 96:6769

[21] Varandas AJC (1989) J Chem Phys 90:4379

[22] Werner H-J, Knowles PJ (1988) J Chem Phys 89:5803

[23] Knowles PJ, Werner H-J (1985) Chem Phys Lett 115:259

[24] Werner H-J, Knowles PJ (1998) MOLPRO is a package of *ab initio* programs written by Werner H-J, Knowles PJ, with contributions from Almlöf J, Amos RD, Deegan MJO, Elbert ST, Hampel C, Meyer W, Peterson KA, Pitzer R, Stone AJ, Taylor PR, Lindh R

[25] Varandas AJC (1992) Chem Phys Lett 194:333

[26] Anderson WR (1989) J Phys Chem 93:530

[27] Boys F, Bernardi F (1970) Mol Phys 19:553

[28] Varandas AJC, Silva JD (1992) J Chem Soc Faraday Trans 88:941

[29] Varandas AJC (1985) J Mol Struct Theochem 120:401

[30] Le Roy RJ (1973) Spec Period Rep Chem Soc Mol Spectrosc 1:113

[31] Varandas AJC (1996) J Chem Phys 105:3524

[32] Varandas AJC, Rodrigues SPJ (1997) J Chem Phys 106:9647

[33] Stallcop JR, Bauschlicher CW, Partridge H, Langhoff SR, Levin E (1992) J Chem Phys 97:5579

[34] Varandas AJC, Rodrigues SPJ (2006) J Phys Chem A 110:485

[35] Matías MA, Varandas AJC (1990) Mol Phys 70:623

[36] Martínez-Nuñez E, Varandas AJC (2001) J Phys Chem 105:5923

[37] Takayanagi T, Kurosaki Y, Yokoyama K (2000) Chem Phys Lett 321:106

[38] Jungen C, Halin K-EJ, Merer AJ (1980) Mol Phys 40:65

[39] Varandas AJC (1979) J Chem Phys 70:3786

Phys. Chem. Chem. Phys. **7**, 2867–2873 (2005).

Repulsive double many-body expansion potential energy surface for the reactions $N\left({}^4S\right) + H_2 \rightleftharpoons NH\left(X^3\Sigma^-\right) + H$ from accurate *ab initio* calculations

L.A. Poveda and A.J.C. Varandas

Departamento de Química, Universidade de Coimbra
3004-535 Coimbra Codex, Portugal.

(Received: April 21, 2005; In final form: June 7, 2005)

Abstract

A single-sheeted DMBE potential energy surface is reported for the reactions $N\left({}^4S\right) + H_2 \rightleftharpoons NH\left(X^3\Sigma^-\right)+H$ based on a fit to accurate multireference configuration interaction energies. These have been calculated using the aug-cc-pVQZ basis set of Dunning and the full valence complete active space wave function as reference, being semi-empirically corrected by scaling the two-body and three-body dynamical correlation energies. The topographical features of the novel global potential energy surface are examined in detail, including a conical intersection involving the two first ${}^4A''$ potential energy surfaces which has been transformed into an avoided crossing in the present single-sheeted representation.

1 Introduction

The reactions involving nitrogen atoms play an important role in both the combustion of nitrogen containing fuels and atmospheric chemistry. In particular, the reactions

$$\mathrm{N}\left({}^4S\right) + \mathrm{H}_2\left(X^1\Sigma_g^+\right) \rightleftharpoons \mathrm{NH}\left(X^3\Sigma^-\right) + \mathrm{H}\left({}^2S\right) \tag{1}$$

$$\mathrm{H}_a\left({}^2S\right) + \mathrm{NH}_b\left(X^3\Sigma^-\right) \rightarrow \mathrm{NH}_a\left(X^3\Sigma^-\right) + \mathrm{H}_b\left({}^2S\right) \tag{2}$$

are of relevance for studying the thermal decomposition or oxidation of ammonia, and the decay of imidogen (NH). While the reactions of electronically excited $\mathrm{N}\,({}^2D)$ and $\mathrm{N}\,({}^2P)$ with H_2 have been widely studied,[1–9] less attention has been paid to the reaction of ground state $\mathrm{N}\,({}^4S)$ with H_2. Amongst other reasons, this is possibly due to the difficulty in preparing translationally hot nitrogen atoms. In fact, there is some consensus both from theoretical and experimental studies that the forward reaction (1) has a strongly repulsive entrance channel that precludes its occurrence at room or even medium temperatures.[10–15]

From the experimental side, Koshi *et al.*[11] studied the reaction (1) over the temperature range $1600 \leq T/\mathrm{K} \leq 2300$ by atomic resonance absorption in a shock tube apparatus. In the same paper, the authors reported the first theoretical estimate of the barrier height for reaction (1) via MP4/6-31G** calculations at HF/4-31G optimized geometries. The predicted barrier height for the forward quartet-state reaction was $35.5\,\mathrm{kcal\,mol^{-1}}$ in accordance with the experimental result of $33 \pm 7\,\mathrm{kcal\,mol^{-1}}$. Moreover, they have estimated[11] the barrier height for the reverse reaction to be $4.4\,\mathrm{kcal\,mol^{-1}}$. In turn, from similar experiments covering the temperature range $1950 \leq T/\mathrm{K} \leq 2850$, Davidson and Hanson[10] have determined lower activation energies of 25.14 and $0.3\,\mathrm{kcal\,mol^{-1}}$ for the forward and reverse reactions, respectively. A more reliable estimate of the activation energy for the reverse reaction (1) has been calculated by Xu *et al.*[12] by scaling all the correlation energy in UMP4/6-311G** calculations (MP-SAC4). They predicted a barrier height of $1.68\,\mathrm{kcal\,mol^{-1}}$ in good agreement with the more recent experiments, and demonstrated the importance of the dynamical correlation in the correct description of the title system. In a more ambitious work, Zhang *et al.*[14] explored the potential energy surfaces for the low-lying electronic states with relevance for the reaction (1). They performed geometric optimizations, internal reaction coordinate (IRC) calculations, and frequency analyzes at the QDCISD/cc-pVDZ level. The energetics along the IRC path was then improved at the QCISD(TQ)/cc-pVTZ level, leading to predicted activation energies for the forward and reverse reactions of 29.6 and 0.5 kcal mol^{-1}, respectively.

The first potential energy surface for the title reactions was calculated by Pascual *et al.*[15] using a modified version of the GROW program of Collins *et al.*[16–19] where the surface is constructed via a Shepard's interpolation of *ab initio* data that includes the energy, energy gradient, and second derivatives at 156 molecular geometries. Such data has been calculated at the MCQDPT2/6-311^{++}G** level by using the full valence complete active space FVCAS [*i.e.*, a CAS(7,6)] wave function as reference. Their results show a reasonable accordance with previous theoretical and experimental values, while demonstrating also the importance of describing adequately the dynamical correlation in studies of the title reactions.

In this work, we report a realistic global potential energy surface for reactions (1) and (2) from double many-body expansion (DMBE) theory.[20–24] Being a fragment of larger N_xH_y species such as those of relevance in studying the synthesis of ammonia, it may then be of key importance for constructing DMBE forms for those systems, an endeavor to which we are currently committed. To calibrate the DMBE form, over 1800 *ab initio* points have been calculated at the multireference configuration interaction (MRCI) level based on the reference FVCAS wave function by employing the aug-cc-pVQZ (AVQZ) basis set of Dunning.[25, 26] Such MRCI energies were subsequently corrected by means of the double many-body expansion-scaled external correlation (DMBE-SEC[27]) method to extrapolate to the complete basis set/complete CI limits. As usual in DMBE theory,[20–24] the potential energy surface shows the correct long-range behavior at all dissociation limits.

After this work has been completed, a paper appeared by Adam *et al.*[28] that reports an experimental and theoretical investigation of both the reverse of reaction (1) and reaction (2) using a semi-numerical potential energy surface based on a 3*D* cubic-spline fit to an extensive data set (18432) of *ab initio* points also calculated at the MRCI/AVQZ level. These authors have additionally performed a number of calculations using larger basis sets with a view to estimate the barrier height for such a reaction. They concluded that there is a tendency for a slight increase of the barrier height with basis set quality (varying from 1.906 to 2.323 kcal mol^{-1} for the cc-pVTZ and cc-pV6Z basis sets, respectively).

The paper is organized as follows. Section 2 describes the *ab initio* calculations, while the analytical representation of the potential energy surface is discussed in section 3. Specifically, section 3.1 focuses on the two-body energy terms, while section 3.2 concentrates on the three-body ones. The main topographical features of the $NH_2\,(^4A'')$ potential energy surface are examined in section 4. Section 5 gathers the conclusions.

2 *Ab initio* calculations

The *ab initio* calculations have been carried out at the MRCI[29] level by using as reference the FVCAS[30] wave function. This involves 7 correlated electrons in 6 active orbitals ($5a'$+$1a''$), amounting to a total of 50 configuration state functions. The AVQZ basis set of Dunning[25, 26] has been used, with the calculations being done with the MOLPRO[31] package at 1812 grid points defined by $1.0 \leq R_{H_2}/a_0 \leq 7.0$, $1.5 \leq r_{N-H_2}/a_0 \leq 10.0$ and $0.0 \leq \gamma/^\circ \leq 90$ for $N-H_2$ geometries, and $1.5 \leq R_{NH}/a_0 \leq 3.0$, $1.5 \leq r_{H-NH}/a_0 \leq 10.0$ and $0.0 \leq \gamma/^\circ \leq 180$ for $H-NH$ geometries; r, R and γ are the atom-diatom Jacobi coordinates.

The *ab initio* energies calculated in this way were then semiempirically corrected by the DMBE-SEC[27] method to account for the excitations beyond singles and doubles and, most importantly, for the incompleteness of the basis set. Thus, the total DMBE-SEC interaction energy is written as[27]

$$V\,(\mathbf{R}) = V_{\mathrm{FVCAS}}\,(\mathbf{R}) + V_{\mathrm{SEC}}\,(\mathbf{R}) \tag{3}$$

where

$$V_{\mathrm{FVCAS}}\,(\mathbf{R}) = \sum_{\mathrm{AB}} V^{(2)}_{\mathrm{AB,FVCAS}}\,(R_{\mathrm{AB}}) + V^{(3)}_{\mathrm{ABC,FVCAS}}\,(R_{\mathrm{AB}}, R_{\mathrm{BC}}, R_{\mathrm{AC}}) \tag{4}$$

$$V_{\mathrm{SEC}}\,(\mathbf{R}) = \sum_{\mathrm{AB}} V^{(2)}_{\mathrm{AB,SEC}}\,(R_{\mathrm{AB}}) + V^{(3)}_{\mathrm{ABC,SEC}}\,(R_{\mathrm{AB}}, R_{\mathrm{BC}}, R_{\mathrm{AC}}) \tag{5}$$

and $\mathbf{R} = \{R_1, R_2, R_3\}$ is a collective variable of the three interatomic distances.

In turn, the first two terms of the SEC series expansion assume the form

$$V^{(2)}_{\mathrm{AB,SEC}}\left(R_{\mathrm{AB}}\right) = \frac{V^{(2)}_{\mathrm{AB,FVCAS-CISD}}\left(R_{\mathrm{AB}}\right) - V^{(2)}_{\mathrm{AB,FVCAS}}\left(R_{\mathrm{AB}}\right)}{F^{(2)}_{\mathrm{AB}}} \tag{6}$$

$$V^{(3)}_{\mathrm{ABC,SEC}}\left(\mathbf{R}\right) = \frac{V^{(3)}_{\mathrm{ABC,FVCAS-CISD}}\left(\mathbf{R}\right) - V^{(3)}_{\mathrm{ABC,SEC}}\left(\mathbf{R}\right)}{F^{(3)}_{\mathrm{ABC}}} \tag{7}$$

Following previous work,[27] the $F^{(2)}_{\mathrm{AB}}$ parameter in Eq. (6) has been chosen to reproduce the bond dissociation energy of the diatomic AB, while $F^{(3)}_{\mathrm{ABC}}$ has been estimated as the average of the three two-body F-factors. Such a procedure leads to[9] $F^{(2)}_{\mathrm{HH}} = 0.9773$, $F^{(2)}_{\mathrm{NH}} = 0.9479$, and $F^{(3)}_{\mathrm{NHH}} = 0.9577$.

3 Potential energy surface

Within the DMBE[20–24] framework, every n-body term is split into two contributions: the extended Hartree-Fock (V_{EHF}) and dynamical correlation (V_{dc}) energies. Thus, for a three-body system, one has:

$$V_{\mathrm{EHF}}\left(\mathbf{R}\right) = \sum_{i=1}^{3} V^{(2)}_{\mathrm{EHF}}\left(R_i\right) + V^{(3)}_{\mathrm{EHF}}\left(\mathbf{R}\right) \tag{8}$$

$$V_{\mathrm{dc}}\left(\mathbf{R}\right) = \sum_{i=1}^{3} V^{(2)}_{\mathrm{dc}}\left(R_i\right) + V^{(3)}_{\mathrm{dc}}\left(\mathbf{R}\right) \tag{9}$$

with the EHF contributions being generally calibrated from available *ab initio* data by using a suitable functional form. In turn, the dc energies are modelled semiempirically from the long-range dispersion energy coefficients. When judged relevant, the induction and electrostatic long range coefficients are also taken into consideration in modelling the long range parts of the potential energy surface. The following sections give the details of the specific analytical forms that we have employed to represent the various contributions in Eqs. (8) and (9).

3.1 Two-body energy terms

As usual, the potential energy curve for the two-body fragments is based on the extended Hartree-Fock approximate correlation energy method for diatomic molecules, including the united atom limit (EHFACE2U[32]), which shows the correct behavior at the asymptotes $R \rightarrow 0$, and $R \rightarrow \infty$. Since accurate EHFACE2U functions have been reported for the electronic states of relevance in the present work, we employ them here. Specifically, the potential curve of $H_2\left(X^1\Sigma_g^+\right)$ has been taken from Ref. 33, while that of $NH\left(X^3\Sigma^-\right)$ was calibrated from the MRCI+Q *ab initio* points of Stallcop *et al.*[34] as described elsewhere.[35] Table 1 shows that they provide an accurate representation of our own *ab initio* energies; for increased accessibility we give the results in angstrom and $\mathrm{kJ\,mol^{-1}}$, rather than in Bohr and E_h or $\mathrm{kcal\,mol^{-1}}$ which we keep in the rest of the paper (for further details, see the original papers and ref. 9).

3.2 Three-body energy terms

3.2.1 Dynamical correlation energy

To model this energy contribution we employ the following semiempirical form:[33]

$$V_{\mathrm{dc}}^{(3)} = \sum_i \sum_n f_i\left(\mathbf{R}\right) C_n^{(i)}\left(R_i, \theta_i\right) \chi_n\left(r_i\right) r_i^{-n} \tag{10}$$

where r_i, θ_i and R_i are the Jacobi coordinates corresponding to a specific geometry of the triatomic species. In turn, $f_i = \frac{1}{2}\{1 - \tanh[\xi\left(\eta R_i - R_j - R_k\right)]\}$ is a convenient switching function, with corresponding expressions applying for f_j and f_k. Following previous work,[36] we adopt $\eta = 6$ and fix $\xi = 1.0 a_0^{-1}$. Regarding the damping function $\chi_n\left(r_i\right)$, we have used the form adopted elsewhere;[9, 33] r_i is the center-of-mass separation for the relevant atom-diatom channel. All other definitions and numerical values were kept as in Ref. 9, being the reader referred to this paper for details.

3.2.2 Extended Hartree-Fock energy

By removing, for a given triatomic geometry, the sum of the two-body energy terms from the corresponding DMBE-SEC interaction energies in Eq. (3), which are defined with respect to the infinitely separated ground-state atoms, one obtains the total three-body energy. By then subtracting the three-body dynamical correlation contribution in Eq. (10) from the total three-body energy, one obtains

Table 1. Comparison of bond distances and harmonic vibrational frequencies for diatomic fragments.

	$H_2\left(X^1\Sigma_g^+\right)$			$NH\,(X^3\Sigma^-)$		
	R_e/Å	ω/cm^{-1}	$D_e/\mathrm{kJ\,mol}^{-1}$	R_e/Å	ω/cm^{-1}	$D_e/\mathrm{kJ\,mol}^{-1}$
UHF/6-311G**[a]	0.736	4594		1.023	3502	
UMP2/6-311G**[a]	0.738	4534		1.034	3392	
UMP4/6-311G**[a]	0.742	4454		1.042	3295	
MCQDPT2/6-311++G**[b]	0.747	4379	−424.5	1.048	3292	−325.3
UQCISD/cc-pVDZ[c]	0.761	4384		1.054	3218	
QCISD(T)/cc-pVTZ[b]	0.743	4410		1.039	3265	
MRCI+Q[d]				1.039	3261	−342.1
MRCI+Q[e]				1.040	3266	−341.8
MRCI/aug-cc-pVQZ[f]	0.742	4401	−456.8	1.038	3272	−338.7
MRCI-SEC[g]	0.742	4401	−458.1	1.038	3274	−341.8
DMBE[h]	0.741	4393	−458.1	1.040	3245	−431.8
KW[i] ('exact')	0.741	4401	−458.1			
Exp.[j]	0.741	4401	−458.4	1.036	3282	
Exp.[k]				1.037	3281	−327.9±15.5
Exp.[l]				1.037	3266	

[a] Ref. 12. [b] Ref. 15. [c] Ref. 14. [d] Ref. 38, using a $[5s4p3d2f1g/4s3p2d]$ contracted Gaussian basis set. [e] Ref. 34, using an extensive Gaussian basis set. [f] This work, *ab initio* calculations. [g] This work, based on a Taylor series expansion fit to a fine grid of MRCI-SEC energies, Eq. (6), calculated in the vicinity of the minimum. [h] This work, using the EHFACE2U curves also employed in Ref. 9. [i] Ref. 39. [j] Ref. 40. [k] Ref. 41. [l] Ref. 45.

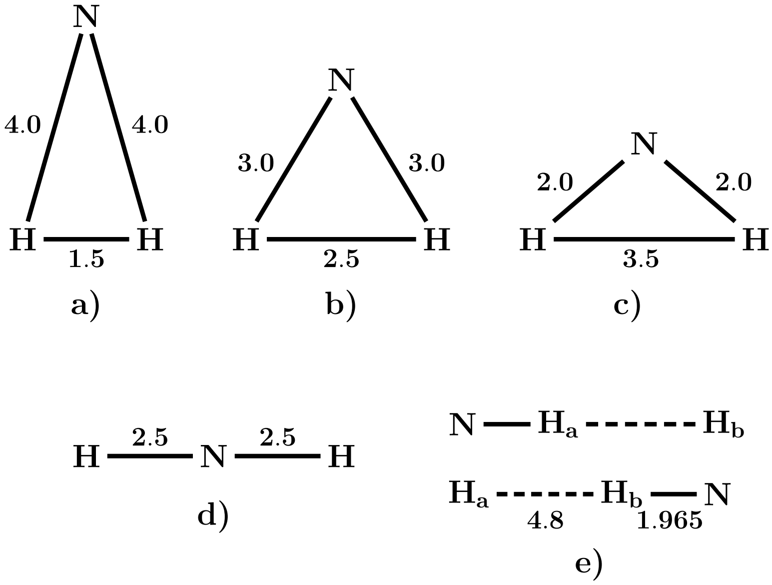

Figure 1. Reference geometries used to represent the three-body EHF energy. See the text for details (distances are in a_0).

the three-body EHF energy contribution. To represent the latter, we employ the following three-body distributed-polynomial[37] form:

$$V_{\mathrm{EHF}}^{(3)} = \sum_{j=1}^{6} P^{(j)}\left(Q_1, Q_2, Q_3\right) \prod_{i=1}^{3} \left\{1 - \tanh\left[\gamma_i^{(j)}\left(R_i - R_i^{(j),ref}\right)\right]\right\} \tag{11}$$

where the $P^{(j)}$s are polynomials up to six-order in the symmetry coordinates

$$\begin{pmatrix} Q_1 \\ Q_2 \\ Q_3 \end{pmatrix} = \begin{pmatrix} \sqrt{\frac{1}{3}} & \sqrt{\frac{1}{3}} & \sqrt{\frac{1}{3}} \\ 0 & \sqrt{\frac{1}{2}} & -\sqrt{\frac{1}{2}} \\ \sqrt{\frac{2}{3}} & -\sqrt{\frac{1}{6}} & -\sqrt{\frac{1}{6}} \end{pmatrix} \begin{pmatrix} R_1 - R_1^{(j),ref} \\ R_2 - R_2^{(j),ref} \\ R_3 - R_3^{(j),ref} \end{pmatrix} \tag{12}$$

The linear coefficients in every $P^{(j)}$ are deposited in Table 1 of the electronic supplementary information[†] (ESI) by specifying the associated monomial; the units are such that with the bond distances in a_0, the energy comes in E_h. In turn, the range-determining parameters and reference geometries are reported in Table 2 of ESI. These are also displayed in Figure 1, having been selected such

---

[†] http://dx.doi.org/10.1039/b505590c

Table 2. Stratified maximum and root-mean-square deviations (in kcal mol^{-1}) of DMBE potential energy surface.

Energy	N^a	max. dev.^{b}	rmsd	$N^c_{>\text{rmsd}}$
10	70	0.134	0.036	11
20	83	0.353	0.089	12
30	290	0.688	0.121	54
40	545	1.202	0.201	105
50	734	1.701	0.306	141
60	935	2.558	0.411	182
70	1044	2.558	0.466	207
80	1301	2.558	0.498	266
90	1438	2.558	0.526	301
100	1526	2.558	0.540	328
120	1639	2.558	0.554	353
140	1670	2.558	0.567	360
160	1689	2.558	0.573	366
180	1706	2.558	0.580	373
200	1717	2.558	0.588	375
250	1747	2.558	0.595	385
500	1790	2.558	0.601	398
1000	1804	2.558	0.602	402
1600	1812	2.558	0.604	405

[a] Number of points in the indicated energy range. [b] Maximum deviation up to the indicated energy range. [c] Number of points with an energy deviation larger than the rmsd.

as to cover the most important regions of configurational space.[37] Note that one such set of reference geometries is located at the NH + H channel in order to improve the fit at the van der Waals regions. In turn, the nonlinear range-determining parameters $\gamma_i^{(j)}$ have been optimized via a trial-and-error procedure such as to minimize the root-mean-squared-deviation (rmsd) while warranting the proper asymptotic behavior on dissociation. The complete set of parameters totals 207 linear coefficients, 18 nonlinear ones, and 18 reference bond distances. Table 2 shows the final stratified rmsd. As shown, the current DMBE form fits the regions of the potential energy surface up to the $\mathrm{N-H-H}$ transition state (30 kcal mol^{-1}, 290 *ab initio* points) with the high accuracy of rmsd = 0.12 kcal mol^{-1}. Of these points, only 18 % show a deviation larger than the corresponding rmsd value.

4 Major features of potential energy surface

Table 1 compares the Morse parameters of the NH and H_2 curves calculated at various levels of theory with the experimental results. Besides the calculations employed to explore the title potential energy surface,[12, 14, 15] we have tabulated some of the best predictions[34, 38] reported thus far. Clearly, electron correlation and enhancement of the basis set quality lead to sensible improvements of such attributes. For H_2, the *ab initio* calculations from the present work, and corresponding energies corrected by scaling of the external correlation, are seen to be in excellent agreement with the 'exact' result.[39] Moreover, the EHFACE2U curve[33] for H_2 is shown to reproduce the equilibrium bond distance and dissociation energy, with the vibrational frequency being only 8 cm^{-1} smaller than the experimental result. In turn, our predictions based on the MRCI-SEC calculations are seen to improve somewhat the Morse parameters when compared with the more recent[40, 41] (reliable) experimental values.

The major feature of the present quartet surface is the $N - H - H$ collinear transition state for reaction (1), which is highlighted in Figure 2. A comparison of the geometrical parameters and frequencies for this stationary point with previous results[12, 14, 15] is shown in Table 3. Note that we have calculated a grid of 78 *ab intio* points in its vicinity, with the DMBE form fitting such data with a rmsd of 1 cm^{-1}. We further observe that the geometrical attributes predicted from our DMBE form for the $N - H - H$ transition state follow the general pattern[28] of the MRCI calculations when increasing the basis set quality. As might be expected, the DMBE frequencies are shown to compare best with the UQCISD(TQ)/cc-pVTZ ones.

Also included in Table 3 are the attributes for the collinear ($D_{\infty h}$) transition state for reaction (2) which is shown in the symmetric stretching plot of the Figure given in the ESI. Here too, our results are found to be in satisfactory agreement with the most recent results by Pascual *et al.*,[15] Zhang *et al.*,[14] and Adam *et al.*[28]

Table 3. Comparison of the main stationary points in the DMBE potential energy surface.

	$R_{\mathrm{N-H}}/a_0$	$R_{\mathrm{H-H}}/a_0$	ω_1(as)/cm^{-1}	ω_2(ss)/cm^{-1}	ω_3(bend)/cm^{-1}
			N − H − H Saddle Point		
UMP2/6-311G**[a]	2.084	2.135	1748i	1592	824
UMP4/6-311G**[a]	2.099	2.248	1311i	1773	574,602
PES[b]	2.088	2.406	963i	1824	631
UQCISD(TQ)/cc-pVTZ[b]	2.096	2.290	1022i	1760	694
MRCI(SD)/cc-pVTZ[c]	2.099	2.289			
MRCI(SD)/cc-pVQZ[c]	2.105	2.253			
MRCI(SD)/cc-pV5Z[c]	2.109	2.238			
MRCI(SD)/cc-pV6Z[c]	2.110	2.234			
DMBE[d]	2.119	2.208	995i	1613	704
			H − N − H Saddle Point		
PES[b]	2.370	4.740	1589i	1822	1031
UQCISD(TQ)/cc-pVTZ[e]	2.381	4.762	2158i	1868	1076
MRCI(SD)/cc-pVQZ[c]	2.361	4.722			
DMBE[d]	2.367	4.734	2194i	2020	1116

[a] Ref. 12. [b] Ref. 15, potential energy surface based on Shepard's interpolation using MCQDPT2/$6-311$++G** calculations. [c] Ref. 28. [d] This work. [e] Ref. 14.

Table 4. Comparison of potential barriers and heat of reaction (in kcal mol^{-1}).

	Forward barrier		Reverse barrier		Heat of reaction	
	ΔV	$\Delta V^{a}_{\mathrm{ZPE}}$	ΔV	$\Delta V^{a}_{\mathrm{ZPE}}$	ΔV	$\Delta V^{a}_{\mathrm{ZPE}}$
			$\mathrm{N}\,(^4S) + \mathrm{H}_2\left(X^1\Sigma_g^+\right) \longleftrightarrow \mathrm{NH}\,(X^3\Sigma^-) + \mathrm{H}\,(^2S)$			
UMP4/6-311G**[b]			3.3	3.1	32.0	30.4
PES[c]	32.4	30.2	2.4	1.9	30.1	28.3
MP-SAC4[d]			1.9	1.7	30.2	28.6
QCISD(TQ)/cc-pVTZ[e]	31.3	29.6[f]	2.2	0.5[f]	29.2	29.1[f]
MRCI/cc-pVQZ[g]			2.2		27.3	
DMBE[h]	29.9	26.9	2.1	0.8	27.8	26.1
exp.[i]		25.1		0.3		24.3, 24.7[g]
exp.[j]		33±7				
			$\mathrm{H}\,(^2S) + \mathrm{NH}\,(X^3\Sigma^-) \longrightarrow \mathrm{NH}\,(X^3\Sigma^-) + \mathrm{H}\,(^2S)$			
PES[c]	22.1		22.1		0	0
UQCISD(TQ)/cc-pVTZ[c]	23.4		23.4		0	0
MRCI/cc-pVQZ[g]	22.6		22.6		0	0
DMBE[h]	22.7	22.5	22.7	22.5	0	0

[a] Zero-point corrected energies. [b] Ref. 12, single-point calculation at UMP2/6-311G** geometry. [c] Ref. 15, potential energy surface based on Shepard's interpolation using MCQDPT2/6-311++G** calculations. [d] Ref. 12, scaled correlation energy in UMP4/6-311G** calculations. [e] Ref. 14. [f] Ref. 14, calculated using the frequencies obtained at QCISD/cc-pVDZ level of theory. [g] Ref. 28. [h] This work. [i] Ref. 10, ± 35% in the k_1 measurement from 1950 to 2850 K. [j] Ref. 11, from 1600 to 2300 K.

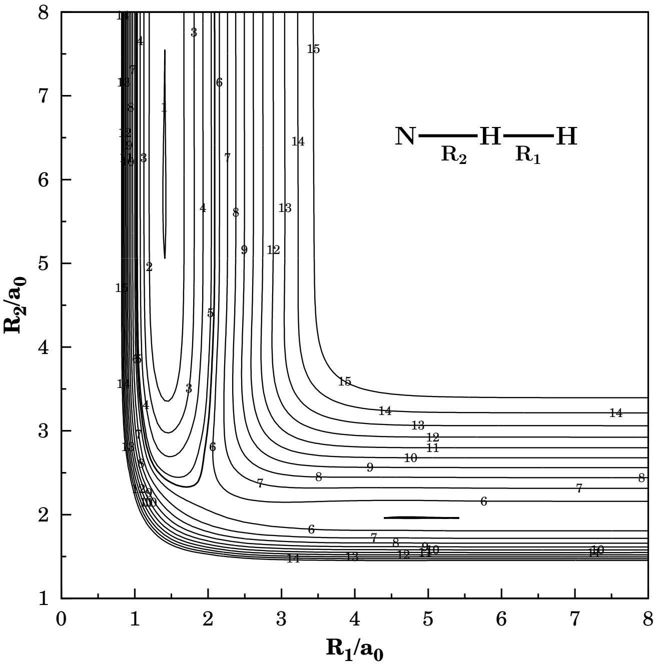

Figure 2. Contour plot for stretching of N − H − H in linear configurations. Contours equally spaced by $0.01\,E_\mathrm{h}$, starting at $-0.17455\,E_\mathrm{h}$. Note the van der Waals minimum shown by the closed contour in the N − H_2 channel.

A comparison of the energetics of the title reactions is shown in Table 4. For the forward reaction (1), our predicted barrier height including the zero-point energy correction is lower than previous theoretical estimates while falling in the interval proposed by Koshi *et al.*[11] It also lies closer to the most recent experimental values reported by Davidson and Hanson[10] than previous theoretical estimates. In turn, for the reverse reaction (1), our results compare well with the available experimental result.[10] Since our calculations together with those of Adam *et al.*[28] employ the highest level of theory used thus far, we may conclude that the agreement with experiment is good both for forward and reverse reactions occurring on the quartet state surface of NH_2.

It is well established from previous theoretical work that reaction (1) cannot proceed via insertion of N into H_2, instead a transition state is observed for the direct abstraction.[11, 12, 14, 15] This is clearly seen from Figure 3 which shows contour plots of the DMBE potential energy surface for the perpendicular approach of N to H_2. One observes a barrier height of 100 kcal mol^{-1}, thus precluding the

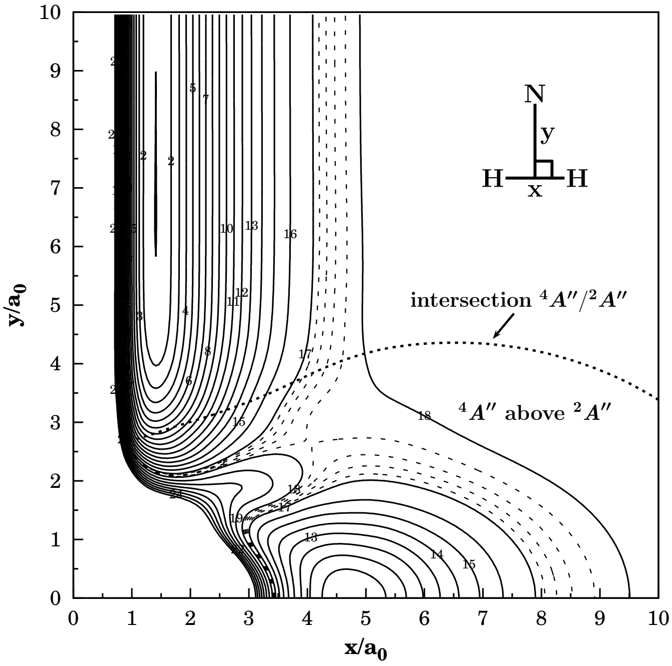

Figure 3. Contour plot for a C_{2v} insertion of N into H_2. Contours are equally spaced by $0.01\,E_\mathrm{h}$, starting at $-0.1745\,E_\mathrm{h}$.

occurrence of insertion. In fact, this saddle-point-like feature (it is not a true saddle-point in the full configuration space) is an artifact of the present single-sheeted representation, and should instead be a conical intersection of the two lowest $^4A''$ potential energy surfaces as illustrated in Figure 4. Of course, the possibility of a narrowly avoided intersection could not be discarded. To demonstrate that it is a true conical intersection, a topological proof has to be given. This is provided in Figure 5, which shows that the wave function changes sign when transported adiabatically along a closed path encircling the crossing point, as required by Longuet-Higgins' (Ref. 42, and references therein) sign-change theorems. Note that the involved sign change has been illustrated by plotting the leading component of the two CI vectors along such a path, following early *ab initio* work by Varandas, Tennyson and Murrell[43] for the LiNaK system.

Also indicated in Figure 3 is a cut for C_{2v} geometries of the $2D$ (allowed) crossing between the $^2A''$ and $^4A''$ potential energy surfaces as obtained by using the DMBE forms reported in the present work and Ref. 9. As expected, the asymptotic N + H_2 channel for the $^4A''$ potential energy surface lies below the

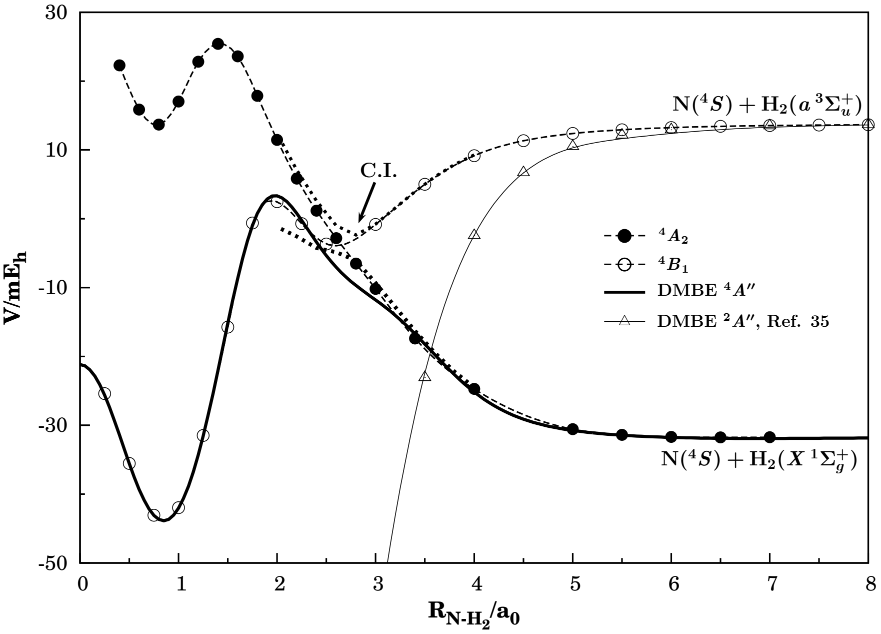

Figure 4. Cut of NH_2 quartet potential energy surfaces calculated at the MRCI/cc-pVQZ level along line with C_{2v} symmetry and H_2 fixed at $r = 3.5\,a_0$. The solid dots show the *ab initio* points for the $^4A_2$ potential energy surface, while the open circles indicate the $^4B_1$ ones. Note that the conical intersection (indicated by the arrow) becomes an avoided crossing as one moves away from C_{2v} symmetry, as shown by the dotted lines for a Jacobi angle of 89.5°. Also shown by the heavy solid line is the single-sheeted $^4A''$ DMBE potential energy surface, while the $^2A''$ DMBE one[9] is indicated by the thin solid line and up-triangles (these indicate actual *ab initio* MRCI/cc-pVQZ points[9]).

corresponding channel for the doublet state, since the former correlates with N in its ground quartet state. The reverse situation occurs for small $N - H_2$ separations (y values), which may be rationalized from the repulsive nature of the quartet state surface; note that the doublet surface shows a deep minimum for C_{2v} geometries associated to the stable NH_2 ($^2B_1$) species.

Figures 6 and 7 show contour plots for an atom moving around the remaining diatom which is fixed at the corresponding equilibrium bond distance. Given the repulsive character of the potential energy surface, the only minima that are observed refer to van der Waals structures. These have been modelled from about 100 *ab initio* points mapping the corresponding regions of configuration space, and fitted with a rmsd $\sim 2\,\mathrm{cm}^{-1}$. Such weak minima are found to occur at linear

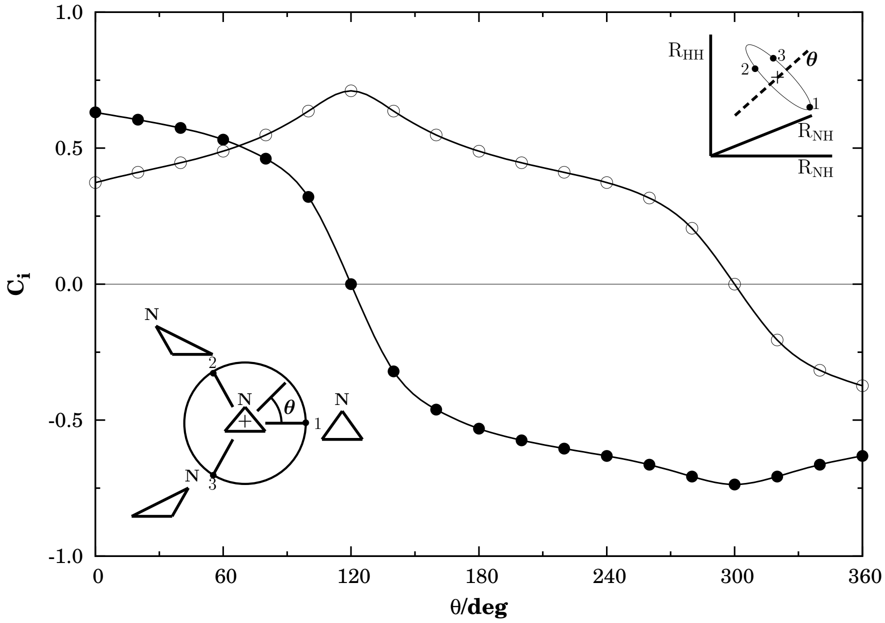

Figure 5. Sign change of the wave function as calculated at the FVCAS/cc-pVTZ level along a closed path encircling the conical intersection (C.I.). Only the variation of the coefficient associated with the dominant configuration is shown. The top right insert shows the coordinates employed, while the bottom left one indicates the geometries covered along such a path.

geometries, which is due to the polarizability component of the diatomics parallel to the molecular axis being larger than the perpendicular component. Table 5 gathers the calculated geometries, energies, and vibrational frequencies of such minima. The notable feature is perhaps the fact that the collinear NH$\cdots$H van der Waals well is somewhat deeper ($0.05\,\mathrm{kcal\,mol^{-1}} = 17\,\mathrm{cm^{-1}}$) than the H$\cdots$NH one (also collinear). This suggests that the attack of the hydrogen atom to NH is initially favored collinearly from the H end of the diatomic, as actually predicted from the dynamical correlation (dispersion energy) itself.

Finally, we show in Figure 8 the isotropic and leading anisotropic components of the $N - H_2$ interaction potential, two quantities of relevance in atom-diatom scattering.[9, 44] As shown in Figure 8, the interaction between N and H_2 for distances smaller than $5\,a_0$ is highly repulsive, with an abrupt increase of the potential energy as the two interacting species get into close contact. In turn, for long range distances, V_0 exhibits a negative (attractive) region where the van der

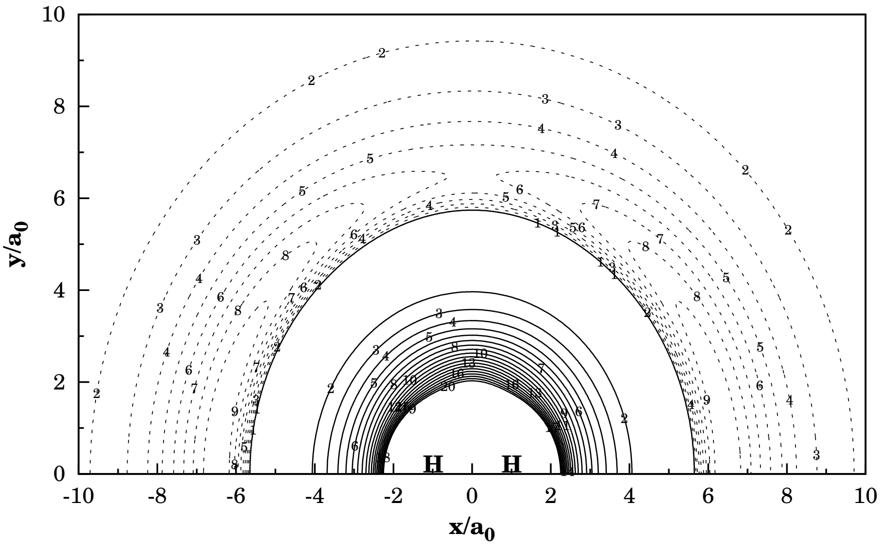

Figure 6. Contour plot for a N atom moving around H_2, which is frozen at the equilibrium geometry $R_{H_2} = 1.401\,a_0$ and lies along the X axis with the center of the bond fixed at the origin. Contours are equally spaced by $0.01\,E_h$, starting at $-0.174474\,E_h$. Shown in dash are contours equally spaced by $30\,\mu E_h$, starting at $-0.174475\,E_h$.

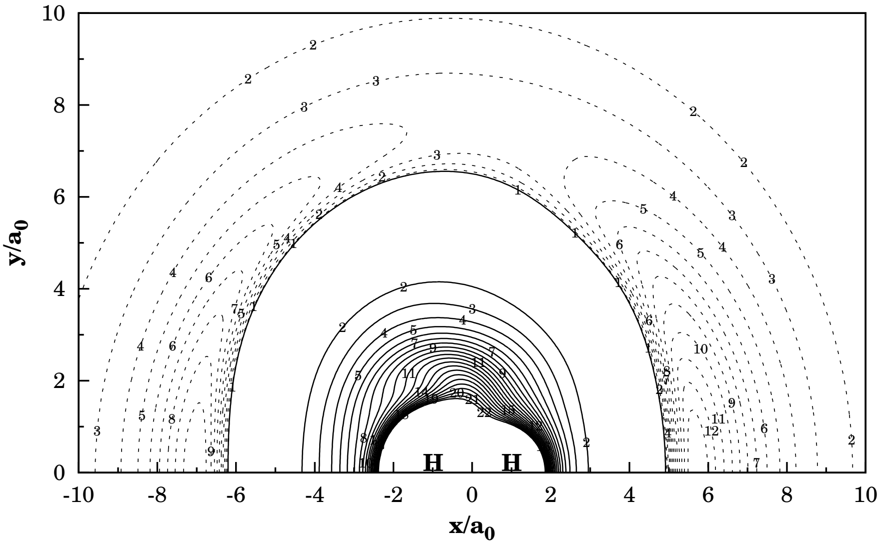

Figure 7. Contour plot for a H atom moving around NH frozen at $R_{NH} = 1.965\,a_0$, and lying along the X axis with the center of the bond fixed at the origin. Contour are equally spaced by $0.01\,E_h$, starting at $-0.1302\,E_h$. Shown in dash are contours equally spaced by $20\,\mu E_h$, starting at $-0.13021\,E_h$.

Table 5. Attributes of collinear van der Waals minima.

Property	$H-H\cdots N$	$N-H\cdots H$	$H\cdots N-H$
$R_{\mathrm{H-H}}/a_0$	1.402	4.705	7.993
$R_{\mathrm{N-H}}/a_0$	5.758	1.974	1.963
ΔV	-0.16^a	-0.17^b	-0.12^b
$\omega_1\,(\mathrm{intra})^c\,/\mathrm{cm}^{-1}$	4395	3244	3260
$\omega_2\,(\mathrm{inter})^d\,/\mathrm{cm}^{-1}$	80	159	103
$\omega_3\,(\mathrm{bend})^e\,/\mathrm{cm}^{-1}$	47	91	67

[a] Relative to the $N + H_2$ asymptote. [b] Relative to the $H + NH$ asymptote. [c] Associated to the intramolecular diatomic stretching frequency. [d] Associated to the intermolecular atom-diatom stretching frequency. [e] Associated to the bending (nearly free-rotor) motion.

Waals minimum is located. The negative sign of V_2 at such distances (see the insert in Figure 8) indicates that the van der Waals structure occurs at a collinear geometry, as expected from the larger polarizability of H_2 along the internuclear axis. Thus, the $N\cdots H_2$ C_{2v} insertion is favorable for atom-diatom distances of $3-5$ a_0, while a collinear arrangement is predicted from such a two-term Legendre analysis to be preferred for distances between 2.5 and $3\,a_0$ or larger than $5\,a_0$. In fact, although occurring for a somewhat larger $H-H$ separation, the transition state has a collinear geometry. In summary, the above behavior of V_0 and V_2 corroborates previous theoretical and experimental evidence by showing that the reaction (1) takes place via an abstraction mechanism rather than by insertion.

5 Concluding remarks

We have reported a single-sheeted DMBE potential energy surface for the quartet state of NH_2 based on a realistic representation of the long-range forces and a fit to accurate *ab initio* calculations. The various topographical features of the new potential energy surface have been carefully examined, and compared with previous analyzes reported for the title system. The inclusion of dynamical correlation and choice of a high quality basis set were found to play a very important role in the prediction of geometrical parameters, vibrational frequencies and energetics

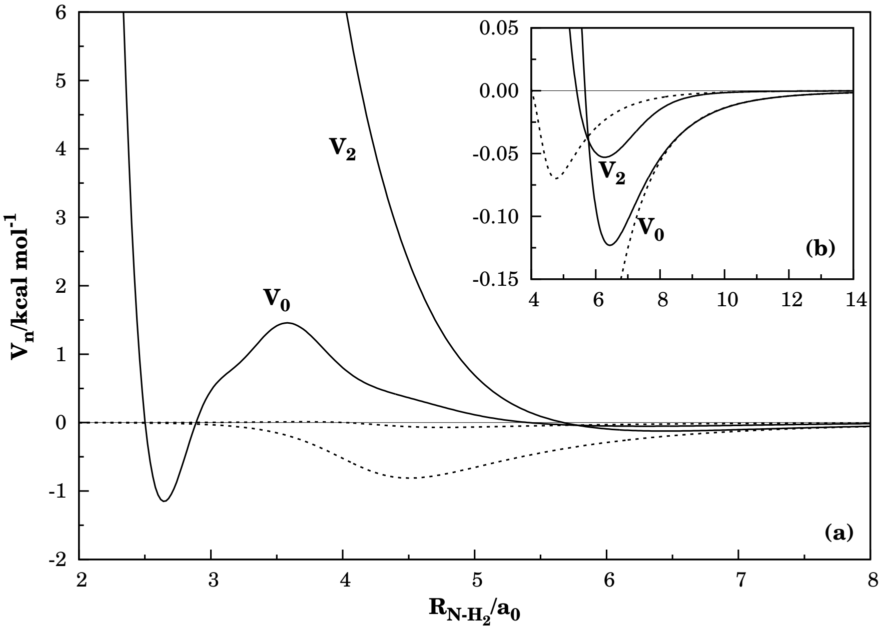

Figure 8. Isotropic (V_0) and leading anisotropic (V_2) components of the N-H_2 interaction potential, with the diatomic molecule fixed at the equilibrium geometry. Also indicated by the dotted lines are the corresponding dynamical correlation contributions. The insert shows a closeup for large distances to illustrate the effect of van der Waals forces.

of the title reactions. For both the forward and reverse reactions (1), the present calculations show good agreement with experiment and the best available theoretical estimates. The large barrier height found for the perpendicular approach of N to H_2 precludes any insertion mechanism for the title reaction, and result from the smoothing of a conical intersection arising between the two lowest $^4A''$ energy surfaces at C_{2v} geometries. Since the DMBE potential energy surface from the present work accurately fits high-level *ab initio* calculations, it is recommended both for dynamics studies of the title reactions and as a building block for the construction of the potential energy surfaces of larger H/N containing systems.

Acknowledgment

This work has the support of Fundação para a Ciência e Tecnologia, Portugal, under programmes POCTI and FEDER. The partial support of the European Community's Human Potential Programme under contract HPRN-CT-2002-00170 is also appreciated.

References

[1] H. Kobayashi, T. Takayanagi, K. Yokoyama, T. Sato, and S. Tsunashima, *J. Chem. Soc. Faraday Trans.*, 1995,**91**, 3771.

[2] H. Umemoto and K. Matsumoto, *J. Chem. Phys.*, 1996, **104**, 9640.

[3] T. Takayanagui, H. Kobayashi, and S. Tsunashima, *J. Chem. Soc. Faraday Trans.*, 1996, **92**, 1311.

[4] H. Umemoto, T. Asai, and Y. Kimura, *J. Chem. Phys.*, 1997, **106**, 4985.

[5] H. Kobayashi, T. Takayanagui, and S. Tsunashima, *Chem. Phys. Lett.*, 1997, **277**, 20.

[6] M. Alagia, N. Balucani, L. Cartechini, P. Cachavecchia, G. G. Volpi, L. A. Pederson, G. C. Schatz, G. Lendvay, L. B. Harding, T. Hollebeek, T.-S. Ho, and H. Rabitz, *J. Chem. Phys.*, 1999, **110**, 8857.

[7] L. A. Pederson, G. C. Schatz, T. Ho, T. Hollebeek, H. Rabitz, and L. B. Harding, *J. Chem. Phys.*, 1999, **110**, 9091.

[8] L. A. Pederson, G. Schatz, T. Hollebeek, T.-S. Ho, H. Rabitz, and L. B. Harding, *J. Phys. Chem. A*, 2000, **104**, 2301.

[9] A. J. C. Varandas and L. Poveda, *Theor. Chem. Acc.*, in press.

[10] D. F. Davidson and R. K. Hanson, Int. *J. Chem. Kin.*, 1990, **22**, 843.

[11] M. Koshi, M. Yoshimura, K. Fukuda, H. Matsui, K. Saito, M. Watanabe, A. Imamura, and C. Chen, *J. Chem. Phys.*, 1990, **93**, 8703.

[12] Z.-F. Xu, D.-C. Fang, and X.-Y. Fu, *J. Phys. Chem. A*, 1997, **101**, 4432.

[13] C. Ottinger, M. Brozis, and A. Kowalski, *Chem. Phys. Lett.*, 1999, **315**, 355.

[14] S. Zhang and T. N. Truong, *J. Chem. Phys.*, 2000, **113**, 6149.

[15] R. Pascual, G. C. Schatz, G. Lendvay, and D. Troya, *J. Phys. Chem. A*, 2002 **106**, 4125.

[16] M. J. T. Jordan, K. C. Thompson, and M. A. Collins, *J. Chem. Phys.*, 1995, **102**, 5647.

[17] K. C. Thompson and M. A. Collins, *J. Chem. Soc. Faraday Trans.*, 1997, **93**, 871.

[18] K. C. Thompson, M. J. T. Jordan, and M. A. Collins, *J. Chem. Phys.*, 1998, **108**, 8302.

[19] R. P. A. Bettens and M. A. Collins, *J. Chem. Phys.*, 1999, **111**, 816.

[20] A. J. C. Varandas, *J. Mol. Struct. Theochem.*, 1985, **120**, 401.

[21] A. J. C. Varandas, *Adv. Chem. Phys.*, 1988, **74**, 255.

[22] A. J. C. Varandas, *Chem. Phys. Lett.*, 1992, **194**, 333.

[23] A. J. C. Varandas, in *Lecture Notes in Chemistry*, ed. A. Laganá and A. Riganelli, Springer, Berlin, 2000, vol. 75, pp. 33.

[24] A. J. C. Varandas, *Modeling and interpolation of global multi-sheeted potential energy surfaces*, World Scientific Publishing, 2004, ch. 5, p. 91.

[25] T. H. Dunning, *J. Chem. Phys.*, 1989, **90**, 1007.

[26] R. Kendall, T. Dunning Jr., and R. Harrison, *J. Chem. Phys.*, 1992, **96**, 6769.

[27] A. J. C. Varandas, *J. Chem. Phys.*, 1989, **90**, 4379.

[28] L. Adam, W. Hack, H. Zhu, Z.-W. Qu, and R. Schinke, *J. Chem. Phys.*, 2005, **114301**, 122.

[29] H.-J. Werner and P. J. Knowles, *J. Chem. Phys.*, 1988, **89**, 5803.

[30] P. J. Knowles and H.-J. Werner, *Chem. Phys. Lett.*, 1985, **115**, 259.

[31] H.-J. Werner and P. J. Knowles, MOLPRO is a package of *ab initio* programs written by H.-J. Werner, P. J. Knowles, with contributions from J. Almlöf, R. D. Amos, M. J. O. Deegan, S. T. Elbert, C. Hampel, W. Meyer, K. A. Peterson, R. Pitzer, A. J. Stone, P. R. Taylor, R. Lindh, 1998.

[32] A. J. C. Varandas and J. D. Silva, *J. Chem. Soc. Faraday Trans.*, 1992, **88**, 941.

[33] A. J. C. Varandas, J. Chem. Phys. **105**, 3524 (1996).

[34] J. R. Stallcop, C. W. Bauschlicher, H. Partridge, S. R. Langhoff, and E. Levin, *J. Chem. Phys.*, 1992, **97**, 5579.

[35] P. J. S. B. Caridade and A. J. C. Varandas, unpublished work.

[36] A. J. C. Varandas and S. P. J. Rodrigues, *J. Chem. Phys.*, in press.

[37] E. Martínez-Nuñez and A. J. C. Varandas, *J. Phys. Chem.*, 2001, **105**, 5923.

[38] C. W. Bauschlicher, Jr. and S. R. Langhoff, *Chem. Phys. Lett.*, 1987, **135**, 67.

[39] W. Kolos and L. Wolniewicz, *J. Chem. Phys.*, 1965, **43**, 2429.

[40] K. P. Huber and G. Herzberg, *Molecular Spectra and Molecular Structure IV. Constants of Diatomic Molecules*, Van Nostrand, New York, 1979.

[41] H. Sakai, P. Hansen, M. Splin, and R. Johansson, *Appl. Opt.*, 1982, **21**, 228.

[42] H. C. Longuet-Higgins, *Proc. R. Soc. Ser. A*, 1975, **344**, 147.

[43] A. J. C. Varandas, J. Tennyson, and J. N. Murrell, *Chem. Phys. Lett.*, 1979, **61**, 431.

[44] A. J. C. Varandas, *J. Chem. Phys.*, 1979, **70**, 3786.

[45] J. M. Lentz, *J. Quant. Spectrosc. Radiat. Transfer.*, 1973, **13**, 297.

Chapter 6

Ab initio study towards a DMBE-PES for diimide

Chem. Phys. Lett. **424**, 46–53 (2006).

Accurate MRCI study of ground-state N_2H_2 potential energy surface

M. Biczysko, L.A. Poveda and A.J.C. Varandas

Departamento de Química, Universidade de Coimbra
3004-535 Coimbra Codex, Portugal.

(Received: January 26, 2006; In final form: April 3, 2006)

Abstract

Extensive *ab initio* calculations have been performed to determine the energy, geometry and vibrational frequencies of all stationary points of the N_2H_2 ground-state potential-energy surface. The geometries of *trans*-, *cis*- and *iso*- minima as well as transition states are reported at the MCSCF/aug-cc-pVQZ level, while the relative energetics is established by single point MRCI/aug-cc-pVQZ calculations including the Davidson size-consistency correction. The data is useful for modeling a single-sheeted global potential energy surface for the title system.

1 Introduction

It is well known that gas phase hydrogenation of nitrogen can occur without a catalyst only under extreme conditions due to the high energy barriers involved, although a detailed reaction mechanism has not been established yet. It is also accepted [1] that the addition of the first hydrogen molecule to nitrogen is the rate-determining step of the nitrogen hydrogenation process leading to ammonia. Knowledge of an accurate global potential energy surface for N_2H_2 is therefore a key step toward the understanding of the elementary reactions involved in such processes.

There have been several theoretical [1–13] and experimental [14–19] studies of the title system (a more complete list of earlier theoretical and experimental work is given in Refs. 2, 3). Some of these studies focused on the determination of accurate geometries, frequencies and relative stabilities of three local minima: *trans*-, *cis*-, and *iso*-N_2H_2 [3, 7, 10, 11, 14–19]. Moreover, there has been considerable theoretical work [1, 2, 4–6, 8, 9, 12, 13] on the determination of the barriers involved in the diimide isomerization or formation processes, often for testing the accuracy of theoretical methods that are used to study chemical reactions [4, 6, 12, 13]. All published work agrees on the structures of the above minima (*trans*, *cis*, and *iso*) for N_2H_2, although the agreement for transition states (TSs) stands only for the TS associated to the *trans*-*iso* conversion. For the other TSs, discrepancies exist between the various theoretical results. In particular, for the *trans*-*cis* conversion, some papers predict both rotational and inversional reaction paths [2, 8, 9] while others infer it to occur by inversion [6, 12, 13] or rotation [1] only.

Regarding previous work on the potential energy surface of N_2H_2 (considering also reaction paths for diazene formation), the most detailed studies have been performed by Jensen *et al.* [2] at the complete-active-space self-consistent field (CASSCF) level using a basis set of double-ζ quality and more recently by Hwang and Mebel [1] using G2M(MP2)//MP2/6-31G** theory. The CASSCF calculations [2] predict three more transition states on the N_2H_2 potential energy surface, in addition to the *trans*-*cis* and *trans*-*iso* isomerization processes. They are associated to the dissociative (N_2H + H) transition state, a C_{2v} TS where both NH bonds are elongated in comparison to the *cis*- minimum (obtained by walking along the symmetric stretching or bending coordinates from *cis*-N_2H_2), and a TS for N_2H_2 (isodiazene) formation from $N_2 + H_2$. On the other hand, the G2M(MP2)//MP2/6-31G** calculations of Hwang and Mebel [1] predict two transition states for diazene formation from hydrogen and nitrogen molecules leading to *cis*- and *iso*-N_2H_2, but only one (rotational) reaction path for *trans-cis* isomerization. Instead of the inversional path (reported by other studies performed at G2 level [6, 12]), a transition state corresponding to *trans*-N_2H_2 isomerization by in-plane scrambling of the hydrogen atoms is predicted. Moreover, there are significant discrepancies in the relative energies of several stationary points throughout the literature showing that the potential energy diagram and involved reaction pathways on the ground state potential energy surface of N_2H_2 are far from well established. This has been a major motivation for carrying out the systematic high level *ab initio* studies reported in the present work, which employ multireference approaches with extensive basis sets. In fact, our calculations provide also an accurate ground for ongoing work on modeling a global single-sheeted potential energy surface for the title system using double many-body expansion (DMBE; Ref. 20, and references therein) theory.

The paper is organized as follows. Section 2 describes the *ab initio* calculations carried out in the present work, while the results are discussed in section 3. The concluding remarks are in section 4.

2 *Ab initio* calculations

All structures have been optimized at the multiconfiguration self consistent field (MCSCF) [21] level using the full valence complete active space (FVCAS) [22] wave function as the reference. This involves 12 correlated electrons distributed over 10 active orbitals. For the basis set we have selected the aug-cc-pVXZ (X=D,T,Q) of Dunning [23, 24] (AVXZ) in order to establish an adequate level of theory for modeling the title potential energy surface. Geometry optimizations have been followed by harmonic frequency calculations to confirm the nature of the stationary points (minima and transition states of index one, *i.e.*, having just one imaginary frequency). Reaction paths from all TSs have also been determined by using the Quadratic Steepest Descent (QSD) reaction path following procedure [25]. For all stationary points, single point calculations at the multireference configuration interaction (MRCI) [26] level have been performed in order to obtain accurate relative energies. Moreover, the Davidson [27] (+Q) and Pople [28] (P) size-consistency corrections have been applied. The energies have been subsequently corrected for zero-point energy (ZPE) based on MCSCF frequency calculations. All *ab initio* calculations employed the MOLPRO [29] package.

3 Results and discussion

The geometries and harmonic frequencies of the *trans*-, *cis*-, and *iso*-N_2H_2 minima calculated at the MCSCF/aug-cc-pVXZ (X=D,T,Q) levels are collected in Table 1. Also given in this Table are the energies obtained from single point MRCI/aug-cc-pVXZ energy calculations including the Davidson size-consistency and zero-point energy corrections (from harmonic calculations at the corresponding MCSCF/AVXZ level). For all minima, there are several theoretical [1–3] and a few experimental [14, 16, 17] results that may serve for comparison purposes, and hence for establishing the level of theory that is required for subsequent studies of the N_2H_2 potential energy surface. As the most accurate theoretical results reported thus far stand the benchmark calculations of Martin and Taylor [3] using the coupled-cluster, CCSD(T), method with extrapolation to the basis set limit and inclusion of inner shell correlation effects and anharmonicity in the zero-point energy. We observe an important overall improvement in the calculated optimized geometries when going from AVDZ to AVTZ, with a further improvement of the basis set to AVQZ quality giving an even better agreement with the reference data [3]. For bond lengths the associated average discrepancies are 0.034, 0.022 and 0.021 a_0 for the AVDZ, AVTZ, and AVQZ basis sets (respectively), while the corresponding maximum deviations are 0.048, 0.034, and 0.033 a_0. For the angles, the average discrepancy varies from more then 0.5° for the AVDZ basis set to 0.41° for AVTZ, and 0.36° for AVQZ. No significant improvement is observed for the frequencies. However, the maximum discrepancies do not exceed 150 cm^{-1}, and hence may be considered relatively small, especially having in mind that the effect of anharmonicity has note been included in the present work.

In fact, the most important sign of having attained good accuracy refers to the energetics. Indeed, the MRCI+Q/AVTZ and MRCI+Q/AVQZ corrected zero-point energies (ZPEs) from this work are shown to differ by less than $0.2\,\mathrm{kcal\,mol^{-1}}$ from the best theoretical estimates [3], with slightly better agreement in case of the AVQZ basis set (average errors of 0.1 and $0.08\,\mathrm{kcal\,mol^{-1}}$ for AVTZ and AVQZ basis sets, respectively). We have also extrapolated the dynamical correlation energy to the basis set limit [30], but observed no significant improvement in the relative energetics of the three minima. This seems to indicate that the energy calculations here reported are fairly well converged at the MRCI+Q/aug-cc-pVQZ level.

The accuracy of the calculations of the present work may further be assessed by comparing with the results of Hwang and Mebel [1] and Jensen *et al.* [2] which represent the most extensive studies of stationary points on the global potential energy surface of N_2H_2 carried out thus far. In both studies [1, 2] the bond lengths are overestimated by up to $0.04\,a_0$, and the frequencies by up to more than $300\,\mathrm{cm^{-1}}$. As for the relative energies, the agreement with the best reported estimate [3] is of $0.5\,\mathrm{kcal\,mol^{-1}}$ in the case of Hwang and Mebel [1], while the relative energies of Jensen *et al.* [2] for the *cis* and *iso* isomers are found to be overestimated by $1.47\,\mathrm{kcal\,mol^{-1}}$ and $10.47\,\mathrm{kcal\,mol^{-1}}$, respectively. In turn, a comparison of the local minima of diazene reported in the present work with those from previous studies for the title system [1, 2] including the best theoretical estimates of Martin and Taylor [3] suggest that they may stand as accuracy tests for subsequent studies of other stationary points on the N_2H_2 potential energy surface. Thus, our work suggests that geometries and vibrational frequencies of transition states from MCSCF/aug-cc-pVQZ calculations, with the energetics determined from single-point computations at the MRCI+Q/aug-cc-pVQZ level corrected for ZPE, provide the best theoretical estimates reported thus far for the N_2H_2 system.

For the TS calculations, we have considered all structures reported in literature as starting points for the symmetry unconstrained geometry optimizations at the MCSCF/AVQZ level. In the case of the TS3 of Jensen *et al.* [2] (C_{2v} structure with both NH bonds elongated in comparison to the *cis*- minimum),

Table 1. Properties of local minima for N_2H_2.

Feature	Property	MRCI+Q/AVDZ// MCSCF/AVDZ^a	MRCI+Q/AVTZ// MCSCF/AVTZ^a	MRCI+Q/AVQZ// MCSCF/AVQZ^a	G2M(MP2)// //MP2/6-31G*^{b}	CASSCF^c	CCSD(T)/VQZ^d	exp.
Global minimum	R_{NN}/a_0	2.3897	2.3767	2.3741	2.3943	2.3924	2.3561	2.3565^e
trans N_2H_2	R_{NH}/a_0	1.9821	1.9702	1.9688	1.9502	1.9748	1.9428	1.9464^e
	$\angle$HNN/°	105.6	105.9	106.0	105.1	104.8	106.2	106.3^e
	ω_1(N-N)/cm^{-1}	1540	1527	1530	1525	1526	1528	1529^f
	ω_2(N-H)$_{sym}$/cm^{-1}	3122	3124	3131	3382	3154	3051	3128^f
	ω_3(N-H)$_{asym}$/cm^{-1}	3152	3158	3164	3353	3197	3133	3120^f, 3120.29^g
	ω_4(N-N-H)$_{sym}$/cm^{-1}	1616	1617	1619	1628	1663	1578	1582^f
	ω_5(N-N-H)$_{asym}$/cm^{-1}	1351	1354	1355	1360	1374	1317	1322^f, 1316.41^g
	ω_6(tors)/cm^{-1}	1314	1321	1323	1349	1351	1294	1286$^{f)}$,1288.65^g
	ΔE/kcal mol^{-1}	0.0	0.0	0.0	0.0	0.0	0.0	
cis N_2H_2	R_{NN}/a_0	2.3804	2.3732	2.3710	2.3829	2.3924	2.3538	
	R_{NH}/a_0	2.0006	1.9807	1.9791	1.9596	1.9748	1.9523	
	$\angle$HNN/°	111.5	111.6	111.7	111.9	104.8	111.9	
	ω_1(N-N)/cm^{-1}	1571	1545	1548	1562	1535	1548	1558^h
	ω_2(N-H)$_{sym}$/cm^{-1}	3035	3088	3092	3306	3144	3003	2966^h
	ω_3(N-H)$_{asym}$/cm^{-1}	2940	2997	3002	3225	3074	2987	2884^h
	ω_4(N-N-H)$_{sym}$/cm^{-1}	1368	1358	1359	1373	1416	1335	1390^h
	ω_5(N-N-H)$_{asym}$/cm^{-1}	1573	1579	1580	1567	1616	1521	1439^h
	ω_6(tors)/cm^{-1}	1254	1255	1258	1287	1267	1232	1259^h
	ΔE/kcal mol^{-1}	5.35	5.09	5.05	4.81	6.68	5.21	
iso N_2H_2	R_{NN}/a_0	2.3140	2.2991	2.2968	2.3092	2.3130	2.3002	
	R_{NH}/a_0	1.9973	1.9886	1.9875	1.9634	1.9615	1.9544	
	$\angle$HNN/°	124.1	124.2	124.2	124.1	124.4	123.5	
	ω_1(N-N)/cm^{-1}	1603	1588	1590	1664	1611	1560	1574^i
	ω_2(N-H)$_{sym}$/cm^{-1}	2916	2906	2910	3173	2868	2770	2805^i
	ω_3(N-H)$_{asym}$/cm^{-1}	2943	2944	2946	3211	3253	2867	2862$^{i)}$
	ω_4(sciss)/cm^{-1}	1727	1737	1739	1783	1814	1665	1645^i
	ω_5(rock)/cm^{-1}	1330	1341	1346	1364	1375	1293	1288^i
	ω_6(tors)/cm^{-1}	1012	1014	1018	1060	1039	991	1003^i
	ΔE/kcal mol^{-1}	25.23	24.31	24.04	24.65	34.59	24.12	

[a] Energies from this work calculated at MRCI+Q/aug-cc-pVXZ level for MCSCF/aug-cc-pVXZ optimized structures that have been corrected for ZPE using MCSCF/aug-cc-pVXZ frequency calculations; see text. [b] G2M(MP2) energies for MP2/6-31G** optimized structures from Hwang and Mebel [1]. [c] Energies corrected for ZPE from Jensen *et al.* [2]. [d] Best estimate at 0K accounting for inner-shell correlation and anharmonic ZPE corrections from Martin and Taylor [3]. [e] Ref. 14. [f] Ref. 16. [g] Ref. 15. [h] Estimates from Creig and Levin [16] based on approximate force field of *trans*-N_2H_2. [i] Ref. 17.

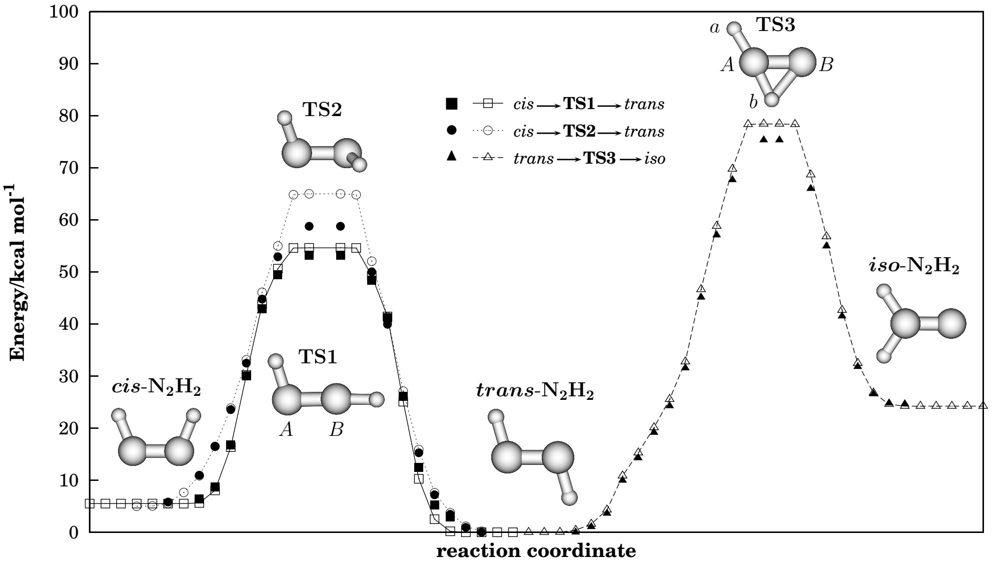

Figure 1. Reaction path following calculations performed at MCSCF/aug-cc-pVQZ level for the isomerisations between local minima: squares and solid line *trans-cis* path through inversional (TS1) transition state; circles and dash-dot line, *trans-cis* path through rotational (TS2) transition state; triangles and dashed line, *trans-iso* path. Selected points on reaction paths calculated at MRCI+Q/aug-cc-pVQZ level are shown by solid symbols. When appropriate in this and subsequent figures, the nitrogen (hydrogen) atoms are distinguished by using the labels *A* and *B* (*a* and *b*). Energies are in kcal mol^{-1} relative to the *trans*-N_2H_2 minimum.

it leads to the dissociative (N_2H + H) transition state TS6. When starting at the TSt-t of Hwang and Mebel [1] (C_{2h} structure with both NNH angles close to 180°), the transition state search carried out in the present work terminated at TS1. It should be added though that the actual structure has not been reported in Ref. 1. Moreover, for all transition states, reaction path following calculations using the QSD [25] scheme have been performed at the MCSCF/aug-cc-pVQZ level, which were followed by single point MRCI+Q/aug-cc-pVQZ energy calculations at selected reaction steps. The reaction paths connecting *trans*-N_2H_2 to the *cis* and *iso* isomers are shown in Figure 1, while the energy profiles for the N_2H_2 formation from molecular hydrogen and nitrogen are shown in Figure 2. In turn, Figure 3 relates to the dissociation-recombinations reaction paths via N_2H + H (TS6). The potential energy scan for dissociation of a hydrogen atom from *trans*-

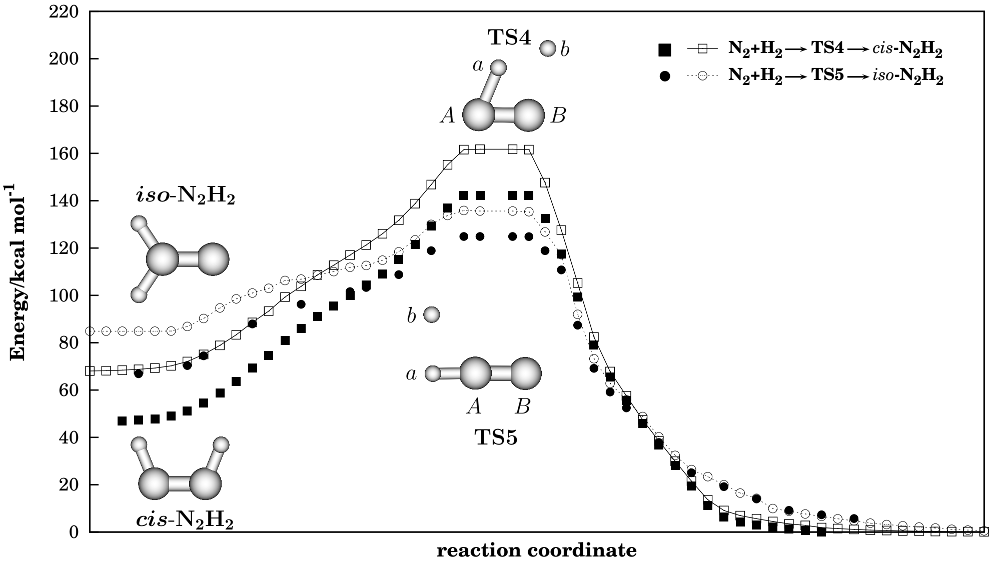

Figure 2. Reaction paths for formation of N_2H_2 from molecular nitrogen and hydrogen. TS4 and TS5 are transition states for the parallel (squares and solid line) and perpendicular (circles and dashed line) approaches of N_2 and H_2, respectively. Reaction path following calculations have been performed at MCSCF/aug-cc-pVQZ level and followed by MRCI+Q/aug-cc-pVQZ calculations for selected points (solid symbols). Energies are in kcal mol^{-1} relative to the N_2+H_2 asymptote.

, *cis*-, and *iso*-N_2H_2 has been calculated at the MRCI+Q/aug-cc-pVQZ level of theory. These figures collect all the structures of minima and transition states of N_2H_2 found in the present study, while Table 2 compares the transition states geometries, frequencies and relative energies with data from other theoretical works [1, 2, 12, 13].

There has been a dispute in the literature on whether the *trans*-*cis* isomerization occurs via one or two transition states connecting these structures (inversional-TS1 or rotational-TS2) or rather that all rearrangements within the N_2H_2 system evolve through the dissociation-recombination pathway involving TS6. The first theoretical works (see Ref. 9) predicted the inversional mechanism to be favored over the rotational one, with the possibility of dissociative rearrangement having been excluded [9] based on the activation energies of related processes. More recent calculations using CASSCF [2] and G2M [1, 6, 12] methods predict very similar stabilities for TS1 and TS2, with TS2 being favored

Table 2. Properties of transition states of N_2H_2 system.

Feature/ Property	MRCI+Q/AVQZ// //MCSCF/AVQZ[a]	G2M(MP2)// //MP2/6-31G*[b]	CASSCF[c]	G2M(MP2)// //DFT/DZVP[d]
TS1				
R_{NN}/a_0	2.3299		2.3622	2.3300
$R_{\mathrm{N}_A\mathrm{H}_a}/a_0$	2.0155		2.0126	2.0390
$R_{\mathrm{N}_B\mathrm{H}_b}/a_0$	1.8514		1.8708	1.9011
$\angle \mathrm{H}_a\mathrm{N}_A\mathrm{N}_B/^\circ$	110.5		108.1	109.5
$\angle \mathrm{H}_b\mathrm{N}_B\mathrm{N}_A/^\circ$	178.4		178.9	177.4
$\Delta E/\mathrm{kcal\,mol}^{-1}$	51.07		63.35	49.53
Frequencies/cm^{-1}	$1720i$		$2075i$	$1509i$
	678		684	682
	1513		1536	1448
	1626		1614	1691
	2733		2876	2701
	4053		3957	3812
TS2				
R_{NN}/a_0	2.5546	2.4812	2.6645	
R_{NH}/a_0	1.9854	1.9521	1.9974	
$\angle \mathrm{HNN}/^\circ$	107.5	110.0	103.4	
$\theta/^\circ$	91.4	90.0	89.9	
$\Delta E/\mathrm{kcal\,mol}^{-1}$	54.96	48.86	62.93	
Frequencies/cm^{-1}	$4802i$	$1328i$	$3323i$	
	961	964	923	
	1192	1117	1257	
	1218	1306	1279	
	2980	3341	2991	
	2995	3357	3001	
TS3				
R_{NN}/a_0	2.4399	2.4359	2.4548	2.4207
$R_{\mathrm{N}_A\mathrm{H}_a}/a_0$	2.0134	1.9804	2.0144	2.0409
$R_{\mathrm{N}_A\mathrm{H}_b}/a_0$	2.1091	2.0541	2.0598	2.1203
$R_{\mathrm{N}_B\mathrm{H}_b}/a_0$	2.5682	2.5738	2.5833	2.5795
$\angle \mathrm{H}_a\mathrm{N}_A\mathrm{N}_B/^\circ$	121.3	120.0	122.1	121.1
$\Delta E/\mathrm{kcal\,mol}^{-1}$	70.87	71.07	81.76	70.26
Frequencies/cm^{-1}	$2302i$	$2423i$	$2186i$	$1953i$
	559	636	574	652
	1325	1359	1330	1319
	1467	1541	1513	1503
	2594	2918	2625	2605
	2888	3203	3082	2882

Table 2. Continue

TS4			
R_{NN}/a_0	2.2852	2.3017	
$R_{\mathrm{N}_A\mathrm{H}_a}/a_0$	2.3345	2.3395	
$R_{\mathrm{N}_B\mathrm{H}_b}/a_0$	3.2210	2.9234	
R_{HH}/a_0	2.5748	2.3622	
$\angle\mathrm{H}_a\mathrm{N}_A\mathrm{N}_B/^\circ$	63.5	61.2	
$\Delta E/\mathrm{kcal\,mol}^{-1}$	92.94	95.55	
Frequencies/cm^{-1}	$3363i$	$3234i$	
	756	850	
	859	1041	
	941	1303	
	1592	1743	
	2217	2447	
TS5			
R_{NN}/a_0	2.1607	2.1845	2.1807
$R_{\mathrm{N}_A\mathrm{H}_a}/a_0$	1.9180	1.9067	1.8765
$R_{\mathrm{N}_A\mathrm{H}_b}/a_0$	3.4085	3.3562	3.3996
R_{HH}/a_0	2.9604	2.8818	2.9298
$\angle\mathrm{H}_b\mathrm{N}_A\mathrm{N}_B/^\circ$	123.9	126.1	124.6
$\angle\mathrm{H}_a\mathrm{N}_A\mathrm{N}_B/^\circ$	176.1	174.9	176
$\Delta E/\mathrm{kcal\,mol}^{-1}$	74.15	76.32	78.77
Frequencies/cm^{-1}	$2024i$	$2001i$	$2387i$
	716	728	713
	720	792	742
	1216	1261	1240
	1827	2136	1892
	3520	3725	3831
$\mathrm{N_2H + H}$ (TS6)			
R_{NN}/a_0	2.2313	2.1751	2.2469
R_{NH}/a_0	2.0395	1.9842	2.0674
$angle\mathrm{HNN}/^\circ$	116.0	120.9	112.4
$\Delta E/\mathrm{kcal\,mol}^{-1}$	61.22	63.6	54.2
Frequencies/cm^{-1}	1121	1050	1141
	1714	2895	1614
	2425	3015	2247

[a] This work. Energies obtained from single point MRCI+Q/aug-cc-pVQZ calculations for MCSCF/aug-cc-pVQZ optimized structures, and corrected for ZPE based on MCSCF/aug-cc-pVQZ frequency calculations; see text. [b] G2M(MP2) energies for MP2/6-31G** optimized structures from Hwang and Mebel [1]. [c] Energies corrected for ZPE from Jensen *et al.* [2]. [d] Structures calculated [13] using density functional theory (DFT), and energies from G2M(MP2) theory [12].

by less than 1 kcal mol^{-1}. Moreover, CASSCF calculations [2] predict TS6 to be significantly lower in energy than both TS1 and TS2, but recombination after dissociation has been ruled out due to the instability of the N_2H radical. In this study, we have confirmed that multireference SCF calculations (see Table 3) predict TS6 to lie lowest in energy. However, when MRCI calculations are performed, TS6 is encountered to lie above both TS1 and TS2 by 10.15 kcal mol^{-1} and 6.25 kcal mol^{-1}, respectively. Moreover, our calculations predict the inversional barrier to be slightly lower than the rotational one, although their relative positions calculated at MRCI level differ by less than 5 kcal mol^{-1}. Note that TS2 has a high imaginary frequency, which may enhance the possibility of reaction via a tunneling mechanism through the rotational path. Thus, our results suggest that the dissociative reaction path can be ruled out for the *trans*-*cis* isomerization. Yet, because the N_2H radical has been found to be a metastable species [31–33], TS6 can be relevant in other recombination processes of N_2H_2.

For the *trans*-*iso* isomerization, all theoretical studies [1, 2, 6, 9, 12] reported only one transition state, namely TS3. Moreover, its energy has been predicted to be about 70 kcal mol^{-1} relative to the *trans* isomer, thus significantly above TS6. As a result, such an isomerization may most likely occur via a dissociation-recombination pathway.

For TS4 and TS5, it has been found that both structures are transition states of index one for the formation of N_2H_2 from molecular nitrogen and hydrogen. The perpendicular approach leading to *iso*-N_2H_2 via TS5 is favorable in comparison to the parallel approach leading to *cis*-N_2H_2 via TS4. However, in both cases barriers of more than 120 kcal mol^{-1} relative to the $N_2 + H_2$ dissociation limit are involved.

As mentioned in the Introduction, this paper stands as a first step toward the modeling of a global DMBE potential energy surface for the title system from accurate *ab initio* calculations. Thus, energies of all stationary points of N_2H_2 and possible dissociative limits have been calculated at different levels of theory, being collected in Table 3 along with the best theoretical and experimental estimates. As benchmark for the accuracy of relative energies stands the heat of formation of *trans*-N_2H_2 (48.8 ± 0.5 kcal mol^{-1}), recently established with good accuracy [19]. To compare with this experiment, theoretical thermochemical data

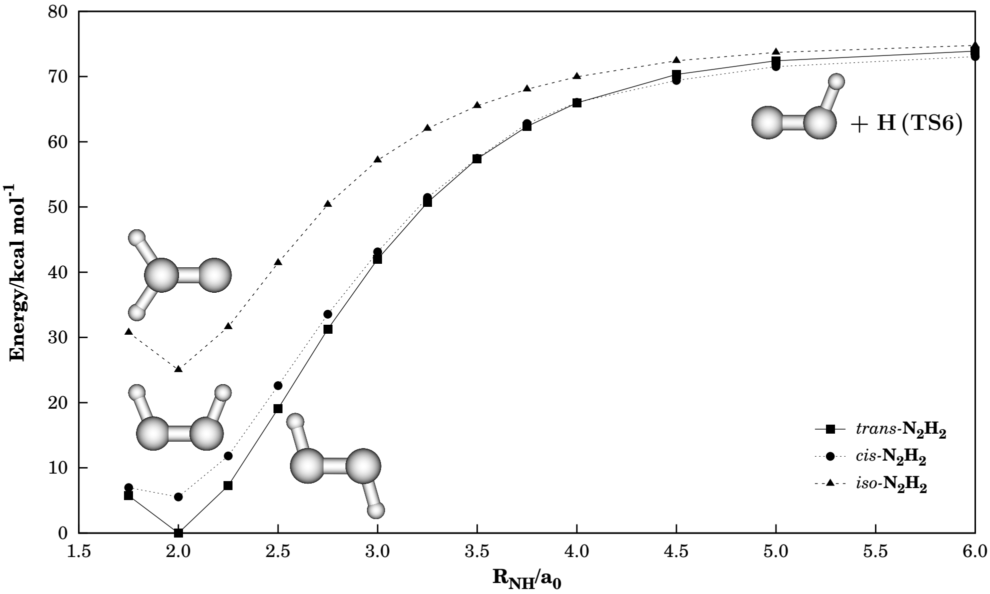

Figure 3. The dissociation-recombination pathways leading to the N_2H+H (TS6). Energy profiles for the dissociation of one hydrogen atom from the *trans*- (squares and solid line), *cis*- (circles and dash-dot line) and *iso*-N_2H_2 (triangles and dashed line) are calculated at the MRCI+Q/aug-cc-pVQZ level. For all structures, the NN distance and other NH distance have been fixed at 2.35 a_0 and 2.0 a_0 respectively, while the angles have been kept at the values corresponding to the optimized structures of *trans-, cis* and *iso* minima. Energies are in kcal mol^{-1} relative to the *trans*-N_2H_2 minimum.

should be used, although it has already been shown for the title system [10] that CI calculations are necessary to reach good agreement between computed and experimental enthalpies. In this work, instead of extremely expensive calculations of enthalpies at MRCI/aug-cc-pVQZ level that would be required for such a purpose, we compare the energies obtained from MCSCF and MRCI calculations subsequently corrected for zero point energy by using frequencies at the MCSCF/aug-cc-pVQZ level. For the MRCI we consider also energies corrected for size-consistency according to the Pople [28] and Davidson [27] schemes. The MCSCF calculations can be found to fail drastically in predictions of relative energies, as compared to the MRCI+Q results, with average errors of 0.4, 5.7, and 22.9 kcal mol^{-1} for local minima, transition states and dissociative limits, respectively. The situation remains unchanged if enthalpy calculations (not reported here) are considered. Moreover, MRCI energies corrected only for ZPE still give

Table 3. Stationary points on N_2H_2 potential energy surface.

	MCSCF/ AVQZ// MCSCF/ AVQZ[a]	MRCI/ AVQZ// MCSCF/ AVQZ[a]	MRCI(P)/ AVQZ// MCSCF/ AVQZ[a]	MRCI+Q/ AVQZ// MCSCF/ AVQZ[a]	G2M(MP2)// MP2/6-31G*[b]	CASSCF[c)]	CCSD(T)/ cc-pV∞Z[d]	Experimental
trans-N_2H_2	0.00	0.00	0.00	0.00	0.00	0.00	0.00	0[e]
cis-N_2H_2	4.60	5.03	5.05	5.05	4.81	6.68	5.21	
iso-N_2H_2	23.40	24.02	24.04	24.04	24.65	34.59	24.12	
TS1	54.29	51.40	51.11	51.07	49.53[g]	63.35		
TS2	61.03	56.39	55.09	54.96	48.86	62.93		
TS3	73.72	71.44	70.93	70.87	71.07	81.76		
TS4	90.50	93.16	92.95	92.94	95.55			
TS5	68.42	74.15	74.13	74.15	76.32	78.77		
$N_2H + H$ (TS6)	49.36	59.94	61.08	61.22	63.6	54.20		
$N_2 + 2H$	18.61	48.56	52.48	52.96		18.34		
$NH + NH$	107.30	119.00	118.86	118.88	124.83			121.6[f]
$NH_2(^2A'') + N(^2D)$	156.39	162.13	161.33	161.28				
$2N(^4S) + 2H$	234.21	271.13	273.11	273.42			278.73	
$H_2+2N(^2D)$	143.59	169.54	169.93	170.06				
$NH \cdots NH$ (van der Waals)	106.63	117.74	117.54	117.56				
$N_2 + H_2$	-70.80	-52.75	-50.30	-50.01	-48.88	-72.44	-49.57	-48.8[e]

Energies are in kcal mol^{-1} relative to the *trans*-N_2H_2 minimum. [a]This work. Energies from single point MRCI+Q/aug-cc-pVQZ calculations for MCSCF/aug-cc-pVQZ optimized structures, and corrected for ZPE based on MCSCF/aug-cc-pVQZ frequency calculations; see text. [b]G2M(MP2) energies for MP2/6-31G** optimized structures from Hwang and Mebel [1]. [c]Energies corrected for ZPE from Jensen *et al.* [2]. [d]Best estimate at 0 K accounting for inner-shell correlation and anharmonic ZPE corrections from Martin and Taylor 3. [e]Ref. 19. [f]Values obtained from experimental atomization energies [1]. [g]Ref. 12.

results of unsatisfactory accuracy for relative energies, with the heat of formation of *trans*-N_2H_2 overestimated by $4\,\mathrm{kcal\,mol^{-1}}$. Conversely, MRCI energies corrected for both size-consistency and zero-point energy agree within chemical accuracy ($1\,\mathrm{kcal\,mol^{-1}}$) with the best experimental [19] estimates and also with the benchmark theoretical results of Martin and Taylor [3] where additional inner shell correlation and anharmonic ZPE corrections have been taken into account. From these slightly better overall agreement is reached if the Davidson correction is applied. Thus, grid points calculated at the MRCI/aug-cc-pVQZ theory with energies subsequently corrected according to the Davidson scheme should be recommended when aiming at accurate global modeling of the N_2H_2 potential energy surface.

4 Concluding remarks

We have investigated the potential energy surface of N_2H_2 by using multireference approaches at FVCAS and MRCI levels with aug-cc-pVXZ (X=D,T,Q) basis sets. It has been shown that geometries and relative, ZPE corrected, energies of all local minima calculated at MRCI+Q/AVTZ or MRCI+Q/AVQZ levels agree well with the best theoretical estimates. For the barriers involved in the diimide isomerization, this work has confirmed the structures of three transitions states, associated to *trans*-*cis*(TS1,TS2) and *trans*-*iso*(TS3) pathways. The possibility of diazene rearrangement via dissociation of one of the hydrogens (TS6) has been ruled out for the former but should be considered for the latter. For N_2H_2 formation from molecular nitrogen and hydrogen, the perpendicular approach leading to *iso*-N_2H_2 via TS5 has been found to be favored over the parallel approach leading to *cis*-N_2H_2 via TS4. Moreover, based on a comparison with the best reported theoretical [3] and experimental [14, 19] results, MRCI/aug-cc-pVQZ theory (and possibly the less expensive MRCI/aug-cc-pVTZ one at some regions of configurational space) with energies corrected using the Davidson scheme emerges as the recommended route for modeling the global N_2H_2 potential energy surface.

Acknowledgments

This work has been carried out within Research Training Network HPRN-CT-2002-00170 (Predicting Catalysis), financed by the European Commission. It has also the support of Fundação para a Ciência e a Tecnologia, Portugal, under program POCI 2010 (contracts QUI/60501/2004, AMB/60261/2004, and REEQ/128/QUI/2005). The authors are also grateful to the Wroclaw Centre for Networking and Supercomputing for computer resources.

References

[1] D.-Y. Hwang and A. M. Mebel, J. Phys. Chem. A 107 (2003) 2865.

[2] H. J. A. Jensen, P. Jorgensen and T. Helgaker, J. Am. Chem. Soc. 109 (1987) 2895.

[3] J. M. L. Martin and P. R. Taylor, Mol. Phys. 96 (1999) 681.

[4] P. Mach, J. Masik, J. Urban and I. Hubac, Mol. Phys. 94 (1998) 173.

[5] S. P. Walch, J. Chem. Phys. 91 (1989) 389.

[6] B. S. Jursic, Chem. Phys. Lett. 261 (1996) 13.

[7] V. Stepanic and G. Baranovic, Chem. Phys. 254 (2000) 151.

[8] L. G. Spears Jr. and J. S. Hutchinson, J. Chem. Phys. 88 (1988) 240.

[9] C. J. Casewit and W. A. Goddard III, J. Am. Chem. Soc. 102 (1980) 4057.

[10] U. Brandemark and P. E. M. Siegbahn, Theor. Chim. Acta 66 (1984) 217.

[11] J. A. Pople and L. A. Curtiss, J. Chem. Phys. 95 (1991) 4385.

[12] B. J. Smith, J. Phys. Chem. 97 (1993) 10513.

[13] J. Andzelm, C. Sosa and R. A. Eades, J. Phys. Chem. 97 (1993) 4664.

[14] J. Demaison, F. Hegelund and H. Burger, J. Molec. Struct. 413-414 (1997) 447.

[15] F. Hegelund, H. Burger and O. Polanz, J. Mol. Spectrosc. 167 (1994) 1.

[16] N. C. Craig and I. W. Levin, J. Chem. Phys. 71 (1979) 400.

[17] J. H. Teles, G. Maier, B. A. Hess Jr. and L. J. Schaad, Chem. Ber. 122 (1989) 749.

[18] A. P. Sylwester and P. B. Derwan, J. Am. Chem. Soc. 106 (1984) 4648.

[19] H. Biehl and F. Stuhl, J. Chem. Phys. 100 (1994) 141.

[20] A. J. C. Varandas, Modeling and interpolation of global multi-sheeted potential energy surfaces (World Scientific Publishing, 2004), Advanced Series in Physical Chemistry p. 91.

[21] H.-J. Werner and P. J. Knowles, J. Chem. Phys. 82 (1985) 5053.

[22] P. J. Knowles and H.-J. Werner, Chem. Phys. Lett. 115 (1985) 259.

[23] T. H. Dunning, J. Chem. Phys. 90 (1989) 1007.

[24] R. Kendall, T. Dunning Jr. and R. Harrison, J. Chem. Phys. 96 (1992) 6769.

[25] J. Sun and K. Ruedenberg, J. Chem. Phys. 99 (1993) 5269.

[26] H.-J. Werner and P. J. Knowles, J. Chem. Phys. 89 (1988) 5803.

[27] S. R. Langhoff and E. R. Davidson, Int. J. Quantum Chem. 8 (1974) 61.

[28] J. A. Pople, R. Seeger and R. Krishnan, Quantum Chemistry Symposium 11 (1977) 149.

[29] H.-J. Werner and P. J. Knowles, MOLPRO is a package of *ab initio* programs written by H.-J. Werner, P. J. Knowles, with contributions from J. Almlöf, R. D. Amos, M. J. O. Deegan, S. T. Elbert, C. Hampel, W. Meyer, K. A. Peterson, R. Pitzer, A. J. Stone, P. R. Taylor, R. Lindh, (1998).

[30] A. J. C. Varandas, J. Chem. Phys. 113 (2000) 8880.

[31] H. Koizumi, G. C. Schatz and S. P. Walch, J. Chem. Phys. 95 (1991) 4130.

[32] L. A. Poveda and A. J. C. Varandas, J. Phys. Chem. 107 (2003) 7923.

[33] P. J. S. B. Caridade, S. P. J. Rodrigues, F. Sousa and A. J. C. Varandas, J. Phys. Chem. A 109 (2005) 2356.

Chapter 7

Conclusions and outlook

In the present thesis we reported a series of published results, mainly focused on the calculation and modeling of double many-body expansion potential energy surfaces for nitrogen-hydrogen molecular systems. Being fragments of larger N_xH_y species and intermediary steps in gas phase reactions close to those involved in the ammonia production, the DMBE-PESs for $HN_2\,(^2A')$, $NH_2\,(^2A'')$ and $NH_2\,(^4A'')$ molecules were constructed by fitting extensive *ab initio* data at the MRCI level of theory. Within the spirit of the DMBE formalism, the calibrated three-body potential fragments can be used as building blocks to construct a potential energy surface for ground state N_2H_2. In this sense, an exploratory *ab initio* study towards a DMBE-PES for such tetratomic specie is also reported in the last case studies. Besides their relevance for studying the ammonia chemistry, the above mentioned triatomics are involved in combustion reactions of nitrogen containing fuels and atmospheric chemistry. With the aim of to elucidate the possible role of the HN_2 species in thermal $\mathrm{De}-\mathrm{NO}_x$ processes, spectroscopic and quasiclassical trajectories calculations over an improved version of a DMBE-PES for HN_2, were also performed.

Analytical forms approximately represents the multisheeted nature of the potential energy surface through a single-valued function of the lowest electronic state. For $HN_2\,(^2A')$ and $NH_2\,(^4A'')$, at the conical intersections the single-valued function smooth the singularities resembling an avoided crossings. In turn, a novel switching function formalism is proposed to account the presence of two nitrogen states in the potential surfaces of $NH_2\,(^2A'')$. The improved switching form, calibrated to reproduce accurate *ab initio* data, allows, in a simple yet reliable manner, that atomic and diatomic fragments of the system dissociates to the appropriate electronic states, for the different asymptotic channels.

The main achievements of the reported DMBE-PES are its smoothness and its accuracy. Indeed, obtained functions fits the chemical regions of interest with root-means-square deviations below 0.5 $\text{kcal}\,\text{mol}^{-1}$. A notable feature of the present DMBE-PESs refers to their accurate description of the long-range regions where van der Waals forces are likely to dominate. A detailed study of modeling such a weak interactions is presented in DMBE-PES for $NH_2\,(^2A'')$, showing that the topography of the van der Waals regions change drastically when increase the quality of the basis set. In turn, special care was devoted during the fitting procedure to avoid the appearance of spurious stationary points and/or unphysical behaviors in the potential.

In order to model an *ab initio*-based DMBE potential energy surface for ground state N_2H_2, electronic structure calculations, at the MRCI+Q/AVTZ and MRCI+Q/AVQZ level of theory, were carried out for all local minima and transition states of such a system. The good agreement between the present results and the best theoretical and experimental estimates, indicate that such *ab initio* methods can be used to explore the potential energy surface for N_2H_2. In fact, a mapping of selected regions of the configuration space of this molecule is currently in progress, with the aim of to calibrate appropriate four-body terms, warranting the convergence of the DMBE cluster expansion.

Summarizing we can concluded that the potential energy surfaces reported in the present thesis, constitute an starting data bank of nitrogen-hydrogen molecular systems to be used as building blocks in the construction of accurate DMBE-PES for large N_xH_y species.

Mathematical appendix

A Linear least-squares [1, 2]

Given a set of N pairs $(\mathbf{x}_i, y_i)$, *e.g.* vector positions in parameter space of the molecule and values of the potential energy at the points, and a linear *model* function that depends of M adjustable parameters, a set of best-fit parameters correspond to a minimum of the merit function

$$\chi^2 = \sum_{i=1}^{N} \left[\frac{y_i - \sum_{k=1}^{M} c_k X_k (\mathbf{x}_i)}{\sigma_i} \right]^2 \tag{A 1}$$

where

$$y(\mathbf{x}) = \sum_{k=1}^{M} c_k X_k (\mathbf{x}) \tag{A 2}$$

is a linear combination of arbitrary fixed functions of $\mathbf{x}$.

The minimum of (A 1) occurs when the derivative of χ^2 with respect to all the M parameters c_k vanishes, *i.e.*

$$0 = \sum_{i=1}^{N} \frac{1}{\sigma_i^2} \left[y_i - \sum_{j=1}^{M} c_j X_j (\mathbf{x}_i) \right] X_k (\mathbf{x}_i) \qquad k = 1, \ldots, M \tag{A 3}$$

Interchanging the order of summations, equations (A 3) can be written in the matrix form

$$\boldsymbol{\Lambda} \cdot \mathbf{c} = \boldsymbol{\beta} \tag{A 4}$$

where

$$\Lambda_{kj} = \sum_{i=1}^{N} \frac{X_j (\mathbf{x}_i) X_k (\mathbf{x}_i)}{\sigma_i^2}, \qquad \beta_k = \sum_{i=1}^{N} \frac{y_i X_k (\mathbf{x}_i)}{\sigma_i^2} \tag{A 5}$$

and $\mathbf{c}$ is the column vector of the adjustable parameters.

Solutions to the linear least squares problem (A 4) can be obtained by using the Gauss-Jordan elimination method, which consists in looking for the column vector $\mathbf{c}$ by applying row operations on the augmented matrix $\mathbf{\Lambda}|\mathbf{c}$ to transform the matrix $\mathbf{\Lambda}$ into diagonal form.

A more general procedure to minimize (A 1), preventing no solution of (A 4) due to singularity in $\mathbf{\Lambda}$, use the *singular value decomposition* (SVD) techniques. Such a method is based on a theorem which states that any $N \times M$ matrix $\mathbf{A}$, no matter how singular the matrix is, can be factorized in the form

$$\mathbf{A} = \mathbf{U} \cdot \mathbf{W} \cdot \mathbf{V}^T \tag{A 6}$$

where $\mathbf{U}$ is an $N \times M$ orthogonal matrix, $\mathbf{W}$ is a $M \times M$ diagonal matrix with positive or zero elements (the *singular values* of $\mathbf{A}$) and $\mathbf{V}^T$ is the transpose of the $M \times M$ orthogonal matrix $\mathbf{V}$.

Defining the following matrix and column vector

$$A_{ij} = \frac{X_j\left(\mathbf{x}_i\right)}{\sigma_i} \qquad \text{and} \qquad \mathbf{b}_i = \frac{y_i}{\sigma_i} \tag{A 7}$$

Equation (A 1) can be written as

$$\chi^2 = \left|\mathbf{A} \cdot \mathbf{c} - \mathbf{b}\right|^2 \tag{A 8}$$

Then, the vector $\mathbf{c}$ which minimize (A 8) can be obtained by using SVD at solving the set of simultaneous linear equations

$$\mathbf{A} \cdot \mathbf{c} = \mathbf{b} \tag{A 9}$$

Thus, the vector

$$\mathbf{c} = \mathbf{V} \cdot \left[\operatorname{diag}\left(\frac{1}{\omega_j}\right)\right] \cdot \left(\mathbf{U}^T \cdot \mathbf{b}\right) \tag{A 10}$$

will be a solution of (A 9) in the fallowing sense: *i*) if $\mathbf{A}$ is nonsingular (A 10) is the unique solution to the equation, *ii*) if $\mathbf{A}$ is singular and $\mathbf{b}$ belongs to the range of $\mathbf{A}$ (subspace of $\mathbf{b}$ 'target' by $\mathbf{A}$) then (A 10) is the solution with smallest norm, *iii*) if $\mathbf{A}$ is singular and $\mathbf{b}$ does not belongs to the range of $\mathbf{A}$ then (A 10) is the solution which minimizes the residual $|\mathbf{A} \cdot \mathbf{c} - \mathbf{b}|$.

In practice if some ω_j's are very small but nonzero, is better to assume $\mathbf{A}$ as being singular by zeroing its small singular values (replace $1/\omega_j$ by zero if $\omega_j = 0$ or very small). Hence, SVD cannot be used as a "black-box", and thresholds should be fixed to the size of the ω_j's and the residual.

B Quadratic steepest-descent [3–5]

The minimum energy path (MEP) in a potential energy surface $V(\mathbf{x})$, is the reaction path which fulfill the following set of differential equations

$$\frac{d\mathbf{x}}{ds} = -\frac{\boldsymbol{\nabla} V(\mathbf{x})}{|\boldsymbol{\nabla} V(\mathbf{x})|} \tag{B 1}$$

where s is the arc length counted from an arbitrary chose point.

In the quadratic steepest-descent (QSD) scheme the potential energy function is approximated by its second-order Taylor expansion around a given geometry,

$$V^{(Q)}(\mathbf{x}) = V(\mathbf{x}_k) + (\mathbf{x}-\mathbf{x}_k)^{\dagger}\mathbf{g} + \frac{1}{2}(\mathbf{x}-\mathbf{x}_k)^{\dagger}\mathbf{H}(\mathbf{x}-\mathbf{x}_k) \tag{B 2}$$

where $\mathbf{g}$ and $\mathbf{H}$ are the gradient vector and the Hessian matrix, respectively, at the point $\mathbf{x}_k$.

By introducing the computational convenient parameter $u(s)$, mapping the arc length between the boundaries $0 \leq u \leq 1$

$$u(s) = \exp\left\{\int^{s} ds' \, |\mathbf{g}[\mathbf{x}(s')]|^{-1}\right\} \tag{B 3}$$

the equation (B 1), within the QSD approach, becomes

$$\frac{d\mathbf{x}}{du} = u^{-1}[\mathbf{g} + \mathbf{H}(\mathbf{x}-\mathbf{x}_k)] \tag{B 4}$$

Eq. (B 4) is solved by the curves

$$\mathbf{x}(u) = \mathbf{x}_k - \mathbf{H}^{-1}\left(\mathbf{I} - u^{\mathbf{H}}\right)\mathbf{g}, \tag{B 5}$$

$$u^{\mathbf{H}} = \mathbf{U}\left(u^{\lambda_i}\delta_{ij}\right)\mathbf{U}^{\dagger} \tag{B 6}$$

where the orthogonal matrix $\mathbf{U}$ and the eigenvalues are obtained from the diagonalization of the Hessian $\mathbf{U}^{\dagger}\mathbf{H}\mathbf{U} = (\lambda_i\delta_{ij})$.

The implementation of this local quadratic approximation is straightforward: at a given geometry $\mathbf{x}_k$, compute the energy, gradient and Hessian matrix, build the QSD curve (B 5) and step (in a small quantity h) to the new geometry $\mathbf{x}_{k+1}$, where the next energy, gradient and Hessian matrix are computed, and so on.

In order to improve the stability and accuracy of the numerical integration in regions of the configuration space with strong curvature, the step size is damped in the following form

$$h\left(\kappa\right) = h_{\mathrm{max}} f\left(\kappa\right), \tag{B 7}$$

$$f(\kappa) = a + \frac{1-a}{1+\left(\kappa/\kappa_{\mathrm{med}}\right)^{\nu}} \tag{B 8}$$

where a and ν are fixed parameters between 0 and 1, and κ is the absolute value of the curvature vector defined as

$$\boldsymbol{\kappa} = \frac{d^2\mathbf{x}_k}{ds^2} \tag{B 9}$$

For $\kappa = 0$ the step size reach its maximum value h_{max}, the minimum value $h_{\mathrm{min}} = ah_{\mathrm{max}} < h_{\mathrm{max}}$ for $\kappa = \infty$, and the intermediate value $h_{\mathrm{med}} = \left(h_{\mathrm{min}} + h_{\mathrm{max}}\right)/2$ for $\kappa = \kappa_{\mathrm{med}}$.

References

[1] W. H. Press, S. A. Teukolsky, W. T. Vetterling, and B. P. Flannery, *Numerical Recipes in Fortran: the Art of Scientific Computing* (Cambridge University Press, New York, 1992).

[2] R. A. Horn and C. R.Johnson, *Matrix Analysis* (Cambridge University Press, Cambridge, 1999).

[3] J.-Q. Sun and K. Ruedenberg, J. Chem. Phys. **99**, 5257 (1993).

[4] J.-Q. Sun and K. Ruedenberg, J. Chem. Phys. **99**, 5259 (1993).

[5] F. Eckert and H.-J. Werner, Theor. Chem. Acc. **100**, 21 (1998).